People's Democratic Republic of Algeria

Ministry of Higher Education and Scientific Research

August 20, 1955 University -Skikda

Faculty of Sciences
Department of Physics

N° : ……..

Thesis

Presented to obtain the degree of Doctorate

Speciality: Materials physics

Thesis entitled:

Synthesis and characterization of nanostructured oxide films

Presented by:

Wassila LAIB

Defended on: 13 /07/2025 before the jury composed of:

Sofiane LOUIDI	Professor	University of August 20, 1955- Skikda	President
Sonia AZZAZA	Professor	University of August 20, 1955- Skikda	Supervisor
Safia ALLEG	Professor	University of Badji-Mokhtar - Annaba	Co-supersisor
Amara OTMANI	Professor	University of August 20, 1955- Skikda	Examiner
Saida SOUILAH	MCA	National Higher School of Technology and Engineering (ENSTI) - Annaba	Examiner
Amel GACEM	MCA	University of August 20, 1955- Skikda	Examiner
Radouane DAIRA	MCA	University of August 20, 1955- Skikda	Invited

Academic year : 2024/2025

To my dear parents

To my sisters and my brothers

To all my colleagues and everyone helped me.

Acknowledgements

*First thanks to **ALLAH** for his grace and for this help to let me completing my research*

*For most, I would like to express my sincere gratitude to my advisor Mrs. **Sonia AZZAZA,** Professor at Skikda University, for the continuous support of my thesis study and research, for his patience, motivation, enthusiasm, and immense knowledge. His guidance helped me in all the time of research and writing of this thesis.*

*I would also like to express my sincere gratitude to my co-supervisor, Ms. **Safia ALLEG**, professor at Badji Mokhtar university -Annaba. I am truly grateful for the time you dedicated, for your enthusiasm, and for all the scientific and technical guidance you have provided.*

*I would like to extend my gratitude to Mr. **Sofiane LOUIDI**, Professor at Skikda University, for graciously accepting the presidency for my thesis.*

*I address my thanks to Mr. **Amara OTMANI**, Professor at Skikda University, Mrs. **Amel GACEM**, MCA at Skikda university and Mrs. **Saida SOUILAH**, MCA at ENSTI superior school of Annaba, for having agreed to do part of the jury of this thesis as examiners, that their remarks and their criticisms are appreciated and i am grateful to them for reading my thesis*

*I express my deepest appreciation to Mr. **Radouane DAIRA**, MCA at Skikda University, for his assistance and support.*

Not least of all, I owe so much to my entire family for their continuous support and belief in my ability to achieve so much.

Abstract

Nanostructured $Cu_{1-x}Fe_xO$ thin films (x = 0, 0.10, 0.15, 0.20 and 0.25) were succefully deposited on glass substrate heated at 350°C by using a simple and low cost spray pyrolysis technique. The Structural, morphological, optical, magnetic and electrical properties of the films were investigated. The X-Ray Diffraction spectra showed that all the samples exhibited a single CuO monoclinic structure up to x = 0.20. The apparition of the secondary α-Fe_2O_3 phase for x = 0.25 alongside CuO indicates a solubility of about 20% Fe in the host CuO matrix. With increased Fe content and dislocation density, the crystallite size reduced from approximately 46 to 33 nm, the band gap dropped from 3.075 eV for x = 0 to 2.974 eV for x = 0.25, and the CuO unit cell volume contracted. The saturation magnetisation rises from 0.166 to 0.603 emu, and the coercivity ranges between 17.6 and 231.5 Oe. The squareness ratio varies from 0.108 to 0.497, suggesting that the prepared films are pseudo-single domains. The electrical resistivity decreases linearly with increasing Fe content from 42.1 to 5.8 kΩ.cm, and the electrical conductivity reaches 0.172 $\Omega^{-1}.cm^{-1}$ for x = 0.25.

***Keywords*:** Copper oxide; Nanostructured films; XRD; Rietveld refinement; Magnetic properties.

Résumé

Les couches minces nanostructurées $Cu_{1-x}Fe_xO$ ($x = 0 \leq x \leq 0,25$) ont été déposées sur un substrat en verre, préchauffé à 350°C, en utilisant la méthode de spray pyrolyse. Les propriétés structurale, morphologique, optique, magnétique et électrique des couches minces obtenues sont examinées. Les échantillons préparés dans la plage de concentration $0 \leq x \leq 0,20$ présentaient une phase unique, correspondant à une structure monoclinique (groupe spatial C2/c). Pour $x = 0,25$, en plus de la phase CuO, une phase secondaire magnétique nanocristalline α-Fe_2O_3 apparaît indiquant une limite de solubilité du Fe dans la matrice CuO d'environ 20 %. Avec l'augmentation de la teneur en Fe et de la densité de dislocations, la taille des cristallites a diminué de 46 à 33 nm, la bande interdite est passée de 3,075 eV pour x = 0 à 2,974 eV pour x = 0,25, et le volume de la maille CuO s'est contracté. L'aimantation à saturation passe de 0,166 à 0,603 emu, et la coercivité est comprise entre 17,6 et 231,5 Oe. L'aimantation rémanente réduite varie de 0,108 à 0,497, ce qui suggère que les films préparés sont des pseudo-domaines simples. La résistivité électrique diminue linéairement avec l'augmentation de la teneur en Fe de 42,1 à 5,8 kΩ.cm, et la conductivité électrique atteint 0,172 $\Omega^{-1}.cm^{-1}$pour x = 0,25

Mots clés : Oxyde de cuivre ; Nanostructures ; Affinement Rietveld, Bande interdite ; Aimantation.

Contents

Chapter 3: Results & Discussion

Appendix

List of figures

List of tables

Introduction

Introduction

Nanostructured thin films have attracted considerable interest due to their unique size-dependent physicochemical properties, which are appealing for a wide range of applications. A thin film is traditionally defined as a material layer ranging from a few nanometers to several micrometres in thickness. Due to their thinness, thin films are often used to coat surfaces or layers that have been previously deposited. However, recent technological breakthroughs have enabled the development of freestanding thin layers, extending the application perspectives. Depending on both the target applications and the deposition technique used, nanostructured films can be designed and developed by tuning their atomic and molecular 2D and/or 3D aggregation, thickness, crystallinity, and porosity, as well as their optical, mechanical, catalytic, and conductive properties. The resulting structures can be exploited in various applications, including electronic devices, electronic semiconductor devices (with superconducting, semiconducting, magnetic, thermal, and insulating layers), energy storage and conversion (such as batteries, solar cells, and fuel cells), optical and protective coatings, and functional tools (including catalysts, sensors, and biosensors).

Nanostructured CuO is a promising candidate for multifunctional applications due to its narrow band gap, ranging from 1.5 to 3 eV, its natural availability, affordability, and ease of fabrication with diverse morphologies and dimensions (1D, 2D, and 3D) [1,2]. Copper oxide can be utilised as photodetectors, gas sensors, biosensors, solar cells, supercapacitors, for the removal of inorganic pollutants, nanofluids, and spintronic devices. The CuO exhibits an antiferromagnetic (AFM) behaviour with low Néel temperatures (T_N=229 and 213 K) [3]. However, at the nanoscale level, the CuO band gap is significantly more pronounced than the bulk one, and room-temperature ferromagnetism (RTFM) may be observed due to the behaviour of spins or electrons, which can alter the material's properties [4]. Furthermore, the properties of CuO can be tailored for practical use by doping with transition metals (TM). However, using high concentrations of magnetic TM ions may enhance ferromagnetism, but

can also lead to the formation of a secondary magnetic phase. The presence of which impurities is not suitable for practical applications in DMS materials. New approaches are based on the combination of codoped semiconductors with low possible concentrations to enhance the magnetic properties. Few reports exist on higher Fe-doped CuO multi-phased systems. Still, the investigation of the origin of their magnetic properties remains very challenging and requires more characterisations, beyond computational calculations.

Several methods have been employed to fabricate nanostructured CuO-DMS thin films, including pulsed laser deposition, spin coating, thermal evaporation, chemical vapour deposition, molecular beam epitaxy, and dip coating techniques [5]. Among these various techniques, Spray pyrolysis (SPT) is a simple, cost-effective, and versatile technique; it has been widely used to produce adherent, homogeneous, and stoichiometric films. SPT permits the production of high-quality oxide films with varying thicknesses and sizes, typically homogeneous and thermally stable. Besides, the deposition parameters (starting solution, nozzle-substrate distance, gas flow rate, deposition time, spray rate, droplet size, and substrate temperature) can affect the properties of the CuO film. Previous studies have reported various techniques for depositing nanostructured Cu oxides under different experimental conditions [6]. The results show the formation of single- or multi-phased systems, with distinct morphologies and thereby different properties [7].

Few studies have been reported on iron-doped CuO films with high Fe content using the spray pyrolysis route, and the results obtained are still far from expectations, as they vary significantly from one study to another. The present work aims to investigate the effect of a relatively high Fe content on the structural, morphological, optical, electrical, and magnetic properties of nanostructured CuO thin films. The relation between microstructure (crystallite size, defects, phases) and absorption and bandgap of the Fe-doped thin films will be studied. Besides, conductivity and magnetic behaviour are thoroughly examined to comprehend different magnetic interactions.

The thesis is organised into an Introduction, a conclusion and three chapters. Chapter one provides a literature survey on recent advances in nanostructured thin films, the different deposition techniques, characterisation and properties. Moreover, a literature review of some previous studies on nanostructured CuO-DMS is presented. In Chapter 2, we introduce the method used in the present work for preparing films. The experimental conditions for sample

deposition using a spray pyrolysis technique, as well as various characterisation techniques, are also employed. In the last chapter, the results obtained from the deposited CuO thin films will be reported, along with a detailed discussion.

References

[1] U.K. Gaur, A. Kumar, G.D. Varma. J. Mater. Chem. C. 3 (2015) 4297.
[2] D.P. Dubal, G.S. Gund, R. Holze, C.D. Lokhande. J. Power Sources, 242 (2013) 687.
[3] Q. Zhang, K. Zhang, D. Xu, G. Yang, H. Huang, F. Nie, C. Liu, S. Yang. Prog. Mater. Sci., 60 (2014) 208.
[4] D.C. Agarwal, U.B. Singh, S. Gupta, R. Singhal, P.K. Kulriya, F. Singh, A. Tripathi, J. Singh, U.S. Joshi, D.K. Avasthi. Sci. Rep., 9 (2019) 6675.
[5] J.O. Ighalo, P.A. Sagboye, G. Umenweke, O.J. Ajala, F.O. Omoarukhe, C.A. Adeyanju, S. Ogunniyi, A.G. Adeniyi. Monit. Manag., 15 (2021) 100443.
[6] S. Manna, S.K. De. J. Magn. Magn. Mater., 322 (2010) 2749.
[7] R. Daira, A. Kabir, B. Boudjema, C. Sedrati. Solid State Sci., 104 (2020)106254.

Chapter 1
Background and literature survey

Chapter 1

Background and literature survey

This chapter presents the fundamentals of nanostructured thin film technology, including deposition techniques, various characterisation methods, and film properties. Due to the exceptional diversity of nanostructured thin films and the extensive range of applications, it is complicated to cover in detail all the areas; however, as many thin films share several features in all steps of the production process, characterisation, and even applications, it is possible to treat them with a general perspective. A literature review on undoped and doped CuO nanostructures is also reported.

1.1. Nanostructured materials

The idea of nanomaterials, nanoscience, and nanotechnologies was formulated by Richard Feynman in 1959 in his famous lecture "There's Plenty of Room at the Bottom". He said that "The principles of physics, as far as I can see, do not speak against the possibility of manoeuvring things atom by atom" [1]. Since then, a nanomaterials "revolution" has followed, confirming their superior properties, including toughness, strength, hardness, resistance to corrosion and wear, as well as various thermal, magnetic, and optical features.

Over the last few decades, nanostructured materials have garnered extensive interest due to their potential applications in various fields, including optoelectronics, spintronics, catalysis, and sensing. The physical and chemical properties of nanomaterials can differ significantly from those of their bulk counterparts due to their small size and the resulting larger surface area-to-volume ratio. In general, nanomaterials comprise novel properties that are typically not observed in their conventional counterparts.

Nanostructures are materials or components thereof in alloys, compounds, or composites having one or more dimensions of nanometer size (1 nm = 10^{-9} m = 10 Å). The phenomenological dimensionality of nanomaterials depends on the size relative to physical

parameters such as quantum confinement regime (≤100 atoms), mean free path of conduction electron (<10 nm), mean free path of hot electron (<1 nm), Bohr excitation diameter (Si = 8.5 nm, CdS = 6 nm, GaAs = 196 nm), de Broglie wavelength (<1 nm). Besides the size of nanostructures, several other aspects must be considered to define nanomaterials. Therefore, the chemical and physical properties of nanoparticles do not only depend on their size, but also on their composition, which can be organic (polymers, lipids) as well as inorganic (metal, metal oxides, metalloid, metalloid oxides) or a mixture of both [2].

Nanomaterials can be categorised into various groups based on size, origin, structural configuration, pore diameter, and potential toxicity [2-6]. Siegel classified nanomaterials by the number of dimensions into four types (Figure 1.1):

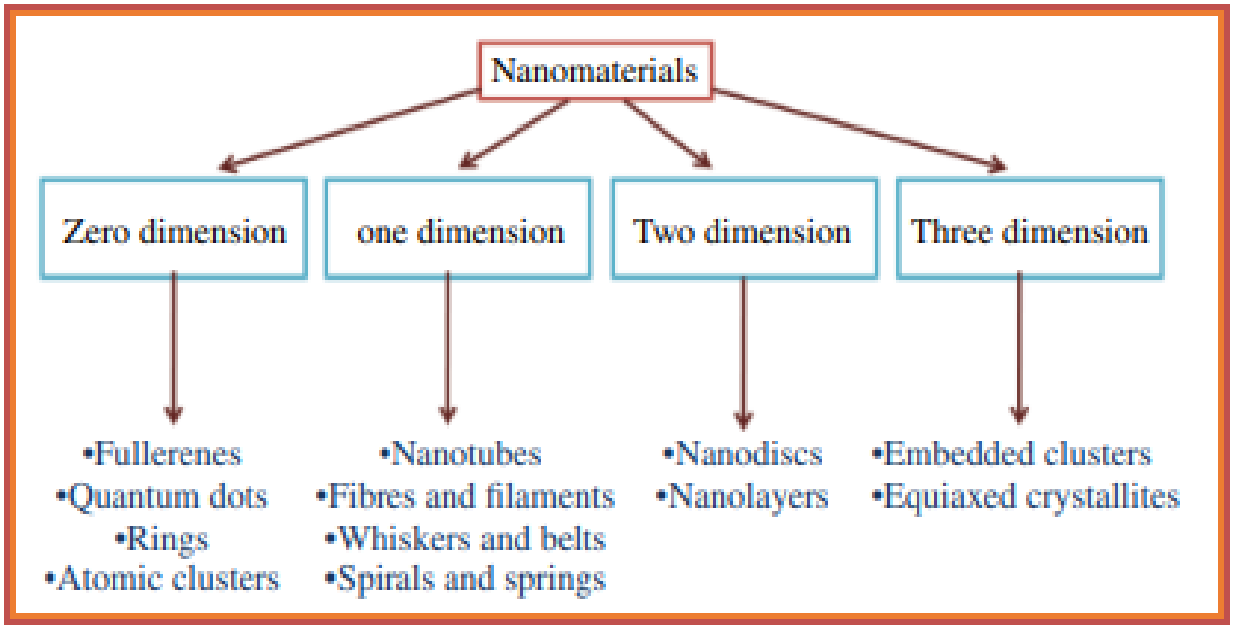

***Figure 1.1**: Classification of nanomaterials based on dimensions [7].*

1.1.1. Zero-dimensional nanomaterials

Zero-dimensional nanomaterials are those wherein all dimensions are less than 100 nm. Various physical and chemical methods have synthesised some 0D-nanomaterials having well-controlled dimensions. Some of these materials include homogeneous particle arrays and heterogeneous particle arrays such as quantum dots (QDs), hollow spheres, nanolenses, core-shell QDs, and others [8].

1.1.2. One-dimensional nanomaterials

One-dimensional nanomaterials are defined as materials with one dimension greater than 100 nm, while others are at the nanoscale. These nanostructures have been used in many fields due to their superior properties compared to bulk materials/structures. One-dimensional

nanostructures include nanowires, nanorods, and nanotubes. It is recognised that 1D nanostructures are of excellent use in exploring electrical, mechanical, and thermal properties as well as size reduction [8]. Moreover, 1D nanostructures play a crucial role as interconnections and functional units in the manufacturing and construction of electronic, electromechanical, optoelectronic, and electrochemical devices. Additionally, in contrast to QDs and wells, advancements in 1D nanostructures have been delayed due to various difficulties associated with their synthesis, morphology, purity, and chemical composition [9, 10].

1.1.3. Two-dimensional nanomaterials

Two-dimensional nanomaterials are defined as those in which two dimensions are on the microscale and one dimension is at the nanoscale. Nanofilms, nanocoatings, and nanolayers are the prominent examples. The shape of 2D nanomaterials is typically plate-like. The 2D nanomaterials are synthesised by deposition on a substrate as single-layer or multilayered structures. These nanomaterials can be amorphous or crystalline, metallic or non-metallic, or polymeric. Recently, 2D nanomaterials have become the primary focus of researchers in fields such as solar energy due to their intriguing surface and electronic properties.

1.1.4. Three-dimensional nanostructure materials

Materials with dimensions greater than 100 nm are 3D-nanomaterials. There is debate about whether 3D nanomaterials are considered nanomaterials. Some nanotechnologists consider them a type of nanomaterial, but others disagree because of the dimensions being greater than 100 nm. There is extensive research on 0D, 1D, and 2D nanomaterials, but relatively little on 3D nanostructures [11].

1.2. Nanostructured thin films

1.2.1. Definition

Nanostructured thin films have garnered considerable interest due to their unique size-dependent physicochemical properties, which are appealing for a wide range of applications. A thin film is traditionally defined as a material layer ranging from a few nanometers to several micrometres in thickness. Due to their thinness, thin films are often used to coat surfaces or layers that have been previously deposited. However, recent technological breakthroughs have enabled the development of freestanding thin layers, extending the application perspectives. Depending on both the target applications and the deposition

technique used, nanostructured films can be designed and developed by tuning their atomic and molecular 2D and/or 3D aggregation, thickness, crystallinity, and porosity, as well as their optical, mechanical, catalytic, and conductive properties. The resulting structures can be exploited in various applications, including electronic devices, electronic semiconductor devices (with superconductive, semiconductive, magnetic, thermal, and insulating layers), energy storage and conversion (such as batteries, solar cells, and fuel cells), optical and protective coatings, and functional tools (including catalysts, sensors, and biosensors).

Nanostructured thin films are a category of 2D-nanomaterials. They are formed by deposited layers on the surface, which is obtained by changing four states of matter, such as vapour, solid, liquid, and plasma. It involves the condensation of atoms, molecules, and ions. Thin films have different physical dimensions, metallurgy, and geometry compared to bulk materials.

1.2.2. Classification of nanostructured thin films

The term "thin films" is ambiguous and usually used to describe "coating" layers. A thin film may be defined as a deposited solid layer with a thickness of a few angstroms to 10 microns. Furthermore, depending on the thickness, the thin films may be classified into three groups: Ultra-thin (50-100 Å), Thin film (100-10000 Å), and moderately thick film (above 1000 Å) [12,13]. Further, nanostructured thin films can also be classified by their crystallinity, morphology, and functionalities. Thin films are categorised by their composition and morphology, and classified in six different groups (Figure 1.2).

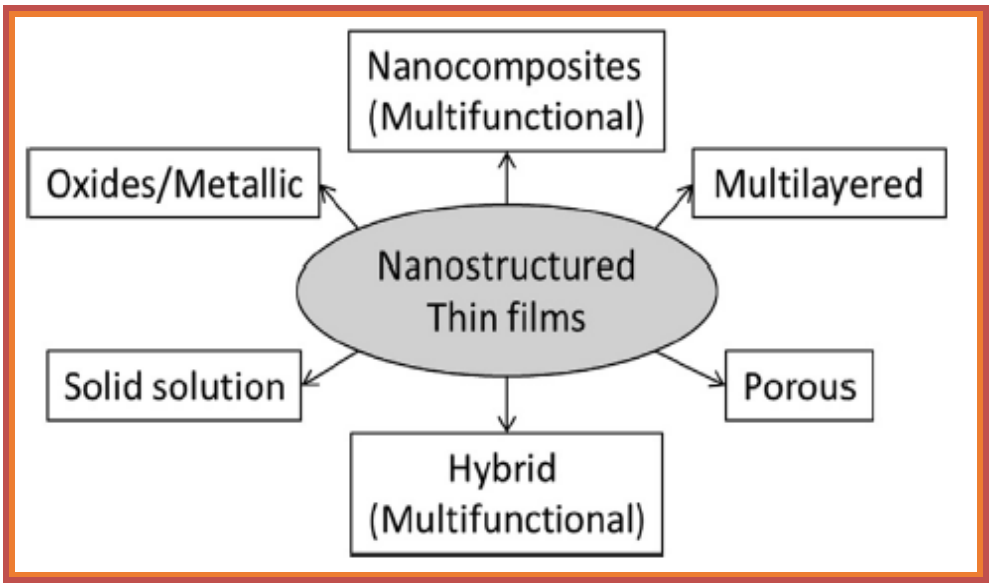

***Figure 1.2**: Classification of nanostructured thin films [14].*

1.2.3. Synthesis of nanostructured thin films

The properties of thin films depend on many factors, such as preparation conditions, film structure, defects, impurities, and film thickness [15]. The enormous usage of nanostructured thin films has drawn the attention of researchers to finding an appropriate method for synthesis to improve specific properties.

It is well known that the atomic structure, composition, morphology, surface roughness, microstructure (including crystallinity and phases), defects, and interfaces, and consequently, the properties of thin films are strongly linked to the growth mechanism, deposition techniques, and synthesis parameters [16,17]. Therefore, the resulting thin films can be of high quality, ranging from compact to porous, rigid to flexible, and can be amorphous, polycrystalline, or epitaxial [18]. Another important factor related to the synthesis of thin films is the type of substrate used for deposition and its preparation. The most commonly used substrates are metals, semiconductors (e.g., Si, conductive glasses ITO, FTO), aluminium oxide, and others. The substrate preparation procedure typically involves polishing/roughening, cleaning and chemical modification of the surface to provide a substrate or surface on which thin films with the desired properties can be deposited. Since thin films are frequently exposed to environmental factors such as chemical (pH, dissolved oxygen), radiative, and thermal stresses, their properties are usually designed and tailored for specific applications. They are closely related to the method of thin film synthesis.

Different methods of production are used to develop/improve the nanostructured film properties and the suitability for scaling up. Generally, thin-film production can be realised based on two technological groups, namely top-down or bottom-up methods. Top-down methods are based on physical or chemical processes and are often used to obtain laminar nanostructures such as nanosheets and nanoflakes. However, Bottom-up syntheses are used to produce complex nanostructured thin films, ranging from atoms to molecules. They can often be modified to control both the chemical and physical properties of these thin films (Figure 1.3).

In the physical deposition technique, mechanical or electrochemical methods are used to deposit the thin film on the substrate. Materials to be deposited on the substrate is totally depend upon the temperature, pressure and other physical conditions [16]. The second process is called as chemical vapor deposition. It is a chemical process in which, the gaseous precursor is used. The precursor gases are moved into the chamber with the substrate. A

chemical reaction takes place between the substrate and precursor. The reaction is continued up to higher temperature till the desired thickness is obtained [17,19]. The overall thin film deposition technique contains three major steps viz. (1) The creation of atomic/molecular/ionic species, (2) Transport of these materials through a suitable medium, and (3) Condensation of species on a proper substrate [20].

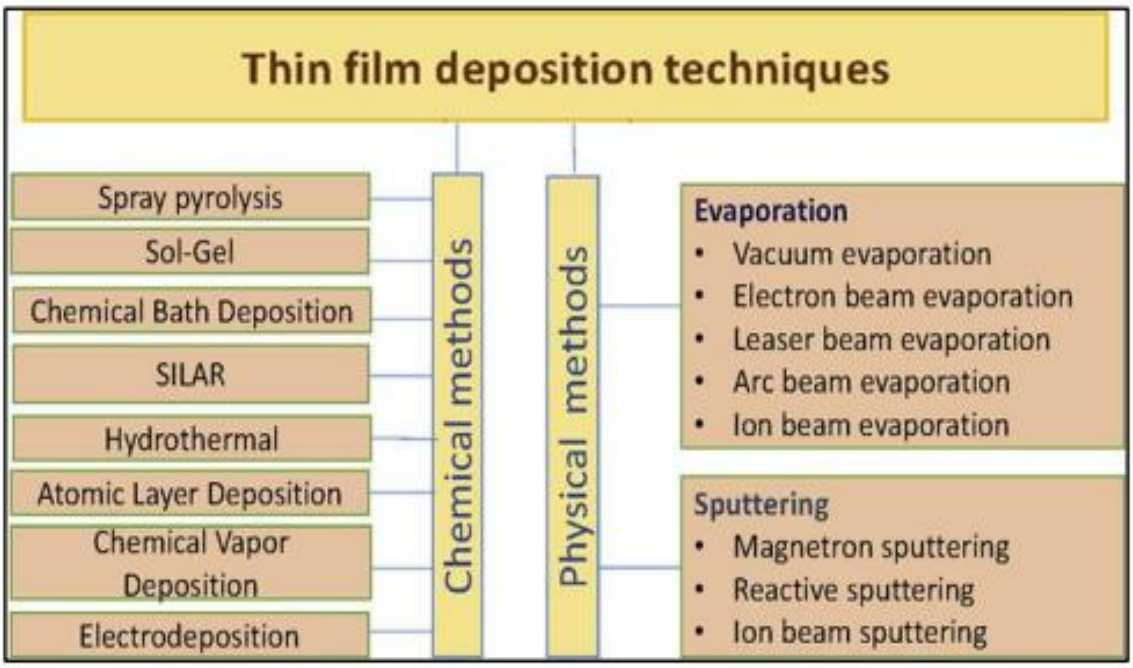

Figure 1.3: *Thin film deposition techniques [21].*

1.2.4. Stages of thin film growth

During thin film growth, different mechanisms occur at various stages (Figure 1.4) [22]:

(1) Surface preparation

Surface preparation is defined as the treatment of a surface to enhance its performance, processing, and functionality. It involves the following steps: (1) cleaning, (2) alteration of surface chemistry, (3) modification of physical properties and morphology, (4) development of nucleation sites, and (5) addition of nucleation agents to make the surface more reactive. These modifications can be achieved through diffusion, physical sputtering, chemical reactions, self-assembly, chemical etching, and plasma treatments. These modifications to the surface change the properties, surface structure, and texture of thin films. For example, ion species from plasma may be used to clean the surface via physical sputtering [23]. These ions or gas nitriding strengthen the stainless steel's surface, making it more suitable for tribological coatings to obtain satisfactory performance [24].

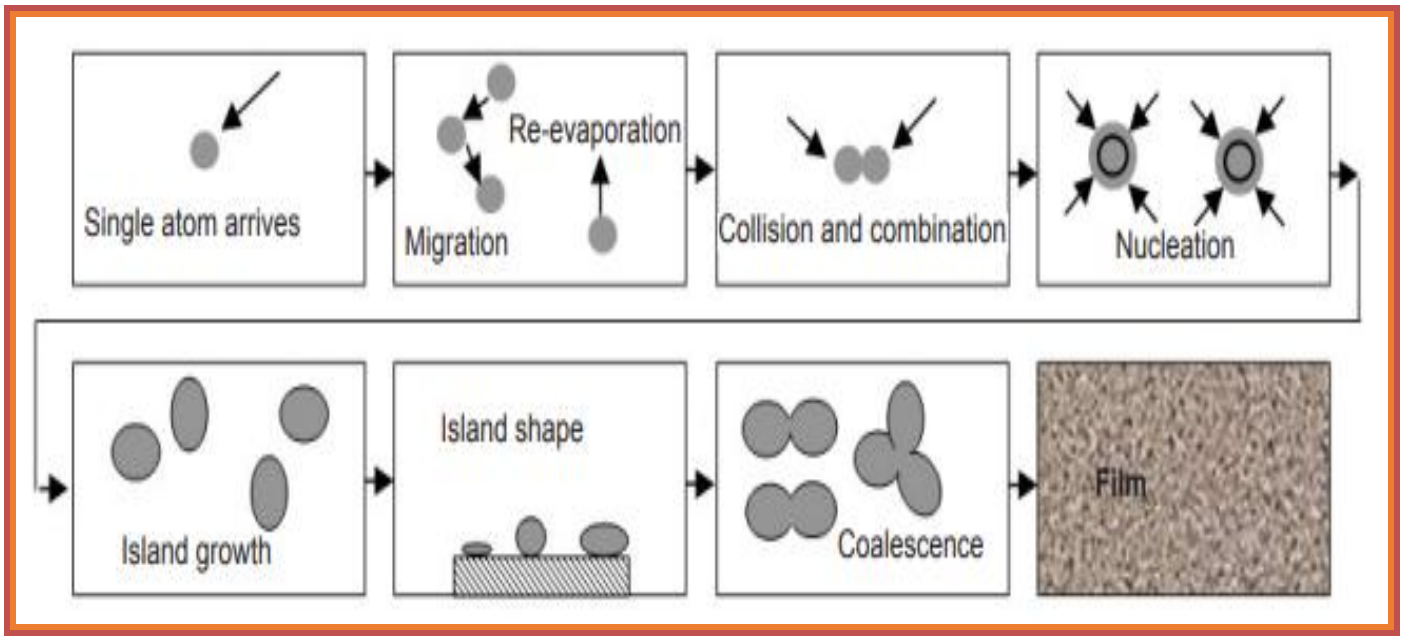

***Figure 1.4**: Different stages of nucleation and growth of nanostructured thin film [33].*

(2) Adatoms and surface diffusion

The impinging atoms or ions interact with the surface at a distance of some A. After a collision with the surface, most of its kinetic energy (KE) and momentum are lost and absorbed by the surface, resulting in a decrease in its potential energy (P_E). Adsorbed atoms are called adatoms. Figure 1.5 shows the P_E profile experienced by different adatoms. 'A' is the adatom at rest, 'B'is the diffusing adatom, 'C' is the adatom diffusing over the step edge, and 'D' is the adatom bonded to the step edge. The jump rate (Γ) of diffusion of adatoms between adsorption sites is defined as:

$$\Gamma = \nu \, e^{(-Ed / kT)} \tag{1.1}$$

Where T is substrate temperature, Ed is diffusion barrier, ν is attempt frequency, and K_b is Boltzmann's constant. The diffusion coefficient is described as:

$$D = 1 / 4 \; a^2 \Gamma = 1 / 4 \; a^2 \nu \, e^{-Ed / kT} = D_0 \, e^{-Ed / kT} \tag{1.2}$$

Where a denotes the separation between adsorption sites, and 1/4 is the 2D nature of surface diffusion. Both E_d and D_0 are factors of surface diffusion. The term diffusion barrier (E_d) arises due to the atomic structure of the surface. The diffusion barrier varies in different materials and even within the same materials, depending on the surface orientation. There are different diffusion barriers in different directions depending on the surface structure [25].

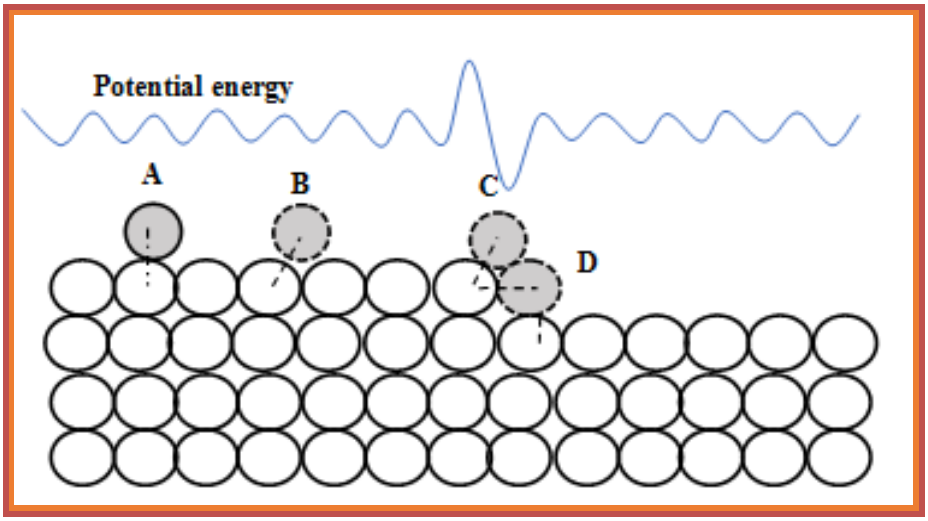

***Figure 1.5**: Depiction of P_E profile faced by adatoms [22].*

(3) Nucleation of adatoms

Nucleation is a widespread phenomenon in all depositions. It is a primary process that occurs during the formation of crystals or thin films from matter (solid, liquid, and vapour). Nucleation is the formation of a small cluster in which ions, atoms, and molecules are arranged in a specific pattern, creating a site for the deposition of new impinging atoms during crystal or thin film growth. Growth follows nucleation. These structures formed in nucleation are unstable, intermediate structures. Nucleation is described as small, tiny regions that grow into a solid crystal for further deposition of incoming atoms [26]. Impinging adatoms have a degree of mobility over the surface before nucleation. The nucleation density of adatoms refers to the amount of interface contact area or interface voids. Generally, for good thin film adhesion, a high nucleation density is required. The nucleation density is affected by many factors such as the KE of adatoms, nucleation sites, chemical reaction, diffusion with the surface, and surface mobility of adatoms. The nucleation density may increase for good thin film adhesion through energetic particle and plasma bombardment, which enhances surface mobility, accelerates chemical reactions and diffusion by heating, and creates surface defects by altering the surface chemistry [27].

(4) Interface formation

An interface is a boundary formed between two materials when they come into contact. Interfaces are formed on the surface during the nucleation process. Their formation continues throughout the whole deposition as well as in post-deposition processing. Interfaces are categorised into several types, including abrupt, mechanical abrupt, diffusion, compound, and pseudodiffusion interfaces. Each type of interface has different electrical, mechanical, and

thermal properties. An interface's reliability depends on the surface composition of materials, contact behaviour, and the process used to bring the materials in contact with each other. An abrupt interface is called abrupt because neither a diffusion process nor a reaction occurs. It is formed due to the abrupt transition of one material to another in place of lattice parameters at a distance of 0.2–0.5 nm [23].

In the formation of an abrupt interface, there is a large gradient in material properties and a reduction in nucleation density. Interfacial voids may occur due to a lack of nucleation growth at the abrupt interface. The changes produced in an abrupt interface result in the formation of a mechanical abrupt interface. This interface offers good adhesion if a rough surface is filled in and interfacial voids are avoided. A diffusion interface forms due to interdiffusion between the film and substrate materials. The disadvantage of a diffusion interface is the creation of voids due to a mismatch in the diffusion rates of the film and substrate materials [28].

Temperature, time, and pressure are necessary for the diffusion of atoms in materials. The extent of diffusion varies with changes in time and temperature. A diffusion interface is mainly found in metallic systems. This type of interface provides good adhesion; however, if the diffusion of atoms in one direction exceeds that in the other direction, it creates voids in the material, which lose excessive atoms and become weakened. In a compound interface, when materials are brought too close to each other, one or more layers of the compound are formed. These compound layers are formed by chemical, metallurgical, and solid-state reactions.

Compound interfaces may be brittle. Generally, they provide good adhesion between materials; however, if voids and microcracks form, the interface weakens, leading to poor adhesion [13,17]. This is a primary concern in the field of interfacial regions [29].

(i) Island structure

During the growth of nuclei and the formation of grains, numerous processes occur. For a positive net growth rate, atoms continuously attach to and detach from grains. Atoms are connected either by vapour or by diffusion of adatoms. It is necessary to understand what happens with different-sized grains on the surface without any deposition. In isolated grains, atoms attach and detach constantly, and as a result, a net change occurs in the size of the isolated grains. There is always a 2D cloud of adatoms in a grain. The island has larger nuclei with diameters greater than 10 Å.

There is an inverse relation between the binding energy of surface atoms and grain size. Additionally, small grains have a high adatom density, while larger grains have a low adatom density. If there are two grains of different sizes, then the adatom density of each will be different (i.e., one with high density and the other with low density). If there is a difference in adatom densities, then atoms flow from the greater density around the small grains to the lesser adatom density around the larger grains. Consequently, this results in a net increase in atoms for large grains and a net decrease in atoms for small grains, a process known as Ostwald ripening [30, 31].

(ii) Coalescence of Islands with gaps

Developing islands will eventually meet. As two growing islands are close to each other, they interact and reconstruct to minimise energy in the system. A grain boundary is formed as a result of the deformation of impinging islands. The coalescence is defined as the significant transfer of mass between islands by diffusion. Small islands disappear. Both recrystallisation and annealing occur during the coalescence of two islands to produce larger islands with a defined shape. The coalescence time is very minimal, approximately 0.6 s [32].

(iii) Channel and holes

After the coalescence process, a film with a channel is formed with continuous deposition. Within the channel, secondary nuclei are grown in void spaces. Further deposition is responsible for the formation of new islands and increases the size of the nuclei as well as film thickness [22]. These new islands merge with the main island or aggregate by filling in the gaps. However, these gaps are not filled in and decrease with increasing film thickness.

(5) Continuous thin film

After the bridging of gaps, a final continuous film is obtained. Some void spaces may be present practically, but an ideal continuous film doesn't contain any gaps. The minimum thickness of the film depends on the nature of the deposits [26].

1.2.5. Characterisation techniques of Nanostructured Thin films

It becomes essential to deposit nanomaterials on the surface of the solid substrate in the form of thin films. Thin film materials are the primary elements of ongoing technological advances in the fields of optoelectronics, photonics, and magnetic devices. Producing materials into thin films enables easy integration into various types of devices [34]. Thin film technology is the basis of surprising development in the solid-state electronics research area [35]. Thin film studies have directly or indirectly advanced many new areas of research in

solid state physics and chemistry, which are based on phenomena uniquely characteristic of the thickness, geometry, and structure of the film [36].

Materials science researchers consider thin films to be commonly associated with semiconductors. Thus, these are significant in a multiplicity of other research fields where coatings are only 50-100 nm thick. The thin film is essential because it amends the surface interactions of the newly made platform from the bulk substrate properties [37].

Once a thin film is produced, it becomes necessary to characterise [38]. An important issue is the correct interpretation of the experimental outcomes obtained through characterisation tools. Therefore, it is essential to characterise the physical, structural, and optical properties of the materials to qualify them as nano materials [39]. Characterisation and outcome reporting are fundamental to the development of nanoscience. The measurements are accompanied by several tools, including instruments, machines, computer hardware, and software [40].

Various analytical techniques were used to characterise the nanomaterials and thin films [41]. The characterisation technique can also be classified into two types: spectroscopic and microscopic techniques. Spectroscopy is a branch of science which deals with the interaction of electromagnetic radiation with matter. It is one of the most powerful tools available for studying atomic and molecular structure and is used in the analysis of a wide range of samples. Table 1.1 provides a list of methods, along with a brief indication of the information that can be obtained from each sample. The techniques are organised by the nature of the incident or probe beam used to initiate the information process.

1.2.6. Properties of nanostructured thin films

1.2.6.1. Thin film structure

Different and complex chemical reactions occur during the deposition process, depending on the technique employed and deposition parameters such as substrate temperature, deposition rate, pressure, and the alignment of the vapour stream with the substrate, which give rise to a variety of microstructures. The resulting microstructure, in turn, defines the physical and chemical properties of the film, which means that an appropriate management of these variables is essential to obtain tailored film properties. The resulting microstructure can be either amorphous, polycrystalline or epitaxial, which are briefly described below [42].

a. **Amorphous thin films**

The growth of amorphous thin films occurs at low substrate temperatures, where the mobility of adatoms (adsorbed atoms) at the substrate surface is minimal [43]. Therefore, at low temperatures, the adatoms approach thermal equilibrium with the substrate.

Table 1.1: *Thin films characterisation methods ordered by incident or probing beam.*

Probing beam	Characterisation techniques	Main information (Utility)
Photons	X-ray photoelectron spectroscopy (XPS)	Surface composition (Li and heavier), surface chemical state
	X-ray diffraction (XRD)	Film crystal structure and phase
	X-ray reflectance (XRR)	Film thickness and interface roughness
	Laser Raman Fourier transform infrared spectroscopy (FTIR)	Molecular structure
		Molecular structure
	Ellipsometry	Film thickness
	Photoluminescence spectroscopy	Luminescence properties
ions	Rutherford backscattering spectrometry	Film composition, film thickness, elemental profiles, and information about the interface.
	Nuclear reaction analysis	Specific isotope composition and distribution
	Ion channeling	Crystalline quality and defect (impurity) locations, information about the interface.
	Elastic recoil detection analysis	Light element concentration and depth distribution.
	SIMS/Nano-SIMS/TOFSIMS Low-energy ion scattering	Molecular and elemental species.
		Outer surface composition, surface structure
	Glow discharge mass spectrometry	Depth profile
	Focused ion beam	Ion-induced EDS, secondary ion microscopy, ion-induced secondary electron microscopy, nanolithography (site-specific cross-sections), film surface cleaning.
	Auger electron spectroscopy	Surface elemental (and chemical state) composition
	Scanning electron microscopy	Surface topography, film thickness?
	Transmission electron microscopy	Microstructure, chemical information, film thickness?
	Low-energy electron diffraction	Surface structure
	Energy-dispersive X-ray spectroscopy	Composition and composition distribution
Other Methods	Scanning probe methods (STM, AFM, etc.)	Topography, electronic structure, site-specific information
	Atom probe microscopy	Atom distributions

limiting the energy available for diffusion through its surface. Instead, these nearly immobile adatoms are incorporated at the point of strike with the substrate surface.

A high deposition rate is another parameter that induces amorphous growth, as it prevents adatoms from migrating to more energetic sites and reaching equilibrium due to the limited time for diffusion. Consequently, they are incorporated into the film structure almost immediately upon striking the substrate surface.

Some developments have also reported the formation of this disordered microstructure by the incorporation of certain gases, such as oxygen and nitrogen, which inhibit the growth of crystallites during the deposition process [44]. Both PVD and CVD techniques are suitable for depositing amorphous structures. The deposition of amorphous thin films is required in various applications, including solar cells, transistors, optoelectronics, and dielectric films.

***b.* Polycrystalline thin films**

They consist of a large number of nano- or micro-crystallites with different orientations, separated by grain boundaries. The crystallite size is primarily determined by the deposition parameters, specifically the deposition temperature and deposition rate. A deposition temperature higher than that required to obtain amorphous structures may lead to the formation of polycrystalline thin films. When adatoms are not in thermal equilibrium with the substrate due to a high substrate temperature, they have sufficient energy to continue diffusing on the substrate surface until they adhere to an existing island or form new islands. These islands do not become thermodynamically stable until their size reaches a critical threshold for nucleation. The stable islands continue to grow until saturation, and then undergo a coalescence process. Thin films initiate between islands, giving rise to the formation of a polycrystalline layer [45]. As adatom diffusion is a temperature-dependent process, the crystallite size is expected to increase in line with the increase in substrate temperature. Another driver for the crystallite size is the film thickness. While the coalescence process limits crystallite growth in the lateral direction, growth in the cross-plane direction is limited by the film thickness. The typical microstructure of this material is of great importance for some applications where the scattering of carriers and phonons needs to be controlled, i.e. thermoelectrics [46, 47].

***c.* Epitaxial thin films**

They consist of a solid crystalline film deposited onto a substrate surface with a nearly perfect lattice structure, whose crystal orientation is aligned with the crystallographic orientation of the substrate surface. Depending on the nature of the substrate, the epitaxial growth can be divided into homo and hetero-epitaxial, with the former referring to the growth of a film onto a substrate of the same material, and the latter, onto a substrate of different material. Various deposition techniques have been developed to enable the deposition of epitaxial films, including MBE and vapour-phase epitaxy; they are mostly used in the semiconductor industry, where high-quality and complex films, such as quantum wells and quantum wires, are required [48]. Achieving epitaxial film growth depends on several factors, including the equilibrium thermodynamics of nucleation, the creation of vapour from reactants, substrate surface reactions, and the mobility of species through the substrate surface. The complex interaction of these atomic processes may lead to the formation of epitaxial films only if they occur over a specific temperature called the "epitaxial temperature", which depends on the particular system and deposition parameters. Epitaxial growth typically occurs at high substrate temperatures to promote the mobility of adatoms on the substrate surface, forming islands that become stable after reaching a specific size. The continuous growth of these islands increases the nucleation density, resulting in a solid film with a preferential orientation. The quality of epitaxial growth is strongly influenced by the strain created in the film during deposition due to lattice misfit and thermal strain produced as a result of the different coefficients of thermal expansion between the film and the substrate. Substrate surface contamination also influences the growth by interrupting the formation of epitaxial layers. To avoid this, deposition is typically carried out under reduced pressures or in a vacuum to promote the effusion of impurities from the substrate.

1.3.2. Thin film morphology

It is challenging to establish a relationship between the morphology of deposited thin films and the deposition parameters because of the interaction of several elements that affect the nucleation and growth phases. However, the most common morphological feature is probably a columnar structure whose growing direction is not necessarily perpendicular to the substrate [42]. The way the adsorbed atoms are integrated into the growing process determines the final morphology of thin films. When the atoms strike the substrate surface, they may contribute to the creation of islands. These islands increase in size due to the feeding of atoms coming from the diffusion in the substrate surface and also from the vapour flux, forming complex arrangements of islands or compact islands. The flux of atoms diffusing in

the substrate is suppressed once the islands start an interfering process with each other due to progressive growth, and only the contribution from the vapour flux remains active, shifting the growth in the thickness direction. The accumulating growth in the thickness direction gives rise to a columnar structure with a cauliflower-like appearance in the top view [43, 45, 49].

The evolution of the morphology in thin films as a function of substrate temperature (adatom mobility) can be classified according to the structure zone model [50]. This model provides three structural zones depending on a homologous temperature (T_h), which results from the ratio between the substrate temperature (Ts) and the melting point temperature of the deposited material [42]:

(i) In zone I for a $T_h \leq 0.3$, the relatively low substrate temperature allows for a low diffusion of adatoms, which is not enough to compensate for the density of defects. As a result, amorphous or nano-crystalline columns with a high density of defects between them are formed with a cauliflower-like appearance on the top surface, which is enhanced by the shadowing process;

(ii) In zone II for $0.3 < Th < 0.5$, with a higher substrate temperature, the diffusion of adatoms is higher and enough to compensate for the defects, producing a columnar structure with a lower concentration of defects and larger.

(iii) In zone III, where $Th > 0.5$, the higher substrate temperature produces a dominant bulk diffusion in the layer, giving rise to a structure formed by coarse crystallites [51].

1.3. Nanostructured metal oxide

1.3.1. Introduction

The progress in nanoscience and nanotechnology has opened a new opportunity for the application of nanostructured materials in solar cells, energy storage devices, biological activities, and spintronic applications, due to their highly tunable size and shape dependent chemical and physical properties [52]. In recent years, an extensive research is assigned for the development of functional materials into organized nanostructures. The novel approaches of following nanoarchitectonics materials and related concepts as well as atom or molecular-controlled systems and novel design of individual nanomaterials to demonstrate the possible of nanoarchitectonics for the future nanotechnology research [53, 54].

Nanostructured metal oxides (NMOs) have been identified as an essential class of functional materials, attracting considerable attention not only for fundamental scientific research but also for diverse practical applications due to their unique physical and chemical properties [55]. These properties are strongly dependent on the sizes, shapes, compositions, and structures of the nanocrystals. Interesting phenomena, such as a remarkable increase in surface-to-mass ratio, a significant change in surface energy, and quantum confinement effects, occur at the nanoscale dimension. Therefore, the manipulation of well-controlled synthesis and manufacture of NMOs with different sizes, shapes, chemical compositions, and structures is crucial in the advancement of nanoscience and nanotechnology.

Among all the NMOs, copper oxide nanomaterials have been widely studied for their interesting semiconducting and optical properties. Nanostructured copper oxide thin films are inorganic compound materials (semiconductors of interest) that have been studied for more than three decades due to the abundance of their constituent elements and their unique properties, leading to several applications. Low-dimensional copper oxide nanostructures are very promising building blocks for various functional materials targeting high-demand applications in the fields of sensing, optoelectronics, catalysis and solar cells [56]. Nanostructured CuO is an interesting material because it is possible to tune the band gap due to quantum confinement when the dimensions of the nanostructures approach the exciton radius [57]. It is observed that nanostructured CuO materials have the advantage of a lower surface potential barrier than metals, which affects electron field emission properties and plays a crucial role in optoelectronics and solar cells. Its various industrial applications indicate that CuO magnetic nanostructures are of particular importance among the semiconductor 3d oxides.

CuO nanostructures differ from other transition metal monoxides, such as FeO, NiO, CoO, and MnO, due to their monoclinic crystal structure and unusual temperature-dependent magnetic susceptibility. Furthermore, it is essential to consider the significant changes in its magnetic properties as the particle size varies [58]. However, magnetism in CuO nanostructures has not been extensively studied.

1.3.2. Copper oxide nanostructures: Literature review

2.3.2.1. Fundamental Properties

The reduction of CuO dimensions to the nanoscale results in considerable variation of its physical and chemical properties as compared to its bulk counterpart due to the “quantum-

size" effects [55]. Therefore, comprehending the fundamental properties of CuO nanostructures is crucial for their synthesis and applications, as well as for The rational design of functional devices based on CuO nanostructures. In this section, we will focus on the fundamental physical properties of CuO nanostructures, including crystal structures, optical, electrical, and magnetic properties. The summary of the fundamental physical properties of CuO material is shown in Table 1.2.

Table 1.2: *Key physical properties of CuO at room temperature [59-61].*

Parameter properties	**value**
Molecular Formula	CuO
Appearance	Black powder
Solubility in water	Insoluble
Molecular mass	79.545 g/mol
Density	6.315 g/cm^3
Melting point	1326°C
Refractive index	2.63
Direct energy band gap	1.2 eV
Hole mobility	0.1 - 10 cm^2/Vs

1.3.2.2. Crystallographic structure

The monoxide CuO has much more complicated tenorite crystal structure. The monoclinic unit cell with C2/c symmetry contains four CuO molecules (Figure 1.6). The atoms coordination is that each atom has four nearest neighbors of the other kind. as shown in figure 2.1, in the (110) plan, each Cu atom (the big turquoise spheres) is linked to four nearest O atoms at the corner of an almost rectangular parallelogram [62]. While, each O atom (the small red spheres) is coordinated to four Cu atoms in the form of a disorder tetrahedron. Lattice constants and other crystallographic properties are listed in Table 1.3.

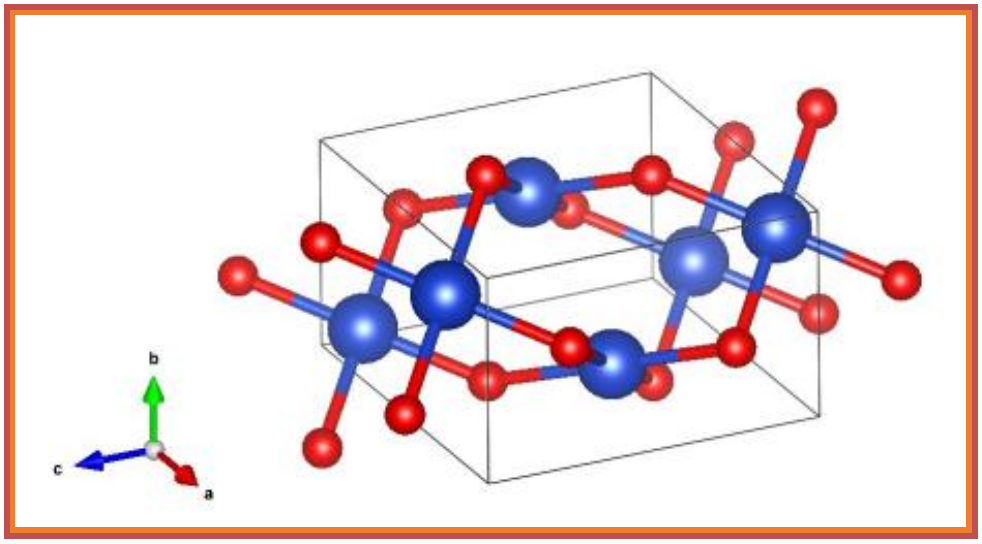

***Figure 1.6**: Crystal structure of the unit cell of CuO [62].*

***Table 1.3:** Crystallographic properties of CuO at room temperature.*

Parameter	**value**
Crystal structure	Monoclinic
Space group	C_{2h}
Lattice constants	*a* (Å) = 4.6837, *b* (Å) = 3.4226, *c* (Å) = 5.1288
	β (degree) = 99.54°, α = γ = 90°
Cell volume	81.08 Å
Cell content	4 [CuO]
Distances	
Cu–O	1.96 Å
O–O	2.62 Å
Cu–Cu	2.90 Å

1.3.2.3. Optical Properties

Compared with bulk CuO, various shapes of nanostructured copper oxide (CuO) have been reported for nanostructured copper oxide fabricated by simple modulation of the reaction conditions [63]. In fact, flower-like, boat-like, plate-like and ellipsoid-like morphologies were observed when controlling the reactants, reaction temperature, and reaction duration. The observed UV–visible diffuse reflectance spectra and estimated bandgap energy for each shape

of CuO is presented in Figure 1.7. The band gaps of the flower-, boat-, plate-, and ellipsoid-like CuO products were estimated by the authors to be 1.425, 1.429, 1.447, and 1.371 eV, respectively. The effect of the morphology of CuO nanostructures on their band gaps is demonstrated.

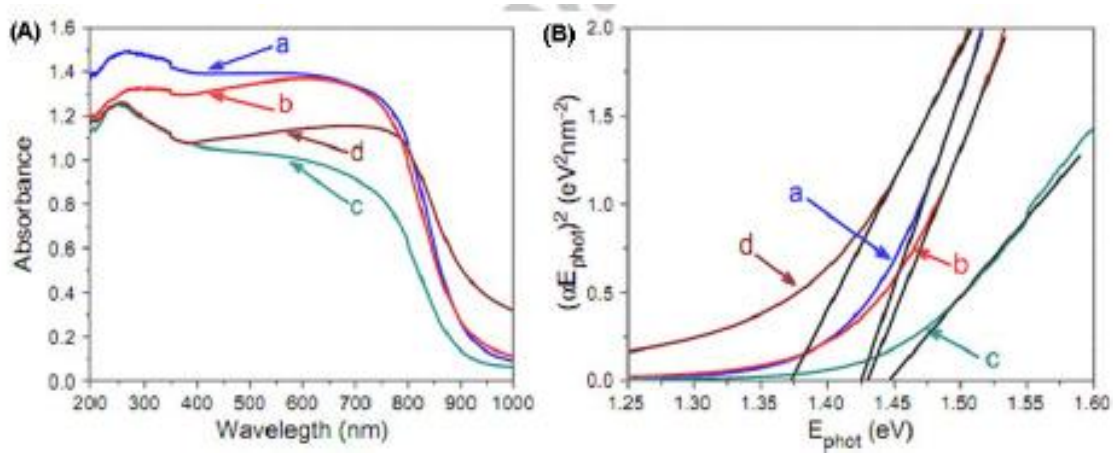

Figure 1.7: *(A) UV–visible diffuse reflectance spectra and (B) Plots of $(\alpha E_{phot})^2$ versus E_{phot} for (a) flowerlike,(b) boat-like, (c) plate-like, and (d) ellipsoid-like CuO nanostructures [63].*

Yang et *al.* [64] also synthesised different scales and shapes of nanostructured CuO by a simple solution-based method. Crystallite size and morphology are controlled by modulating the molar ratio of NaOH to Cu(NO3)2, reaction temperature, and the concentration of the starting NaOH solution. The absorption edge is blue-shifted to shorter wavelengths with reduced size and changed morphology. This result indicates that not only the size but also the morphology of the CuO nanocrystals affects the bandgap.

Additionally, photoluminescence (PL) spectra of CuO nanostructures are also comprehensively reported and reviewed in [55]. Gaashani et *al.* [65] achieved different morphologies and sizes of CuO nanostructures by rapid thermal decomposition of Cu nitrate [$Cu(NO_3)_2$] under ambient conditions, in which the size and morphology of the nanostructures were controlled by changing the temperature and the duration of the decomposition process. The observed PL spectra of (a) the CuO samples prepared at a fixed time (20 min) for various temperatures and (b) the CuO samples prepared at a fixed temperature (400 °C) for different times are similar. PL spectra of all samples have three main broad emission bands centred at ~305 nm (4.07 eV), 505 nm (2.46 eV), and 606 nm (2.05 eV). The PL peak at ~305 nm (4.07 eV) is related to the band-edge emission of CuO nanostructures. The three strong emission peaks, located at 489 nm (2.54 eV), 505 nm (2.46 eV), and 525 nm (2.37 eV), are attributed to band edge emission from the new sublevels at 300 K or possibly to defects present in the CuO

nanostructures. The emission bands extending from 585 nm to 625 nm correspond to deep-level defects of CuO.

Other emission peaks, centred at ~680 nm (1.81 eV) and 714 nm (1.74 eV), as well as an IR band at ~760 nm, are observed in CuO nanoparticles, nanorods, and nanofibrils, respectively [65-69]. The PL peak located at 685 nm (1.81 eV) is correlated to the interstitial in CuO. In contrast, the peak at 714 nm (1.74 eV) is attributed to the recombination of electrons and holes at oxygen vacancies. The peak observed at 760 nm can be attributed to the specific surface effect, which causes a red shift in the PL emission. In summary, the PL properties of CuO nanostructures can be controlled by their morphology, dimension, and shape. Quantum confinement effect and specific surface effect are the two most reported mechanisms, which can result in the blueshift and redshift of the PL peak, respectively [65]. Thus, considering these parameters in the design of CuO-based photo-electronic devices is essential.

1.3.2.4. Electrical Conductivity

For p-type MO semiconductors, the charge carriers based on a considerable concentration of the free holes existing in their VBs are widely accepted. The concentration of the free holes in these materials is mainly determined by the metal deficit concentration (or excess oxygen) within the crystallite sites of the materials [70,71]. This phenomenon is attributed to the deviation from the stoichiometric composition of the components, which can be induced by regulating the preparation conditions of the material [72].

Structural factors, including grain size, grain boundary, film thickness, specific phase, and dopants, also remarkably influence the conductivity of a material [73,74]. Consequently, both the synthetic techniques and growth conditions can strongly affect the electrical properties of CuO. For example, a CuO film prepared by a chemical solution deposition technique from acetate and sintered at 300°C to 600°C exhibits a conductivity range of 10^{-2} S/cm to 10^{-3} S/cm. However, film conductivities prepared using Cu 2-ethylhexanoate and naphthenate are 10^{-6} to 10^{-4} and 2×10^{-3} to 10^{-5} S/cm, respectively [55]. These results showed that the conductivity of doped CuO thin film increases when doped with Li^{+} and decreases when doped with Al^{3+} [55].

Changing the synthesis parameters, thickness, and roughness of samples can also vary the resistivity of the prepared CuO samples. Resistivity reportedly increases with the

thickness and deposition temperature of the CuO sample due to the irregular grains (or aggregates) that contribute to more trapping and scattering of free charge carriers [74]. Jundale et *al.* [75] also observed a similar trend in the electrical conductivity of CuO prepared by the sol-gel method and subsequently sintered at various temperatures ranging from 300 °C to 700 °C. The room temperature electrical conductivity of CuO increased from 10^{-6} $(\Omega cm)^{-1}$ to 10^{-5} $(\Omega cm)^{-1}$ with an increase in annealing temperature from 300 °C to 700 °C because of the removal of H_2O vapour, which may resist conduction among CuO grains. Moreover, electron density (n) and mobility (μ) also increased with the increase in annealing temperature and were estimated to be of the order of 4.6×10^{19} cm^{-3} to 7.2×10^{19} cm^{-3} and 3.7×10^{-5} $cm^2 V^{-1}s^{-1}$ to 5.4×10^{-5} $cm^2V^{-1}s^{-1}$, respectively. The enhancement was due to the temperature-dependent carrier scattering mechanism, which was driven by the intergrain barrier potential.

Moreover, carrier motilities tend to significantly decrease when going from single crystals to polycrystalline and nanocrystalline materials due to scattering at grain boundaries and energy barriers at these boundaries [76]. Other factors, such as lattice strain and crystal distortions, can also affect the charge movement, resulting in an increase in the resistivity and a decrease in conductivity [77].

1.3.2.5. Magnetic Properties

The bulk transition metal monoxides, including MnO, FeO, CoO, NiO, and CuO, are all antiferromagnets, where CuO occupies a special place because its unique magnetic properties. Bulk CuO is antiferromagnetic with Néel temperatures from 213 K to 230 K [78]. However, although the preliminary magnetisation measurements performed by Avoni et al. in 1992 suggest the presence of weak ferromagnetism, which may explain the unusual behaviour of the single-crystal bulk CuO susceptibility [79].

Anomalous ferromagnetic behaviour is observed for different CuO nanostructures. Punnoose et *al.* [80] investigated the magnetic properties of CuO nanoparticles with a nominal size range from 6.6 nm to 37 nm synthesised by the sol–gel method combined with high-temperature annealing. For nanoparticles with a diameter (d) <10 nm, a more rapid lattice expansion exists, and the magnetic susceptibility varies as $1/d$, accompanied by a weak ferromagnetic component and hysteresis loops. For nanoparticles greater than 10 nm, the magnetic ordering is essentially similar to the antiferromagnetic ordering of the bulk CuO [80]. For CuO nanoparticles <10 nm, the surface spins are expected to dominate the measured magnetisation because of their lower coordination and uncompensated exchange couplings.

Consequently, a weak ferromagnetic behaviour is observed. Rao et *al.* also studied the magnetic properties of CuO nanoparticles synthesised by thermal annealing of $Cu(OH)_2$ with average particle diameters ranging from 13 nm to 33 nm. Their magnetic measurements reveal the presence of a weak ferromagnetic interaction and blocking behaviour in these CuO nanoparticles, which is caused by the existence of uncompensated surface spins [81].

The magnetic properties of nanostructures depend not only on size but also on the morphology and anisotropy of nanostructures. Xiao et *al.* investigated the magnetic properties of CuO nanorods with diameters ranging from 30 nm to 40 nm and lengths from 100 nm to 200 nm, which were hydrothermally synthesised in the presence of sodium citrate [82]. The CuO nanorods with a much larger diameter than 10 nm exhibit an obvious anomalous ferromagnetic behaviour in the 5 K to 300 K range, in which the effect of the morphology of CuO nanostructures plays a key role in the magnetic properties. Dar et al. studied the magnetic properties of CuO nanoneedles synthesised by a simple hydrothermal method. Their measurements using a superconductor quantum interference device magnetometer also reveal the ferromagnetic behaviour of the CuO nanoneedles, in which the coercivity of CuO nanoneedles at 3 K was estimated to be 42 Oe [83].

Recently, room temperature ferromagnetism has been observed in pure CuO nanostructures. For example, Shang et *al.* synthesised straw-like CuO nanostructures (nanostraws) on a Cu foil substrate through a simple solution method and demonstrated that room-temperature ferromagnetism is associated only with the nanostructures (not the microscale CuO film) [84]. Gao et *al.* studied the room-temperature ferromagnetism of flower-like CuO nanostructures prepared by the co-precipitation method with post-annealing in air, confirming that the observed room-temperature ferromagnetism in flower-like CuO nanostructures might originate from oxygen vacancies [85]. In another study from the same group, room-temperature ferromagnetism is observed in pure CuO nanoparticles prepared by the precipitation method without any ferromagnetic dopant.

1.3.3. Transition metal-doped CuO nanostructures

Accordingly, the synthesis of copper oxide nanoparticles (NPs) becomes imperative. Cu^{+}, Cu^{2+}, and Cu^{3+} are the three oxidation states that can occur in copper (Cu), and metal oxide nanoparticles (NPs) can be doped with both kinds of electrons and holes [86]. The electrical configuration of the host material (CuO) can be modified by carefully doping

transition metal ions into it, which improves the conductivity and physical characteristics of the resulting synthetic nanoparticles.

The magnetic properties of nanostructured oxides span from diamagnetic, paramagnetic, to ferromagnetic and antiferromagnetic, and their chemical reactivity can be tailored from being extremely reactive to inert. All these promising properties originate from the strong and competitive exchange coupling between charge, orbital, lattice, and spin degrees of freedom in these oxide materials [87]. Following the theoretical predictions by Dietl et *al.* [88], numerous studies have sought magnetic semiconductors with Curie temperatures above room temperature, utilising various host semiconductor materials doped with 3d transition metals. Theoretical models of magnetism in DMSs have suggested that ferromagnetic ordering in DMSs is stabilised by exchange interactions between the magnetic dopants and additional free or defect-bound charge carriers [89]. Table 1.4 gives a brief comparison of the main features of the magnetic interactions in DMS (see Appendix).

***Table 1.4**: Main magnetic interactions in DMSs.*

Interaction	**Description**
Direct super-exchange	Direct coupling of magnetic ions through the overlap of magnetic orbitals.
Indirect super-exchange	Spins of two magnetic ions are correlated.
RKKY	Indirect exchange coupling of magnetic moments over relatively large distances via band electrons due to Coulomb exchange. It becomes efficient when a high concentration of free carriers is present, such as in metals for which it was developed.
Double exchange	Couples of magnetic ions in different charge states by virtual hopping of the extra electron from one ion to the other through interaction with p-orbitals.

Doping makes profound changes in optical, magnetic and magneto-transport properties of CuO by modifying its electronic structure. Electrical, optical, excitonic, spectroscopic and neutron diffraction studies on pristine and doped CuO with Mn, Ni, Fe, Co, and Cr have been studied [86]. Kumar et *al.* reported the existence of weak ferromagnetism in the sol–gel derived Ni-doped CuO NPs ($Cu_{1-x}Ni_xO$) [90]. Rietveld refinements of the XRD patterns and Raman spectra corroborated the single monoclinic DMS phase of Cu1-xNixO,

with a crystallite size ranging from 19 to 21 nm. The energy band gap for these NPs was found to decrease (i.e., red-shifted) from that of pure CuO (1.43 eV). The weak magnetic nature induced in the DMS phase is possibly due to the exchange interaction between the localised magnetic d-spins of dopant ions and the charge carriers from the valence band of pure CuO. The existence of inter-grain magnetic interactions and hence the induction of weak magnetism in this DMS phase is also supported by the quantified value of the squareness ratio, which has a value less than 0.5.

1.3. Conclusion

Nanostructured materials have attracted much attention from scientists and engineers due to their unique and novel physical and chemical properties. The development of available and cheap methods for their synthesis and characterisation techniques contributed not only to the miniaturisation of new devices and systems but also opened up new possibilities for modern technologies.

In this chapter, we classified nanomaterials based on their dimensionality. Each class exhibits specific and unique properties and can be tuned by morphology and fabrication methods. Further, we focus on different properties of nanostructured thin films in terms of their production and characterisation. This information will help researchers and scientists design novel and innovative materials with enhanced properties as nanostructured DMOs. Finally, an overview of previous studies on nanostructured undoped and doped copper oxide thin films is presented.

References

[1] R. Feynman, There Plenty of Room at the Bottom, (1959).
[2] F.A. Cupaioli, F.A. Zucca, D. Boraschi, L. Zecca, Prog. Neurobiol., 119 (2014) 20.
[3] F. Findik, Period. Eng. Nat. Sci. 62 (2021) 75.
[4] B. Mekuye, B. Abera, Nano Select., 4 (2023) 486.
[5] N. Joudeh, D. Linke, J. Nanobiotechnology, 20 (2022) 262.
[6] V.V. Pokropivny, V.V. Skorokhod, Physica E, 40 (2008) 2521.
[7] Jeevanandam J., Barhoum A., Chan Y.S., Dufresne A. Danquah M. K., Beilstein J. Nanotechnol., 9 (2018) 1050.
[8] J.N. Tiwari, R.N. Tiwari, K.S. Kim, Prog. Mater. Sci., 57 (2012) 724.
[9] Y. Xia, P. Yang, Y. Sun, Y. Wu, B. Mayers, B. Gates, Y. Yin, F. Kim, H. Yan, Adv. Mater. 15 (2003) 353.
[10] M.B. Tahir, T. Nawaz, G. Nabi, M. Sagir, M.A. Shehzad, A. Yasmin, S. Hussain, M.P. Bhatti, A. Ahmed, S. Gilani, Int. J. Environ. Anal. Chem., (2020) 1.
[11] S. Lindsay, Introduction to Nanoscience, Oxford University Press, Oxford, 2010.
[12] R. D. Prasad, A. K. Sahoo, O. P. Shrivastav, N. Charmode, S. R. Prasad, R. Kamat, N. G. Kajave, J. Chauhan, S. Banga, U. Tamboli, M. S. Pandharpatte, R. H. Atigre, V. Shaikh, M. N. Padvi, P. Salvalkar, N. R. Prasad, ES Food & Agroforestry, 8 (2022) 12.
[13] M. Ruoho, J. P. Niemelä, C. Guerra-Nunez, N. Tarasiuk, G. Robertson, A. A. Taylor, X. Maeder, C. Kapusta, J. Michler, I. Utke, Nanomaterials, 10 (2020) 558.
[14] M. Benelmekki , A. Erbe. In: Nanostructured Thin Films, (2019) Published by Elsevier Ltd, .ISBN 978-0-08-102572-7.
[15] J. Budida, K. Srinivasan, Materials Today: Proceedings, 92 (2023) 1030.
[16] A.T. Petkoska, I. Nasov, Zastita Materijala, 55 (2014) 3.
[17] J. E. Crowell, J.Vacuum Science & Technology A: Vacuum, Surfaces, and Films, 21 (2003) S88.
[18] G.D. Sulka, Molecules, 28 (2023) 4040.
[19] M. Saeed, Y. Alshammari, S. A. Majeed, E. Al-Nasrallah, Molecules, 25 (2020) 3856.
[20] S. J. C. Irvine, Photochemical vapour deposition of thin films. Pauleau Y, Chemical Physics of Thin Film Deposition Processes for Micro- and Nano-Technologies. Dordrecht: Springer, (2002) 199-222.
[21] R. S. Pedanekar, S. K. Shaikh, K. Y. Rajpure, Current Applied Physics, 20 (2020) 931.
[22] M. Ghosh, A.Paul, R. Mandal, Comprehensive Materials Processing (Second Edition), 4 (2024) 39-60
[23] D. Mattox, J. Vac. Sci. Technol. A, 7 (1989) 1105.
[24] R.F. Bunshah, J.M. Blocher, Deposition Technologies for Films and Coatings: Developments and Applications, Noyes Data, (1982).
[25] D. Magnfalt, Fundamental Processes in Thin Film Growth: The Origin of Compressive Stress and the Dynamics of the Early Growth Stages, in, Linkoping University Electronic Press, 2014.
[26] S.B. Ogale, Thin Films and Heterostructures for Oxide Electronics, Springer Science & Business Media, Berlin, (2006).

[27] J. Greene, S. Barnett, J.-E. Sundgren, A. Rockett, Low-energy ion/surface interactions during film growth from the vapor phase: effects on nucleation and growth kinetics, defect structure, and elemental incorporation probabilities, in: Plasma-Surface Interactions and Processing of Materials, Springer, (1990) 281.
[28] M. Pfeifer, Materials Enabled Designs: The Materials Engineering Perspective to Product Design and Manufacturing, Butterworth-Heinemann, (2009).
[29] D. Mattox, R. Cuthrell, MRS Online Proc. Library Arch. 119 (1988).
[30] P.W. Voorhees, The theory of Ostwald ripening, J. Stat. Phys. 38 (1985) 231.
[31] W. Ostwald, Z. Phys. Chem., 34 (1900) 495.
[32] C.V. Thompson, Annu. Rev. Mater. Sci., 30 (2000) 159.
[33] W. Wu, Z. Chen, Johnson Matthey Technol. Rev., 61 (2017) 93.
[34] M. C. Rao, M. S. Shekhawat, Int. J.Mod. Phys.: Conference Series, 22 (2013) 576.
[35] Y. Yu, M. Gong, C. Dong, X. Xu, Next Nanotechnology, 3-4 (2023) 100028.
[36] M. Yu, X. Feng, Joule, 3 (2019) 338.
[37] J. J. Wang, D. Shi, Applied Energy, 208 (2017) 83.
[38] Z. Alhalili, Molecules, 28 (2023)3086.
[39] S. R. Prasad, S. B. Teli, J. Ghosh, N. R. Prasad, V. S. Shaikh, G. M. Nazeruddin, A. G. Al-Sehemi, I. Patel, Y. I. Shaikh, Eng. Sci., 16 (2021) 90.
[40] R. D. Prasad, R. S. Prasad, R. B. Prasad, S. R. Prasad, S. B. Singh, R. J. Prasad, P. Sinha, S. Saxena, A. K. Vaidya, S.B Teli, U. R. Saxena, A. Harale, M. B. Deshmukh, M. N. Padvi, G. J. Navathe, ES Energy & Environ., 23 (2024) 1087.
[41] S. Mourdikoudis, R. M. Pallares, N. T. K.Thanh, Nanoscale,10 (2018) 12871.
[42] E. Acosta, 'Thin Films/Properties and Applications', Thin Films. IntechOpen, (2021).
[43] M.Pelliccione: Evolution of Thin Film Morphology Modeling and Simulations / by Matthew Pelliccione, Toh-Ming Lu. 1st ed. 2008. ed. (New York, NY : Springer New York : Imprint: Springer, New York, NY, (2008).
[44] K. L. Choy, Prog.Mater. Sci., 48 (2003) 57.
[45] R.D. Gould, S. Kasap, A.K. Ray, In Springer Handbook of Electronic and Photonic Materials, ed. Safa Kasap and Capper Peter (Springer International Publishing: Cham, 2017).
[46] K. Valalaki, N. Vouroutzis, A.G. Nassiopoulou, J. Physics D: Applied Physics, 49 (2016) 315104.
[47] J. Ma, S. Sinha, J. App. Phy., 112 (2012) 073719.
[48] M. S Dresselhaus, G. Chen, M. Y Tang, R. G Yang, H. Lee, D. Z Wang, Z. F Ren, J. P. Fleurial, P. Gogna, Adv. Mater., 19 (2007) 1043.
[49] R. Messier and S. TrolierMcKinstry, In Encyclopedia of Materials: Science and Technology, ed. K. H. Jürgen Buschow, Cahn Robert W., Flemings Merton C., Ilschner Bernhard, Kramer Edward J., Mahajan Subhash and Veyssière Patrick (Elsevier: Oxford, 2001), pp. 9306-9313.
[50] A. Kameneva, Res. J. Pharm. Biol. Chem. Sci., 6 (2015) 951.
[51] P.A. Dearnley,T. Liskiewicz, In Encyclopedia of Tribology, ed. Q. Jane Wang and Chung Yip-Wah (Springer US: Boston, MA, 2013), pp. 3948-3960.
[52] K.Ariga, M. Li, G. J.Richards, J. P. Hill, J. Nanosci. Nanotechnol., 11 (2011) 1.
[53] K.Ariga, H.Ito, J. P. Hill, H.Tsukube, Chem. Soc. Rev., 41 (2012) 5800.
[54] K.Ariga, Y.Yamauchi, G.Rydzek, Q.Ji, Y.Yonamine, K. C. W.Wu, J. P. Hill, Chem. Lett. 43 (2014) 36.
[55] Q. Zhang , K. Zhang , D.Xu , G. Yang , H. Huang , F.Nie , C. Liu , S. Yang , Prog. Mater. Sci., 60 (2014) 208.
[56] M.J. Paul, R. Suresh, R. Marnadu , V. Balasubramani , Optic. Mater.,

31(2022)112732.
[57] O. Baranov, K. Bazaka,T. Belmonte , C. Riccardi , H. E.Roman , M. Mohandas, S. Xu, U. Cvelbar, ' I. Levchenko, Nanoscale Horiz., 8 (2023) 568.
[58] N. Sreeju, A. Rufus, D. Philip, J. Phys. Chem. Solids, 124 (2019) 250.
[59] J. Ghijsen, L.H.Tjeng, J.van Elp, H.Eskes, J.Westerink, G.A.Sawatzky, M.T. Czyzyk, Phys. Rev. B, 38 (1988) 11322.
[60] J.B.Forsyth, S. Hull, J. Phys.: Condensed Matter, 3 (1991) 5257.
[61] O.Madelung, Semiconductors: data handbook, Springer, Berlin, 2004.
[62] A.Sharma, M.Varshney, J.Park, T-K.Ha, K-H.Chae, H-J.Shin, RSC Advances, 5 (2015) 21762.
[63] M. Yang, J. He, J. Colloid. Interface Sci., 355 (2011)15.
[64] M. Yang, J. He, X. Hu, C. Yan, Z. Cheng, Environ. Sci. Technol., 45 (2011) 6088.
[65] R. Al-Gaashani, S. Radiman, N. Tabet, R. Daud. J. Alloys Compd., 509 (2011)8761.
[66] C. Jin, K Baek, S. Park, H.W. Kim, W.I. Lee, C. Lee, Solid State Commun., 150 (2010)1812.
[67] A. Aslani, V. Oroojpour, Physica B, 406 (2011)144.
[68] S-S. Chang, H-J. Lee, H.J.Park, Ceram. Int., 31 (2005)411.
[69] C-Y. Huang, Chatterjee, S.B. Liu, S.Y. Wu, C-L. Cheng, Appl. Surf. Sci., 256 (2010)3688.
[70] A.H. Jayatissa, K. Guo, A.C. Jayasuriya, Appl. Surf. Sci., 255 (2009)9474.
[71] I. Singh, R.K. Bedi, Appl. Surf. Sci., 257 (2011)7592.
[72] N. Banerjee, S. Kundoo, K.K. Chattopadhyay, Thin Solid Films, 440(2003) 5.
[73] T. Serin, Yildiz, Ş. H. Şahin, N. Serin, Physica B: Condensed Matter, 406 (2011)575.
[74] T. Serin, Yildiz, Ş.H. Şahin, N. Serin, Physica B, 406 (2011)3551.
[75] D. Jundale, P. Joshi, S. Sen, V.B. Patil, J. Mater. Sci: Mater. Electron, 23(2012)1492.
[76] G. Boschloo, T. Edvinsson, A. Hagfeldt, Chapter 8 - In: Soga T, editor. Nanostructured materials for solar energy conversion. 1st ed. Nagoya: Elsevier Science; (2007) 231.
[77] H. Zheng, J.Z. Ou, M.S. Strano, R.B. Kaner, A. Mitchell, K. Kalantar-zadeh, Adv. Funct. Mater., 21 (2011)2175.
[78] P. Brown, T. Chattopadhyay, J. Forsyth, V. Nunez, F. Tasset, J. Phys: Condens. Matter., 4281 (1991)4281.
[79] C. Azzoni, A. Paleari, G., J. Phys.: Condens. Matter., 4 (1992)1359.
[80] Punnoose, H. Magnone, M. Seehra, J. Bonevich, Phys. Rev. B, 64 (2001)1.
[81] G.N. Rao, Y.D.Y. Yao, J.W. Chen, G. Narsinga Rao, J. Appl. Phys., 105 (2009)093901.
[82] H-M. Xiao, L-P. Zhu, X-M. Liu, S-Y. Fu, Solid State Commun.,141 (2007) 431.
[83] M. Dar, Y.S. Kim, W.B. Kim, J.M. Sohn, H.S. Shin, Appl. Surf. Sci., 254 **(**2008)7477.
[84] D. Shang, K. Yu, Y. Zhang, J. Xu, J. Wu, Y. Xu, Appl. Surf. Sci., **255 (**2009)4093.
[85] D. Gao, G. Yang, J. Li, J. Zhang, J. Zhang, D. Xue, J. Phys. Chem. C, 114 **(**2010)18347.
[86] Bushra, M.Kashif, Khairullah, A. A.Khan, H.Sun, J.Yousaf, M. I. A.Shah, S.Hussain, J. Amir, Y.Jamal, T. Ahmad, Braz. J. of Sci., *3*(8) (2024) 1.
[87] N. Izyumskaya, Y. Alivov, H. Morkoc¸ Crit. Rev. Solid State Mater. Sci., 34(2009) 89.
[88] T. Dietl, Science, 287 (2000)1019.

[89] M. Bououdina, Y. Song, S. Azzaza, Nano-Structured Diluted Magnetic Semiconductors, Elsevier Ltd, (2016).

[90] A.Kumar, M. Kumar, P.C.Sati, M.K.Srivastava, S.Ghosh, S.Kumar, Curr.Appl. Phys. 32, (2021)24.

Chapter 2
Experimental procedure

Chapter 2

Experimental procedure

The spray pyrolysis technique (SPT) is the most commonly used method for synthesising nanostructured thin films. In this chapter, the details of the different experimental apparatus used for the preparation and characterisation of nanostructured $Cu_{1-x}Fe_xO$ thin films are presented.

2.1 Spray pyrolysis technique

2.1.1. Definition

Nanostructured thin films have been studied for many years. One of the most challenging tasks for researchers and engineers in nanotechnology and nanoscience is the need to observe, measure, and manipulate materials at the nanometer level. Different methods of production are used to optimise specific properties of nanostructured thin films and the suitability for scaling up. However, compared to the other techniques mentioned in Chapter 1, the SPT requires simple and inexpensive equipment. Its main advantages include the easy addition of doping materials, good reproducibility, a high film growth rate, chemical homogeneity in the final product, and the potential for deposition over large areas [1].

2.1.2. Principle of spray pyrolysis

SPT is used to deposit thin films onto substrates by spraying a liquid precursor or dispersion onto the complex-shaped substrate (Figure 2.1). A wide range of materials, including polymers, ceramics, metals, nanoparticles, and organic compounds, can be deposited using SPT, making it suitable for a diverse range of applications. The spray pyrolysis approach enables the growth of both dense and porous films, as well as powdered materials. This process roughly consists of several steps:

a) Preparation: The substrate, typically made of glass, metal, ceramic, or polymer, is cleaned thoroughly to remove any contaminants that could affect the quality of the thin film. The liquid precursor or dispersion, often referred to as a spray solution, is prepared by

dissolving or dispersing the desired material in a suitable solvent or carrier fluid to form a homogeneous solution or suspension.

b) Atomization: The spray solution is atomised into fine droplets using a spray nozzle or atomiser. Atomization can be achieved through various methods, including pneumatic atomization, ultrasonic atomization, and airless atomization. The size and distribution of the droplets can be controlled to attain the desired film thickness and uniformity.

c) Deposition: The atomised droplets are sprayed onto the substrate surface using a spraying device or system. The substrate may be held stationary or moved relative to the spraying device to achieve uniform coverage. Multiple passes may be made to build up the desired film thickness.

d) Drying or curing: After deposition, the sprayed coating undergoes drying or curing to remove the solvent or carrier fluid and solidify the thin film. The drying process can be carried out at ambient temperature or under controlled conditions, such as elevated temperature or reduced pressure, depending on the properties of the coating material and the desired film characteristics.

e) Post-treatment (optional): Depending on the specific application and requirements, the deposited film may undergo additional post-treatment steps, such as annealing, curing, or surface modification, to enhance its properties, adhesion, or performance.

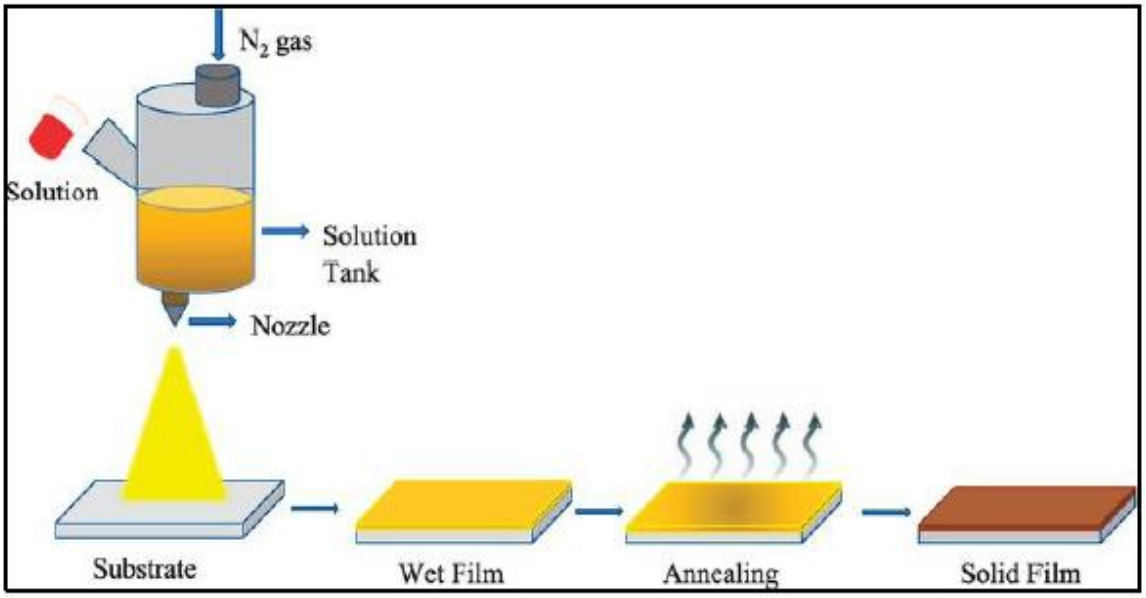

Figure 2.1: *Schematic diagram of spray coating method [1,3].*

2.1.3. Advantages

Apart from its simplicity, the spray pyrolysis technique has many advantages [1]:

(i) ***Versatility:*** Spray coating can be used with a wide range of materials, including polymers, ceramics, metals, nanoparticles, and organic compounds, making it suitable for diverse applications.

(ii) ***Scalability:*** Spray coating can be easily scaled up for large-scale production, making it suitable for industrial manufacturing processes.

(iii) ***Uniformity:*** With proper control of spraying parameters, spray coating can produce thin films with excellent uniformity and thickness control.

(iv) ***Ability to coat complex shapes:*** Spray coating can be used to deposit thin films on substrates with complex geometries or irregular surfaces, making it suitable for a wide range of applications.

2.2. Experimental conditions

2.2.1. Sample preparation

The materials used in the preparation of Fe-doped CuO thin films include copper(II) chloride dehydrate ($CuCl_2.2H_2O$, 99 %) as the copper precursor, iron(II) chloride ($FeCl_2$, 98 %) as the doping agent for introducing tin, deionized water (H_2O, >99 % purity), and ethyl alcohol (EtOH, 99.5 % purity) as solvents to dissolve the precursors and achieve homogeneous solutions. Glass substrates were used as the deposition surface for the nanostructured thin films. These chemicals were carefully selected for their purity and compatibility to ensure the formation of high-quality CuO thin films with controlled Fe doping concentrations. They were subsequently prepared via the spray pyrolysis method (SPT).

SPT involves several key steps, starting with the preparation of a precursor solution, followed by the deposition process, and the subsequent formation of thin films on glass substrates. The glass substrates were first ultrasonically cleaned to remove any contaminants and then placed on a heated substrate holder. The substrates were positioned 25 cm from the spray nozzle, and an air pressure of 2.5 bar was used to atomise the solution for spraying. The solution was sprayed onto the substrates at a constant flow rate of 1 mL/min. During the spraying process, the substrate was maintained at a constant temperature of 350 °C, which was monitored using a thermocouple. The deposition time was fixed at 5 min. The spray pyrolysis process allows for the formation of thin films, as droplets of the precursor solution,

when deposited onto a heated substrate, undergo pyrolytic decomposition, resulting in the formation of both pure CuO and Fe-doped CuO nanostructured films.

The deposition parameters outlined in Table 2.1 are critical for the growth of CuO thin films with controlled doping concentrations. The use of $FeCl_2 \cdot 2H_2O$ as the copper precursor, mixed with water and ethanol, ensures the proper solubility and evaporation rate necessary for efficient thin film formation. The addition of varying concentrations of $FeCl_2$ allows for systematic doping of Fe into the CuO lattice, with Fe concentrations ranging from 0 *wt*.% to 25 *wt*.%. The distance from the spray nozzle to the substrate (25 cm) ensures proper atomization and even distribution of the precursor solution across the substrate. Maintaining a consistent air pressure of 2.5 bar and a solution flow rate of 1 mL/min during spraying ensures uniform film deposition, preventing excess precursor accumulation and promoting the formation of high-quality thin films. The substrate temperature of 350 °C, monitored by a thermocouple, is sufficiently high to promote the pyrolysis of the precursor solution, ensuring the formation of CuO films without thermal degradation. The spray time of 5 min is optimised to allow for adequate film growth while preventing over-saturation of the substrate.
Fig. 1 illustrates the spray pyrolysis process for fabricating Fe-doped CuO thin films:

Table 2.1: *Deposition parameters for $Cu_{1-x}Fe_xO$ thin films using SPT.*

SPT parameters	Value
Precursor solution	0.10 mol ($CuCl_2$, $2H_2O$) dissolved in 90 mL water +10 mL EtOH
Dopant	($FeCl_2$, $2H_2O$) with varying concentrations (0, 10, 15, 20, and 25 *wt*.% Fe)
Distance from spray nozzle to substrate	25 cm
Air pressure	2.5 bar
Substrate	BK7 optical-grade glass
Substrate temperature	350 ◦C (measured using a thermocouple)
Solution flow rate	1 mL/min
Spray time	5 min

2.2.2. Sample characterisation

The study of a material's structural information is essential for understanding its nature and helps correlate the different physical properties of the material. A brief description of experimental characterisation techniques used in this study is as follows:

2.2.2.1. Weight difference method

Film thickness is one of the very important attributes of the films to be determined. The reason is that many properties of the films are dependent on the film thickness, and other parameters, such as mass density, can be derived from the thickness.

Different techniques were employed to estimate the film thickness. The weight difference method is convenient and straightforward, and the thickness *t* is measured using the gravimetric method. This method is performed using a sensitive electronic balance with four-digit sensitivity (10^4 g). The substrates are weighted before and after deposition. From the weight difference and the area of substrate, the thin film thickness (*t*) can be measured, according to the following equation:

$$\mathbf{T = \Delta m / \rho_0 \times S} \qquad (2.1)$$

Where Δm is the weight difference of the substrate. This means that it is the mass of the thin film (g); S is the area of the thin film cm^2, and ρ_0 is the density of material of the thin film (6.51 g/ Cm^3) for copper oxide and (7.874 g/cm^3) for iron, the density of material calculated from:

*Total density (ρ_0) = density of CuO × its percentage in the solution + density of Cu × its percentage in the solution [4].

In this work, the obtained films have a thickness of about 326 nm.

2.2.2.2. X-ray diffraction

X-ray diffraction techniques (XRD)are a family of non-destructive analytical methods that reveal information about the crystallographic structure, chemical composition, and physical properties of materials and thin films [5]. These techniques are based on observing the scattered intensity of an X-ray beam hitting a sample as a function of incident and scattered angle, polarisation and wavelength or energy. From the X-ray diffraction pattern, we can obtain the following information [6]:

- Identification of phases present in the material.
- Study the formation of a particular material system.
- Estimation of unit cell structure, lattice parameters and Miller indices.
- Estimation of the amorphous content.
- Analysis of the average crystalline size from the width of the peak. Large grain size gives rise to sharp peaks, while the peak width increases with decreasing grain/particle size.

- Analysis of structural distortion caused by the strain and thermal distortion

XRD is a crucial technique for determining the crystal structure of nanostructured thin films, which is influenced by the deposition conditions. The basic principle lies in the mechanism of electron (x-ray) diffraction within the crystalline lattice. Since all the atoms in a crystalline solid are regularly arranged with an interatomic spacing of the order of a few angstroms, the crystal can behave as a three-dimensional grating for x-rays. When a monochromatic X-ray beam passes through such a crystalline solid, the X-ray electron gets diffracted as the wavelength of the X-ray is comparable to the interatomic spacing within the solid. In 1912, W.H. Bragg and W.L. Bragg proposed a model that generates the condition for diffraction, considering the reflection of an X-ray beam from atomic planes, as shown in Figure 2.2. It was discovered that the constructive diffraction pattern will occur following Bragg's law condition:

$$2\, d_{hkl}\, sin\theta_{hkl} = n\, \lambda \qquad (2.2)$$

Where n is an integer 1, 2, 3….. (usually n =1), λ is wavelength in angstroms (1.5418 Å for $Cu\ K\alpha$), d_{hkl} is spacing between the planes, the θ is the angle between the incident light and the lattice planes, the 2θ is angle between the incident and scattered beams, the angle 2θ of maximum intensity is called the Bragg angle. All diffraction directions of the lattice will be generated by scanning through a range of 2θ angles on the sample.

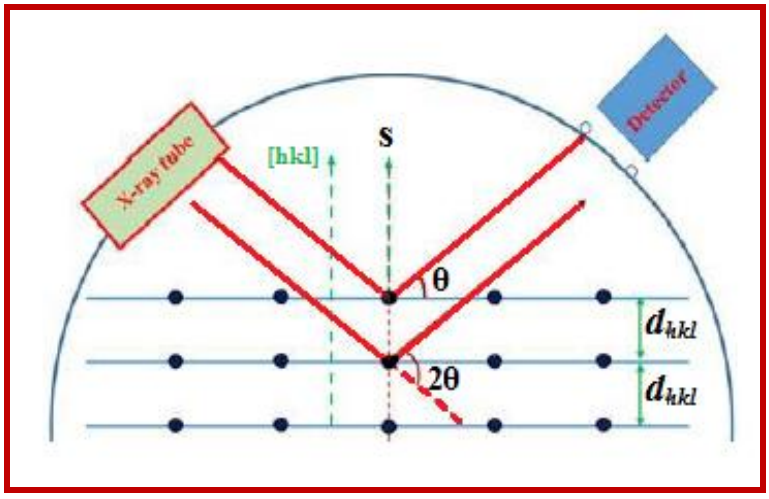

***Figure 2.2**: Schematic of the Bragg diffraction condition [6].*

In this work, the structural properties of the nanostructured films were studied using X-ray Diffraction (XRD), with an X-ray diffractometer (Bruker D8 Advanced) operating in a (θ−2θ) geometry, utilising a Cu Kα source (λ_{Cu} = 1.5418 Å) to analyse the phase formation in

the $Cu_{1-x}Fe_xO$ films. The diffractograms were measured in the 2θ domain of 20-70°, using a 0.02° step size and a 10 s step time.

2.2.2.3. Scanning Electron Microscopy

The morphology of the nanostructured films can be investigated via scanning electron microscopy (SEM). SEM is one of the most widely used tools to characterise the morphology of thin films. This technique is based on the interplay of a beam of electrons with the sample surface (Figure 2.3). This interaction produces the emission of electrons from the sample with different energies due to either elastic or inelastic scattering, or the absorption of photons, which are collected by a detector to produce a distribution map based on the intensities of the signal. Each of the three emitted scattered electrons allows the reproduction of images that provide different information about the sample. For example, images from secondary electrons (inelastic scattering) are suitable for studying topographical features. From a top view, this technique permits the visualisation of the crystalline columns emerging at the sample surface, as well as the different material phases, either crystalline or amorphous, due to the contrast created by secondary electrons. The film thickness can be evaluated from a cross-sectional SEM analysis.

In this work, the morphological and compositional characterisation of the semiconducting thin films is carried out using a scanning electron microscope FEI Quantum 250 SEM operating at 25 kV.

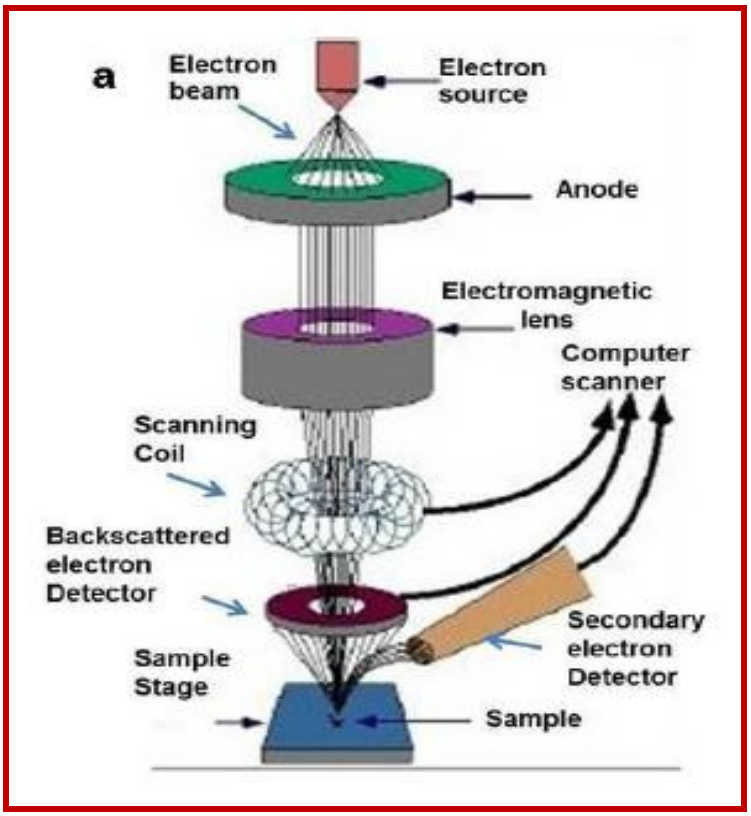

Figure 2.3: *Block Diagram of SEM components [7].*

2.2.2.4. Photoluminescence spectrometry

The photoluminescence (PL) emission was measured at 300 K using a PerkinElmer LS55B luminescence spectrometer and an Xe flash lamp excitation source over 200-900 nm.

Photoluminescence spectroscopy is one of the most popular & non-destructive techniques for investigating the optical properties of the material. The Photoluminescence is a process in which the material absorbs and re-radiates photons. Since the PL measurement does not rely on electrical excitation or detection, sample preparation is minimal, making it attractive for material systems with poor conductivity or undeveloped contact/junction technology [6]. PL spectroscopy system has the following components:

1. A light source (continuous or pulsed laser).
2. Dispersive element for light dispersion (spectral analysis of PL).
3. Sample holder including lens optics for focusing light and collecting the emissions.
4. Optical detector along with appropriate electronics for signal conditioning & readout mechanism.

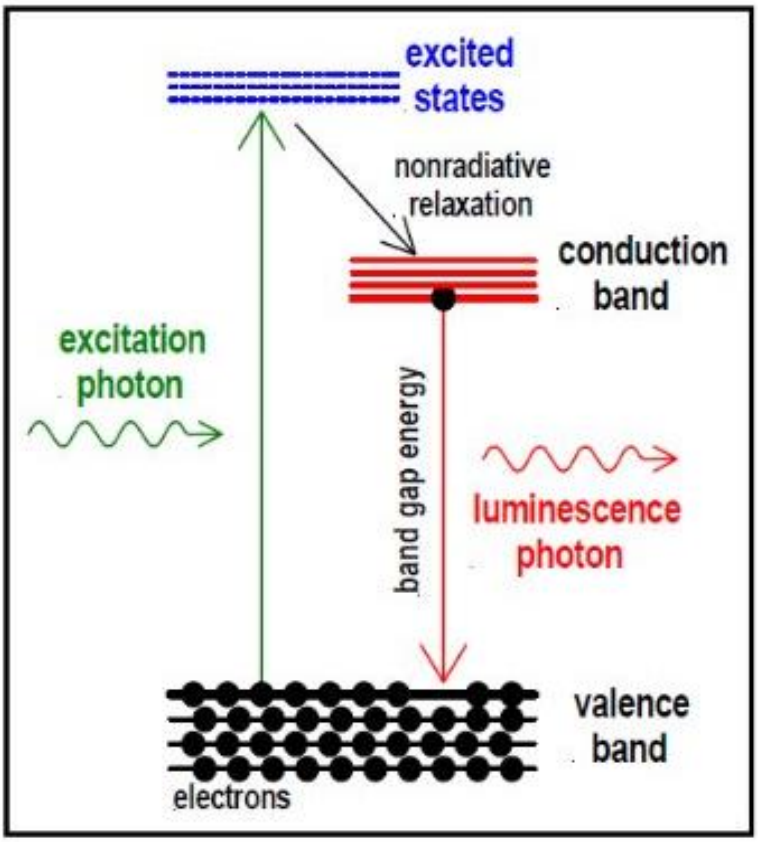

Figure 2.4: *Principle of photoluminescence spectroscopy [1].*

As shown in Figure 2.4, the main principle of PL measurements is that the semiconductor is excited by light photons with higher energy than the band gap of the semiconductor, such as a laser. Then, the incident photons are absorbed, creating electron-hole pairs in the semiconductor. Within a short period, the electron-hole pairs recombine and emit photons from the semiconductor; the energy of the emitted photons reflects the energy of the carriers in the semiconductor. Finally, the emitted luminescence (light) and intensity are collected and recorded to generate a PL spectrum. These emitted photoluminescence and intensity are direct measurements of semiconductor properties, such as bandgap, impurity levels, defect detection and recombination mechanisms [8].

2.2.2.5. UV-visible spectrometer

UV-visible spectroscopy is widely used in various fields, including chemistry, biochemistry, environmental science, and materials science, for the qualitative and quantitative analysis of the optical properties of substances. Instrumentation for measuring the absorption of UV or visible radiation can be summarised as (a) source (for generation of UV-visible radiations), (b) wavelength selector (monochromator), (c) sample container, (d)

detector, and (e) signal processor and screen [54]. A pictorial representation of the UV-Vis Spectrophotometer is exhibited (see Figure 2.5).

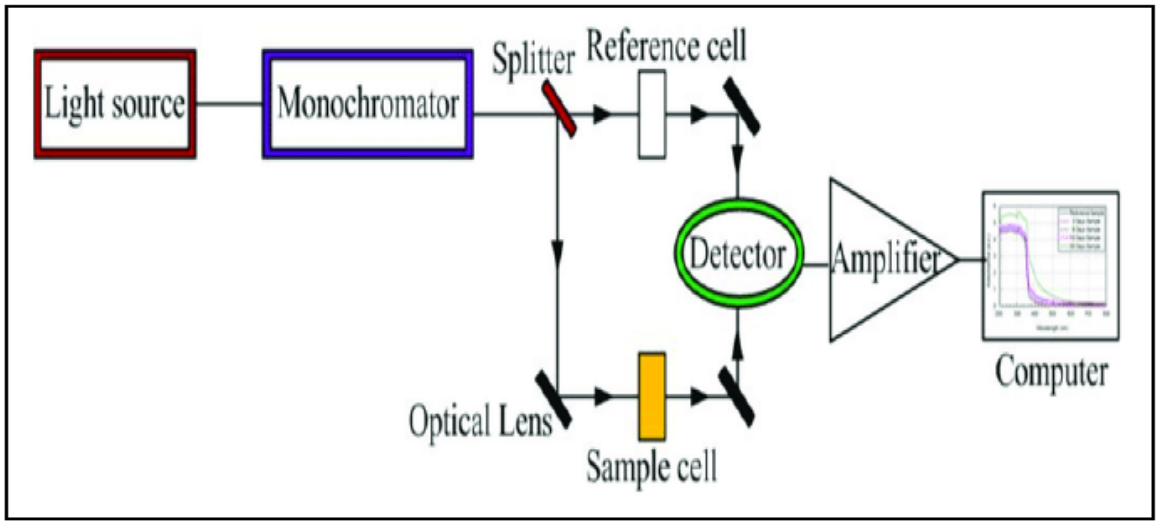

Figure 2.5: *A pictorial representation of UV-Vis Spectroscopy [9].*

The optical study concerns transmission, absorption, reflection, refraction, polarisation, interference, and other properties. From these properties, it is possible to calculate the optical constants, such as the absorption coefficient (α), direct and indirect band gaps, refractive index (n), extinction coefficient (k), optical conductivity, and the real and imaginary parts of the dielectric constant, among others.

UV-visible transmission spectra have been recorded using a UV-visible spectrometer (SPECTROVIO C5210- C5220 in the wavelength range of 200-900 nm at room temperature. The absorbance/transmittance transmission spectra have been recorded for both pure CuO and CuO: Fe thin films.

2.2.2.6. Vibrating sample magnetometer

The Vibrating Sample Magnetometer (VSM) is a tool that provides information about the magnetism of samples, allowing for operation at low temperatures and under variable external magnetic fields. A schematic representation of a VSM is shown in Figure 2.6. A sample is placed between two electromagnets, and it undergoes vibration in a sinusoidal manner. The change in magnetic flux is induced by the sinusoidal motion of the sample, which in turn causes a voltage in the pickup coil. The magnitude of the VSM signal is determined by the magnetic moment of the sample. In other words, the variation in magnetic

flux density provides information about the magnetisation behaviour of the sample under investigation.

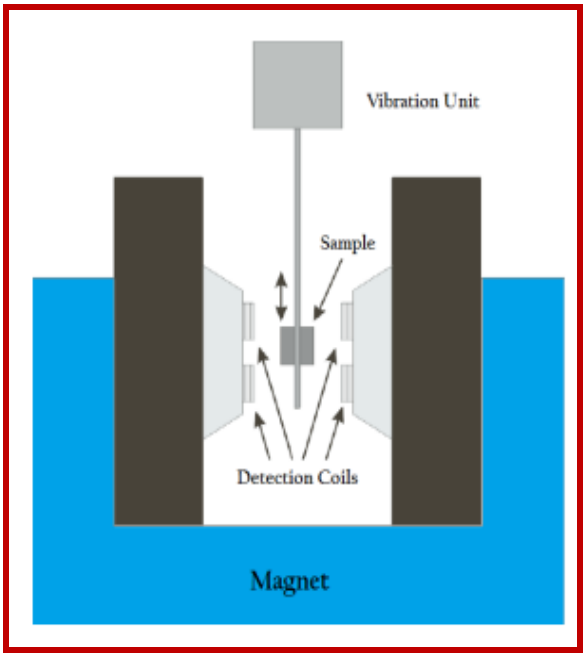

***Figure 2.6**: Schematic demonstration of a VSM chamber.*

The magnetic properties of the investigated samples were measured at room temperature using a vibrating sample magnetometer (VSM) (PMC MicroMag 3900 Series; LakeShore Cryotronics) with a parallel magnetic field of ±10 kOe to the film plane, approximately 5 mm × 5 mm × 5 mm. From the obtained hysteresis loops, the saturation magnetisation (Ms) and coercivity (H_C) were determined.

2.2.2.7. Electrical measurements

The most widely used technique for measuring electrical resistivity is the four-point probe method. It consists of four metal tips, linearly arranged with the same separation from each other. An electric current is applied to the outer two probes, while the potential difference is measured in the inner two probes (Figure 2.7).

From these measurements, the sheet resistance (R_{sh}) of the film can be calculated using the following equation. Sheet resistance is defined as the ratio of resistivity (ρ) to film thickness (t).

$$R_{sh} = \rho / t \qquad (2.3)$$

An extra issue related to the measurement of carrier concentration and carrier mobility appears in semiconductor characterisation. The Van der Paw technique [10] provides a

solution to obtain these parameters. This method is based on two independent measurements, i.e. resistivity and Hall coefficient. The characteristic resistances are first obtained by applying a current between two adjacent contacts. In comparison, the potential difference is measured in the other two remaining contacts, all of which are located in the periphery of a sample with an arbitrary shape. These results are then incorporated into an expression developed by Van der Pauw, where d is the film thickness and f is a correction factor that depends on the ratio of the characteristic resistances R_A and R_B.

$$\rho = \frac{\pi d}{\ln 2}\left(\frac{R_A + R_B}{2}\right) f \tag{2.4}$$

The Hall effect consists of the creation of a voltage when an electric current (I) is applied between opposite contacts of a semiconductor that is under the effect of a magnetic field perpendicular to the plane of the sample (*B*). This potential difference is created by the migration of charge carriers, either electrons or holes, to the edge of the sample induced by the magnetic force. The sign of this voltage is determined by the type of major carriers dominating the electronic transport. This Hall voltage (V_H) is used to obtain the Hall coefficient (R_{HS}) and the carrier concentration (N_S) through the following equation.

$$R_{HS} = V_H / IB = r / qN_s \tag{2.5}$$

Where r is the scattering factor, and q is the elementary charge. The carrier Hall mobility (μ_H) is obtained by combining the Hall coefficient with the resistivity previously calculated

$$\mu_H = R_{HS} / \rho \tag{2.6}$$

Using a four-point method, the resistivity (ρ), mobility (μ), p/n type, and carrier concentration of $Cu_{1-x}Fe_xO$ films were determined by utilising a HMS-3000 Hall System at 300 K.

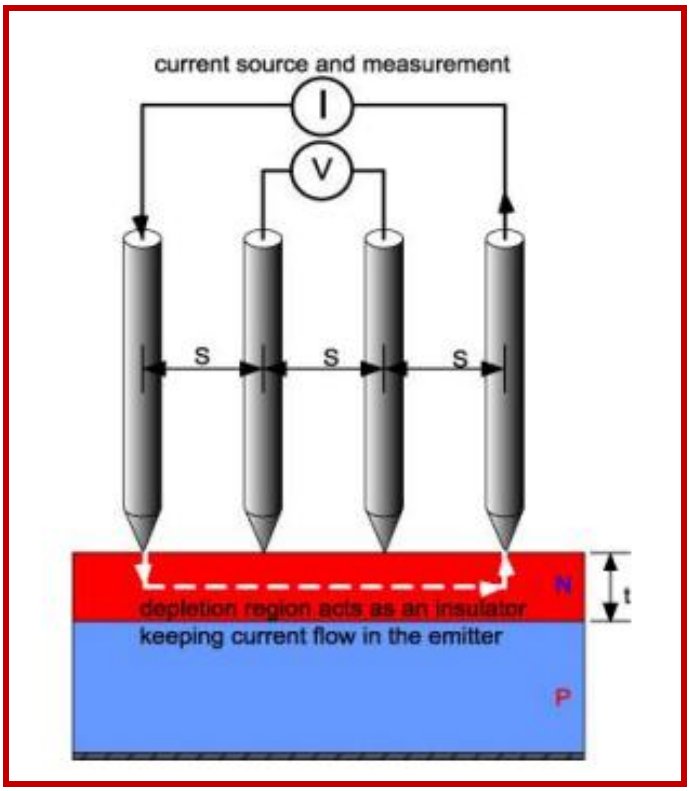

***Figure 2.7**: Four point probe method [7].*

References

[1] R.D. Prasad, S. B. Teli, R. S. Prasad, ES Mater. Manuf., 25 (2024)1198.
[2] J. E. Bishop, T. J. Routledge, D. G. Lidzey, The Journal of Physical Chemistry Letters, 9, 1977 (2018).
[3] R. D. Prasad, S. B. Teli, R. S. Prasad, R. B. Prasad, S.R. Prasad, P. Sinha, A. Sinha, P. Sinha, M. Saxena, R. R.. Prasad, R. S. Pande, N. Charmode, K. G. Deshmukh,P. D. Sarvalkar, U. D. Kadam, C. Chiplunkar, N. Prasad, M.V. Padvi and
[4] Z. Guo, ES Mater. Manuf., 25 (2024) 1198.
[5] A. Kumar, synthesis, characterization and application of bare and zinc doped nickel oxide nanoparticles, master of philosophy in chemistry, Shoolini University, (2013).
[6] B. D. Cullity, "Elements of X-ray Diffraction", Addison Wesley, Massachusetts (1956).
[7] H.S. Kaushik, Thesis, J.C. Bose University of Science & Technology, YMCA, Faridabad (2011).
[8] S. Ghosh, G. G. Khan and K. Mandal, EPJ Web of Conferences 40, 03001 (2013)].
[9] P. Jagadeesh, S. M. Rangappa, S. Siengchin, Advanced Industrial and Engineering Polymer Research, 7 (2023) 122.
[10] L. J. van der Pauw, In Semiconductor Devices: Pioneering Papers, (WORLD SCIENTIFIC: (1991) pp. 174-182.

Chapter 3
Results & Discussion

Chapter 3

Results & Discussion

This chapter examines the impact of Fe addition on the structural, optical, magnetic, and electrical properties of CuO thin films. It presents and analyses the experimental findings obtained through various characterisation techniques conducted on nanostructured $Cu_{1-x}Fe_xO$ films.

3.1. Structural analysis

X-ray diffraction is a non-destructive technique that provides various information on the crystal structure, phase, crystal orientation, and other properties of materials. It is the primary method for crystallographic characterisation of bulk, nano, and thin film materials. This is achieved by irradiating a sample of the material with incident X-rays and then measuring the intensities and scattering angles of the X-rays scattered by the material.

The XRD patterns of pure and doped CuO with different Fe concentrations are shown in Figure 3.1. A closer examination of this figure revealed various reflections peaks at 2θ = 35.71°, 38.21°, 44.47°, 54.44°, 57.40°, 60.91°, 65.85° and 67.13° assigned respectively to the diffraction planes (002), (111), (-202), (020), (202), (-113), (-311) and (220) of the monoclinic CuO phase (PDF4+ICDD file No. 04–004–4916, space group C2/c (No. 15). For x = 0.25, the appearance of new peaks are related to the formation of a secondary phase. The new diffraction peaks, situated at 2θ angles of 32.12°, 34.33°, and 48.32°, are attributed to the 104, 110, and 024 crystal planes corresponding to the rhombohedral (hexagonal) α-Fe2O3 phase, also known as hematite (JCPDS file No. 013-0458), with the R-3c space group (No. 167). The intensity of the (002) and (111) main diffraction peaks of the CuO phase shifts slightly towards higher 2θ angles with increasing Fe content, indicating a contraction in the crystal lattice.

The form and distribution of Fe ions inside the CuO matrix depend essentially on the synthesis atmosphere. Therefore, incorporating Fe within the CuO crystal structure does not guarantee that Fe^{2+} will certainly substitute Cu^{2+} ions. Thus, Fe would manifest in different ways: (i) substitutional solution as Fe^{3+}, (ii) substitutional solution as Fe^{2+}, (iii) spinel ABO_3 phase, or (iv) metallic Fe precipitates. Consequently, the formation of nano-structured α-Fe_2O_3 phase for x =0.25 indicates that the Fe solubility limit into the CuO crystal lattice is reached for x = 0.20. Consequently, the presence of more Fe atoms in the starting solution leads to the precipitation of α-Fe_2O_3. It is established that under ambient conditions, α-Fe_2O_3 is the more stable polymorph of iron (III) oxide with a significant negative heat of mixing of about −826 kJ/mol.

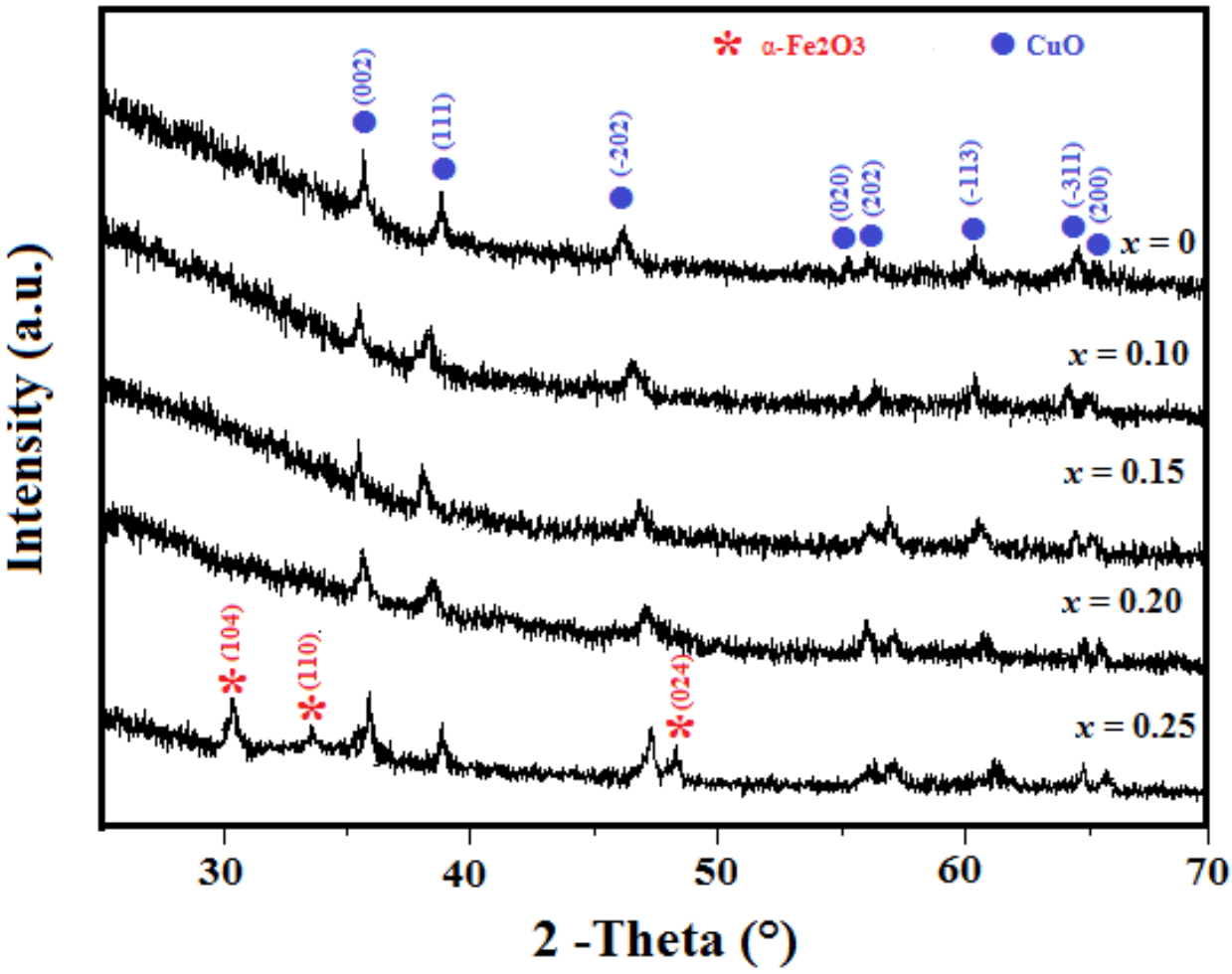

Figure 3.1: *Evolution of the XRD patterns of $Cu_{1-x}Fe_xO$ thin films as a function of Fe-doping.*

Fe is reported to be soluble up to 15% in the CuO synthesised by the wet chemical technique [1]. Besides, the decrease in the unit volume as the Fe content increases was

attributed to uniform Fe doping at the Cu site in CuO [1]. However, in the Fe-doped CuO obtained using the urea nitrate combustion technique, the solubility limit of Fe was 20% because the secondary α-Fe_2O_3 was observed for 25 and 30% Fe [2]. The α-Fe_2O_3 secondary phase was formed for 4 and 8 at. % Fe in the Fe-doped CuO nanostructures produced by hydrothermal [3]. The X-ray diffractogram of the sprayed 10% Fe-doped CuO thin film on glass at 500°C revealed the coexistence of monoclinic CuO and cubic $CuFe_2O_4$ phases [4]. The spin coating process was utilised to deposit *x*Fe-doped CuO films (x = 3−9 wt.%) onto glass substrates. The thin films showed a monoclinic phase, with decreasing crystallite size as the Fe-doping content increased. The bandgap diminished from 3.48 to 2.79 eV for pure CuO and 9 wt.% Fe, respectively [5].

The improvement in the solubility limit of Fe in the CuO matrix differs from that reported earlier for the Fe-doped CuO prepared by spray pyrolysis with a smaller content of Fe-doping [1, 3]. Hence, Fe-doped CuO (with 0-5 wt. % Fe) thin films, deposited at 450°C by a nebuliser-assisted spray pyrolysis procedure, exhibited a monoclinic CuO structure with 28 nm crystallite size [6]. The secondary α-Fe_2O_3 phase was observed in the Fe-doped CuO prepared by the urea nitrate combustion technique for Fe contents of 25% and 30% [2]. A lower solubility limit was observed in CuFeO prepared by the sol-gel technique (~12.5%) [7]. The discrepancies may be related to several parameters, such as the preparation method, starting products, solution preparation, and pH, among others. One also notes that the Cu^{2+} (0.73 Å) ionic radius is higher than that of Fe^{3+} (0.64 Å) but close to that of Fe^{2+} (0.77 Å). Consequently, higher Fe incorporation into the CuO lattice and its substitution for Cu may engender crystal defects, strains, and distortions for a substitutional solution such as Fe^{3+}.

3.1.1. Rietveld Refinement Analysis of XRD Results

Qualitative and quantitative analysis of the diffraction patterns of the prepared samples was conducted using the Maud software, based on the Rietveld method [4]. The refinement was carried out by taking both structural (atomic coordinates, occupancies, lattice parameters, thermal parameters) and microstructural (crystallite size and root-mean-square strain (r.m.s.) parameters as free parameters, The background was fitted using third degree polynomial function, meanwhile the peak shape profile is fitted using a linear combination of Gaussian (crystallite size) and Lorentzian (microstrain) functions, which is called as Pseudo-Voigt (pV) function [5]. Least squares Marquardt procedures were utilised for reducing the difference

between the experimental and calculated XRD patterns using the reliability parameters, R_{wp} (weighted residual error) and R_B (Bragg factor) defined as:

$$R_{wp} = \left[\frac{\sum_i w_i (I_0 - I_c)^2}{\sum_i w_i I_0^2} \right]^{1/2} \tag{3.11}$$

and

$$R_B = 100 \frac{\sum |I_0 - I_C|}{\sum I_0} \tag{3.2}$$

The quality of the Rietveld refinement is approved through the goodness parameter given by the ratio of R-weighted (R_{wp}) to the R-expected (R_{exp}) patterns ($\chi^2 = R_{wp}/R_{exp}$) [8], where:

$$R_{\exp} = \left[\frac{N - P}{\sum_i w_i I_0^2} \right]^{1/2} \tag{3.3}$$

wi=1/Io; Io and *I* are the experimental and calculated intensities, *N is* the number of experimental points, and *P* is the number of fitting parameters. The best refinement is reached when the value of χ^2 is close to 1.

The typical refinement plots of pure and Fe-doped CuO compositions via the MAUD program [9] are shown in Figure 3.2. In this Figure, the calculated patterns are shown in the same field as a solid line curve. The difference between the observed and calculated intensities is shown in the middle field. All refinements were performed using the following considerations:

(i) In the monoclinic CuO structure with Z=4, the Cu^{2+} ions occupy the symmetry site 4c (1/4, 1/4, 0), and the oxygen ions are located at the fourfold set 4e (0,0.4184, 1/4). The lattice parameters are *a*=4.6837 Å, *b*=3.4226 Å, and *c*=5.1288 Å, and β= 99.54°.

(ii) In the rhombohedral α-Fe_2O_3, Fe and O atoms are located at 12c (0, 0, 0.3557) and 18e (0.3216, 0, 1/4), respectively. The lattice parameters are *a* =*b* =5.037 Å and *c* =13.771 Å.

The revealed reliability factors of the best Rietveld refinement of the XRD patterns are listed in Table 3.1.

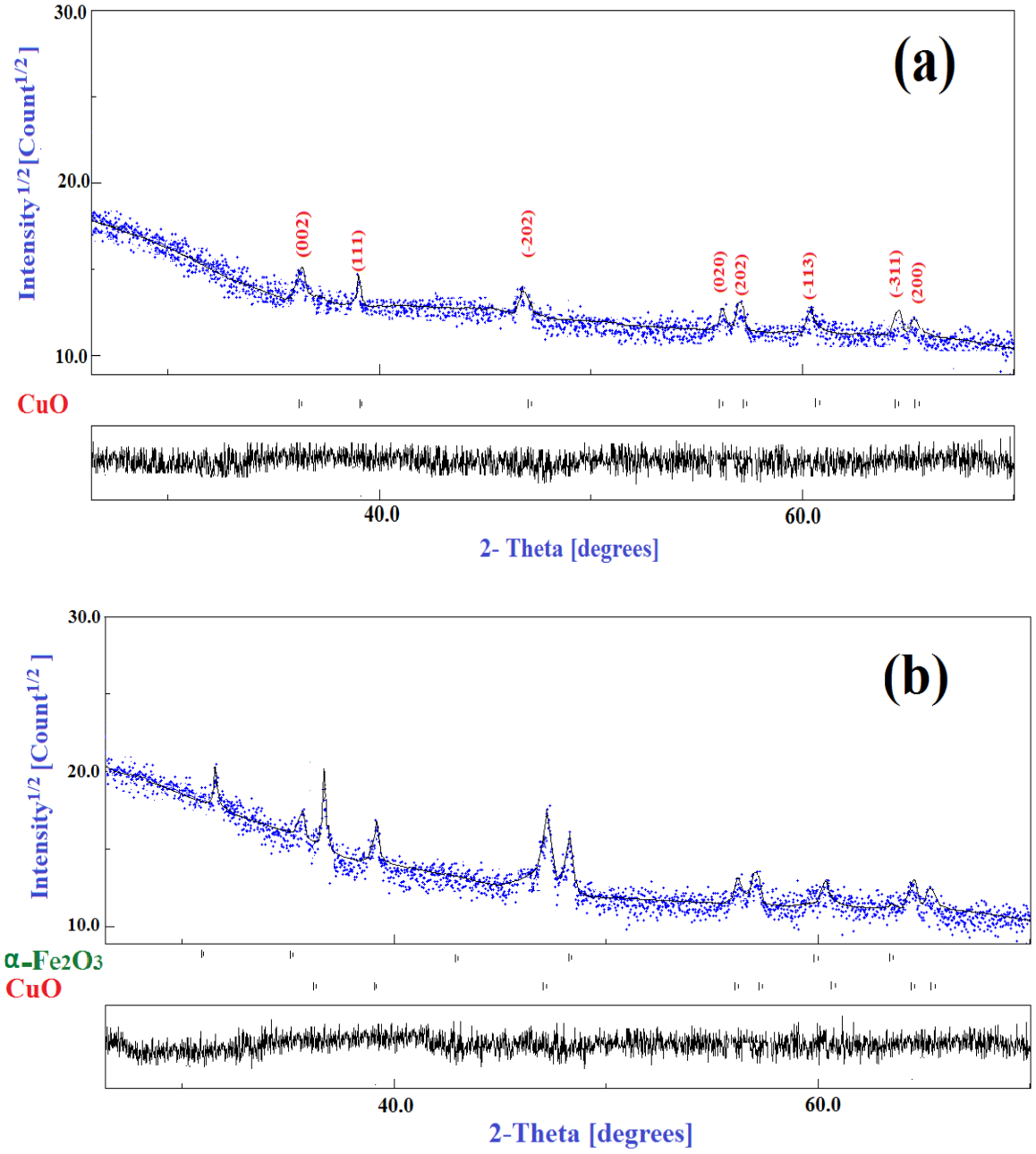

Figure 3.2: *Typical Rietveld refinements of the XRD patterns of pure CuO (a) and (b) $Cu_{0.75}Fe_{0.25}O$ (b) thin films.*

***Table 3.1**: Reliability factors estimated from Rietveld refinement of XRD patterns*

	0.00	0.10	0.15	0.20	0.25
Weighted profile factor (Rwp)	4.419	5.149	3.452	4.315	5.934
Bragg R-factor (RBragg)	2.878	3.014	2.356	2.473	2.055
Expected R-factor (Rexp)	4.047	4.569	3.116	3.455	5.147
Chi squared (χ^2)	1.092	1.127	1.108	1.249	1.153

3.1.2. Structural parameters

The structural parameters of the pure as well as doped CuO samples, including the cell length ($a \neq b \neq c$) and the cell angle ($\alpha = \gamma = 90^\circ \neq \beta$) are extracted from the Rietveld refinements and listed in Table 2. There are slight changes in the structural parameters with the incorporation of the Fe-dopants into the CuO lattice. These barely detectable changes are due to the dissimilarity of the ionic radii of the dopant ions (Fe^{2+} / Fe^{3+}) as compared to the host Cu^{2+} ions. This further confirms the incorporation of Fe atoms in the CuO lattice, without changing its structure.

The obtained lattice constants are smaller than those of the JCPDS file of monoclinic CuO structure (a_0=4.703 Å, b_0=3.426 Å, c_0=5.148 Å, and V_0=81.84 Å^3. The related variation in the lattice parameters to a_0, b_0, and c_0 can be estimated using the following relations: $\Delta a\,(\%) = \frac{a-a_0}{a_0}$, $\Delta b\,(\%) = \frac{b-b_0}{b_0}$, and $\Delta c\,(\%) = \frac{c-c_0}{c_0}$. The crystal structure of the Fe-doped CuO exhibits contractions ranging from –0.429 to –0.472% for Δa, –0.119 to –0.18% for Δb, and –0.456 to –0.592 % for Δc (Table 3.2).

The variation in the lattice parameters of $Cu_{1-x}Fe_xO$ films compared to pure CuO indicates that the Fe dopant has been incorporated into the CuO host lattice. Thus, the lattice parameters and cell volume reduction might be due to substituting Fe^{3+} (0.64 Å) ions for Cu^{2+} (0.73 Å) ones. However, Fe^{3+} being further positive than Cu^{2+} will raise the lattice's O affinity, reduce the oxygen vacancies, and provide the possibility of O-interstitial points. Hence, for each of the two Fe^{3+} substitutions, an interstitial O atom may be essential, leading to a rise in the probability of a structural breakdown. Additionally, Cu^{2+} ions can be substituted by a proportion of Fe^{+2} and Fe^{3+} ions, creating a vacancy in the CuO monoclinic lattice without disturbing the crystal structure [10, 11]. The lattice parameters of $Cu_{1-x}Fe_xO$ thin films are analogous to those of the literature [12-14]. For the pure CuO film prepared by

the coprecipitation method, the cell parameters were: a = 4.6836 Å, b = 3.4227 Å, c = 5.1278 Å, and V = 81.06 Å^3 [15]. A lattice constant of a = 4.699 Å, b = 3.444 Å, c = 5.091 Å, and V=81.32 Å^3 were reported for Fe-doped CuO nanocrystals produced by the solid-state reaction technique [16]. The divergences between our results and the literature might be correlated with the preparation conditions.

***Table 3.2**: Structural parameters of nanostructured $Cu_{1-x}Fe_xO$ thin films.*

x	**0.00**	**0.10**	**0.15**	**0.20**	**0.25**
***a* (Å)**	4.6828	4.6822	4.6808	4.6811	4.6812
***b* (Å)**	3.4203	3.4219	3.4205	3.4198	3.4201
***c* (Å)**	5.1245	5.1214	5.1195	5.1187	5.1175
***β* (°)**	99.83	99.76	99.58	99.63	99.71
Δ*a* (%)	-0.429	-0.442	-0.472	-0.465	-0.463
Δ*b* (%)	-0.166	-0.119	-0.553	-0.180	-0.172
Δ*c* (%)	-0.456	-0.516	-0.160	-0.569	-0.592

The lattice geometry formula was used to determine the primary monoclinic unit cell volumes (V = *abc* sin*β)*. The corresponding CuO unit cell volumes are shown in Figure 3.3 as a function of Fe content. The cell volume is found to decrease slightly from 82.07 to 81.93 Å^3. The lattice expansion or contraction depends on the ionic radii of the foreign and host atom. Thus, the substitution of Cu^{2+} having a larger ionic radii with relatively the smaller one (Fe^{2+}/Fe^{3+}) results in the lattice contraction [17,18].

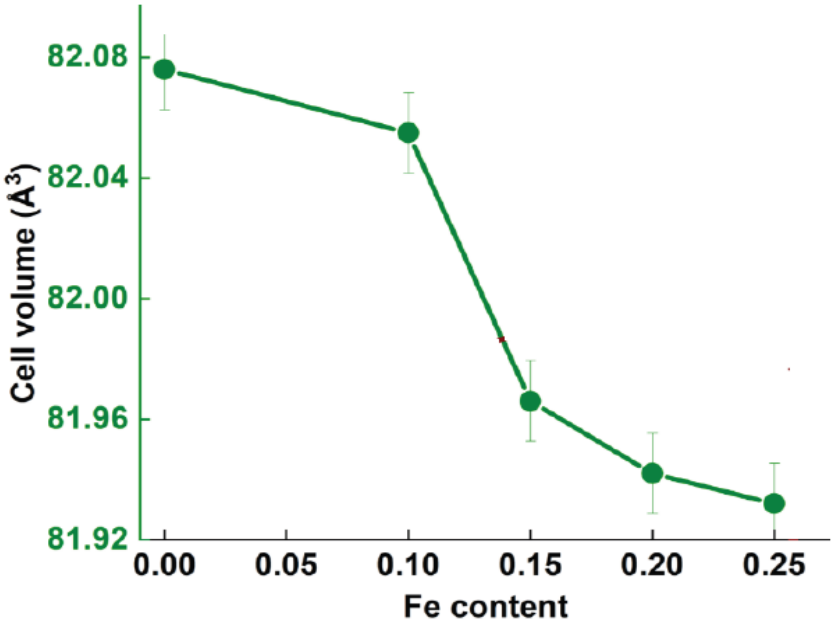

***Figure 3.3:** Cell volume variations versus Fe content.*

3.1.3. Crystallite size

In addition to the Rietveld method (RM), the Debye–Scherrer method (DSM) was identified and applied to the XRD patterns of the samples to determine the crystallite size and microstrain. The DSM method is a straightforward and widely used approach to determine the average crystallite size. The DSM's relation between average crystallite size (<*L*>) and full width at half maximum (FWHM, β) is given to ascertain these contributions:

$$L = K\lambda / \beta\cos\theta \tag{3.4}$$

Where 2θ is Bragg's diffraction angle, K is a constant which is equal to 0.9, and λ is the wavelength used. It is worth mentioning that the FWHM was corrected by taking into account the instrumental broadening (*βins*), following the relation:

$$\beta^2 = \beta^2_{measured} - \beta^2_{ins} \tag{3.5}$$

From equation (4), the size can be obtained from the slope of the DSM plot, by considering the variations of cos θ as dependent variables on the values of $1/\beta$.

The generated microstrain (ε) from the lattice distortion can be estimated from the Stock–Wilson (SW) formula [19]:

$$\varepsilon = \beta cos\theta / 4 = K\lambda / 4\ \mathrm{L}\ sin\theta \tag{3.6}$$

The values of the crystallite size obtained using the Debye–Scherrer formula are very close to those obtained by Profile fitting by Rietveld analysis (Table 3.3). This difference may be due to the fact that the internal strain effect is not considered in the Scherrer model, which only fits the peak shape with a Gaussian distribution. However, in the Profile fitting Rietveld analysis, the peak shape profile is fitted using a linear combination of Gaussian (crystallite size) and Lorentzian (microstrain) functions, which are collectively referred to as Voigt or pseudo-Voigt functions [2]. The average crystallite size, <*L*>, of the CuO phase decreases as the Fe content increases, reaching 32.74 nm for the $Cu_{0.75}Fe_{0.25}O$ sample. Simultaneously, the r.m.s. strains reach a maximum value of 0.14% for x=0.15 and remain in the range of 0.09-0.10 for x=0, 0.1, 0.2, and 0.25. The impacts of doping on the microstructure were usually detected in metal oxides [20]. In the Ag-doped ZnO, the defect formation inhibited the crystallite growth [21]. Additionally, the formation of fine precipitates during doping can act as pinning centres at the grain boundary, where the crystallite growth is prevented. [22].

3.1.4. Dislocation density

Among the linear crystal defects, dislocations strongly influence numerous properties. The dislocation density, described as the length of dislocation lines per unit volume of the crystal, can be determined by equation (3.7). It is the measure of the number of dislocations present in the content of the material. Dislocations are irregularities or crystallographic defects in a crystal that arise from the lattice mismatch with another part of that crystal. This can be determined by the following formula [23]:

$$\rho_D = 1 / \langle L \rangle^2 \qquad (3.7)$$

The dislocation density increases with increasing Fe content (Table 3.3). Because the generated dislocation density in the Fe-doped CuO films is about ~10^{15} m^{-2}, the dislocations might be a mixture of screw (~ 10^{13} m^{-2}) and edge (~ 10^{16} m^{-2}). The higher number of dislocations allows solid solution formation by accelerating atomic diffusion. The obtained values are comparable to those reported for Fe-doped CuO thin films [10,24, 25].

Table 3.3: *Microstructural parameters deduced from Rietveld refinement.*

Fe content (*x*)	**<L> (nm)**		**Strain (%)**		**ρ_D (x $10^{15}m^{-2}$)**
	RM	**DSM**	**RM**	**SW**	
0	45.74	76.14	0.102	0.178	0.477
0.10	41.01	63.45	0.091	0.204	0.594
0.15	39.29	52.98	0.143	0.252	0.647
0.20	36.75	50.73	0.103	0.311	0.740
0.25	32.74	45.88	0.099	0.417	0.932

3.2. SEM observation

A scanning electron microscope is a type of electron microscope that produces images of a sample by scanning it with a focused beam of electrons. The electrons interact with atoms in the sample, producing various signals that can be detected and that contain information about the sample's surface topography and composition.

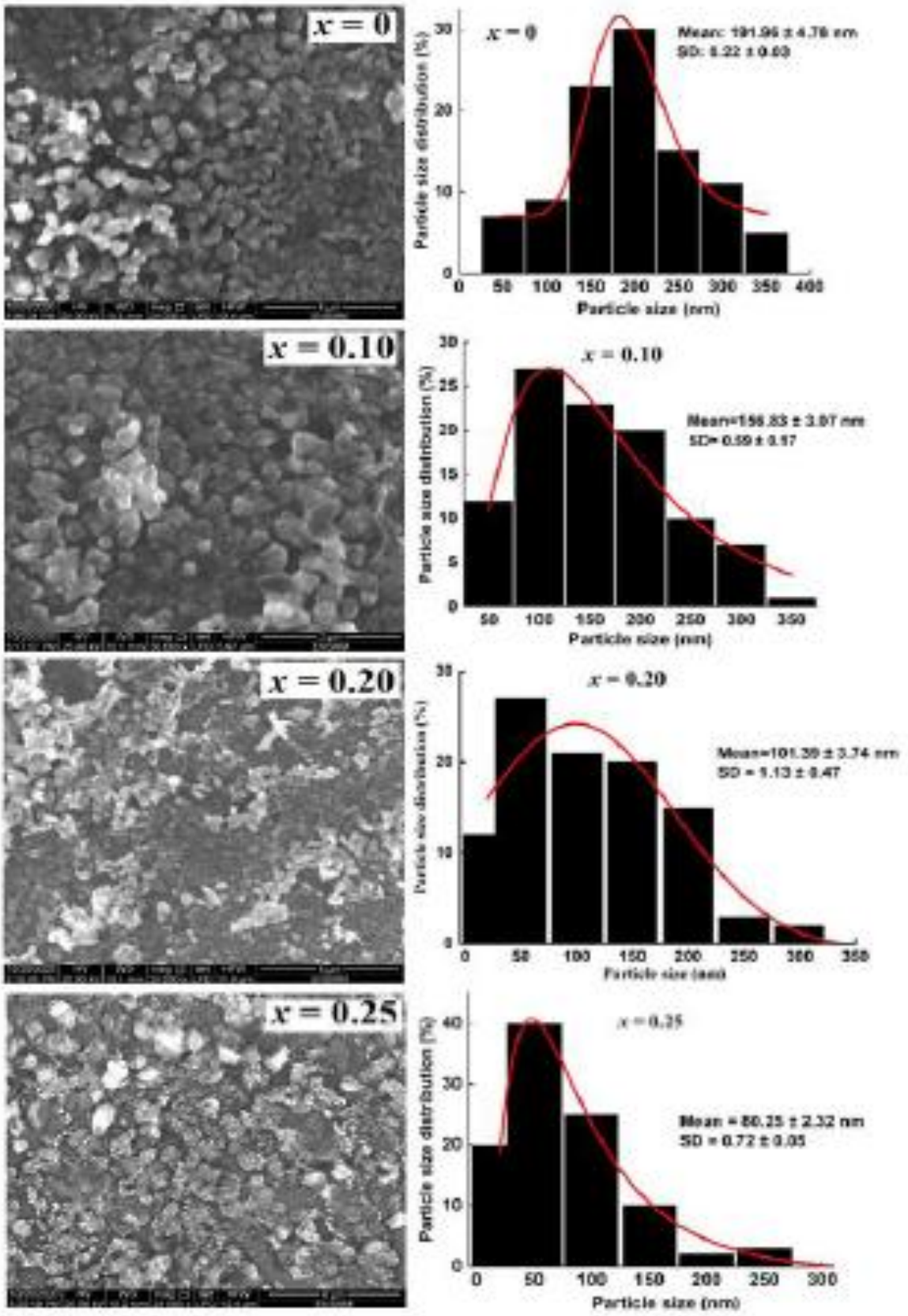

Figure 3.4: *SEM images and particle size distribution of $Cu_{1-x}FexO$ thin films.*

Figure 3.4 illustrates the surface morphologies of $Cu_{1-x}Fe_xO$ thin films. The SEM images of undoped and Fe-doped CuO films with x = 0.10 showed nearly homogeneous cubic-shaped particles with different particle size distributions. As can be seen, Fe-doping did not induce a significant change in the shape of CuO. For x = 0.25, the surface morphology shows the existence of finer and a few bigger particles with irregular shapes in addition to aggregation or overlapping of smaller particles. The difference in the surface morphology of the $Cu_{0.75}Fe_{0.25}O$ compared to the other samples is consistent with the XRD results, which disclose the formation of α-Fe_2O_3 precipitates. Different morphologies were observed for the CuO nanostructures fabricated by chemical precipitation methods using various synthesis conditions (starting materials, temperature, pH, additives, etc.). The morphologies consisted of nanowires, flower-shaped, spindle-like and plate-like, oval nanosheets, nanotubes, nanoribbons and nanorings [1, 21, 22,26-28].

The particle size distribution was analysed using the ImageJ software and well-fitted with a log-normal function, as displayed in Figure 3.4. The average particle size decreases from 191.96 nm for undoped CuO to about 80.25 nm for $Cu_{0.75}Fe_{0.25}O$ (Figure 3.5). For pure CuO, 68% of the particle size ranges between 150 and 250 nm, while 85% of particles are less than 150 nm in size for $Cu_{0.75}Fe_{0.25}O$ film. The particle size fine-tuning rises with increasing Fe content, as confirmed by the left-skewed distribution. The geometrical standard deviation (SD) increases to a maximum value for x=0.2, then decreases slightly.

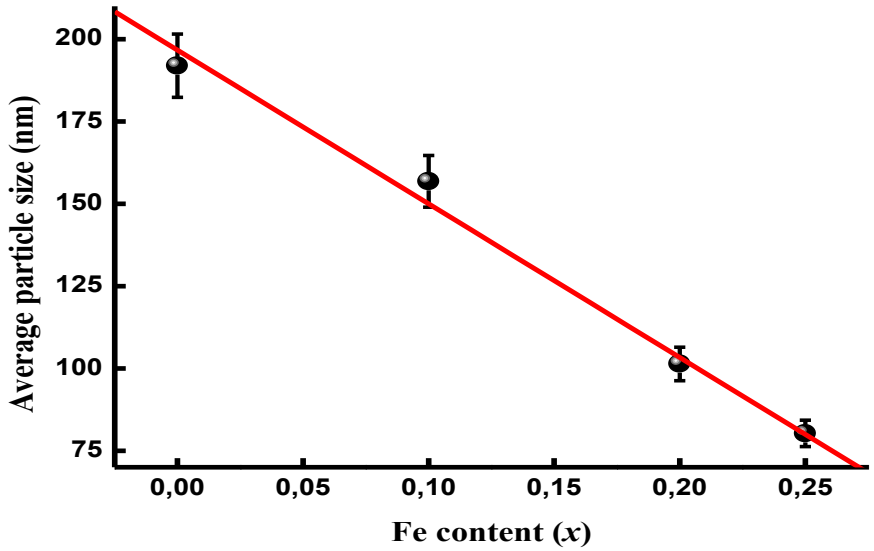

Figure 3.5: *Evolution of the average particle size versus Fe content.*

Particle size refinement with the Fe concentration may be ascribed to the induced disorder due to the discrepancy in the ionic radius of $Fe^{2+}$and Fe^{3+} ions related to that of Cu^{2+} ions [10, 21, 22]. Additionally, the dissimilarity in Pauling electronegativity can affect the growth rate of particles. Pauling electronegativity is a virtually constant atomic property, even for different oxidation states of any element. Thus, the electronegativity of iron, as 1.8 (Fe^{2+}) or 1.9 (Fe^{3+}), is slightly lower than that of copper, as 2.0 (Cu^{2+}). This divergence evidences the decrease in the growth rate of Fe-doped CuO nanoparticles [29].

3.3. Photoluminescence spectroscopy

Photoluminescence spectroscopy is the method used to characterise the various properties of a material, such as purity, crystalline quality and the minority carrier lifetime of semiconductors. PL is one form of luminescence (light emission) after the absorption of photons (electromagnetic radiation). In a typical PL experiment, a semiconductor is excited with a light source that provides photons with energy larger than the band gap energy. Once the photons are absorbed, electrons and holes are formed in the conduction and valence bands, respectively. The excitations then undergo energy and momentum relaxation towards the band gap minimum. Finally, the electrons recombine with holes, emitting photons. In a defect-free semiconductor, the major luminescence comes from the near band edge emission (NBE). If there are various types of defects, corresponding defect bands will be created between the conduction band and valence band, which may also create conditions for electron transitions and light emission, in addition to the NBE emission. Through theoretical calculations and experimental analysis, it is possible to determine the defect state from which a specific emission originates [30].

In nanostructured DMOs, the photoluminescence originates from defects appearing to be broader than the core-related luminescence [31]. Figure 3.6 displays the PL spectra of a nano-structured pure CuO film at room temperature. The three main emission peaks are observed at 395 nm, 617 nm and 758 nm. The corresponding energy levels are 3.14 eV, 2.01 eV and 1.63 eV, respectively. The PL peak at ~395 nm is related to the band-edge emission of CuO nanostructures. PL band at the red region (617 nm) is often associated with deep-level emissions related to native point defects, specifically interstitial copper (Cu_i) and oxygen vacancies (V_o). These defects create energy levels within the band gap, facilitating transitions that result in the emission of orange-red light [32]. The peak at 758 nm may be attributed to electron-hole recombination at the oxygen vacancy.

Three emissions were observed at 682, 752 and 822 nm for CuO nanoparticles synthesised by the precipitation approach [33]. The authors reported that the Peak emission at 682 nm corresponds to near-band-edge emission [34]. Emission at 752 nm was attributed to electron-hole recombination at an oxygen vacancy, and emission at 822 nm was due to the recombination of bound excitons at a single-charged oxygen vacancy [35]. Three main peak emissions around 505 nm (2.46 eV), 547 nm (2.27 eV), 630 nm (1.97 eV), and three shoulder peaks around 520 nm (2.38 eV), 590 nm (2.10 eV), and 650 nm (1.91 eV) were detected in the recorded PL of all spray-deposited CuO thin films with deposition temperature varying from 450 to 550°C [36].

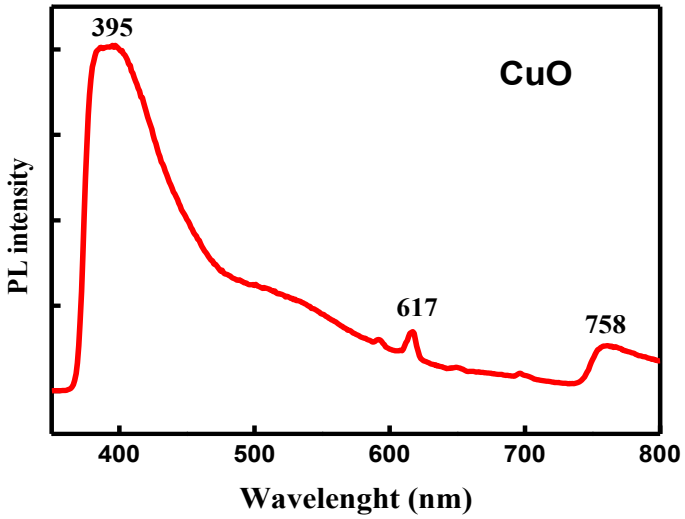

Figure 3.6: *PL spectrum of the deposited pure CuO thin film.*

In nanostructured $Cu_{1-x}Fe_xO$ films with $x > 0$, the addition of Fe to CuO is observed to increase these emission intensities compared to pure CuO nanoparticles (Figure 3.7). This may arise from defects such as a single ionised oxygen vacancy [37]. The emission intensity of TM-doped CuO nanoparticles increased with increasing electron-hole recombination in the valence band (VB) [38]. Additionally, with increasing Fe content, the PL spectra reveal more peaks than those of undoped CuO. Such peaks can be associated with the precipitation of the α-Fe_2O_3 phase, single-ionised oxygen vacancies, and several structural defects in both pure and Fe-doped CuO nanostructures [39]. The observed emission peaks at 434 nm, 537 nm, and 649 nm can be linked to the formation of α-Fe_2O_3 nanophase [40,41]. Emission peaks can represent the atomic transitions of iron vacancies at 434 nm. The band emission at 537 nm and 649 nm was attributed to deep-level or trap-state emission resulting from the recombination of a photogenerated hole with a singly ionised charge state of the specific

defects [42-44]. The peak at 649 nm corresponds to the atomic transitions of oxygen vacancies.

A-Fe2O3 does not exhibit photoluminescence in the bulk due to localised d–d transitions and resonant energy transfer between cations; however, it can be observed when the size of Fe_2O_3 is reduced to the nanometer scale [45]. P. Thomas et al. have prepared ultrafine iron oxide nanoparticles through the hydrothermal method [40]. They reported that the intense blue or yellow band emission at 535 nm and 645 nm was attributed to deep-level or trap-state emission resulting from the recombination of a photogenerated hole with a singly ionised charge state of the specific defects [46-49]. For hybrid Fe_2O_3-Au nanoparticles synthesised using a simple wet chemical method, a sharp peak at 322 nm was observed [41]. This luminescence was related to an electronic transition within the iron oxide (α-Fe2O3) nanoparticle. Therefore, the lowest exciton state of Fe_2O_3 arises from excitation between the mixture of Fe (3d) and O (2p) states in the valence band, and the Conduction Band, which derives from Fe (4s) states. Under excitation, an electron is excited from the valence band to the conduction band, leaving a hole in the valence band. The exciton (-) and the hole (+) move freely and form an exciton; the recombination of the electron and hole in the exciton yields the photoluminescence emission. A broad emission is observed around 400 nm, which may be related to deep-level emissions and primarily results from defects such as interstitials and oxygen vacancies [50].

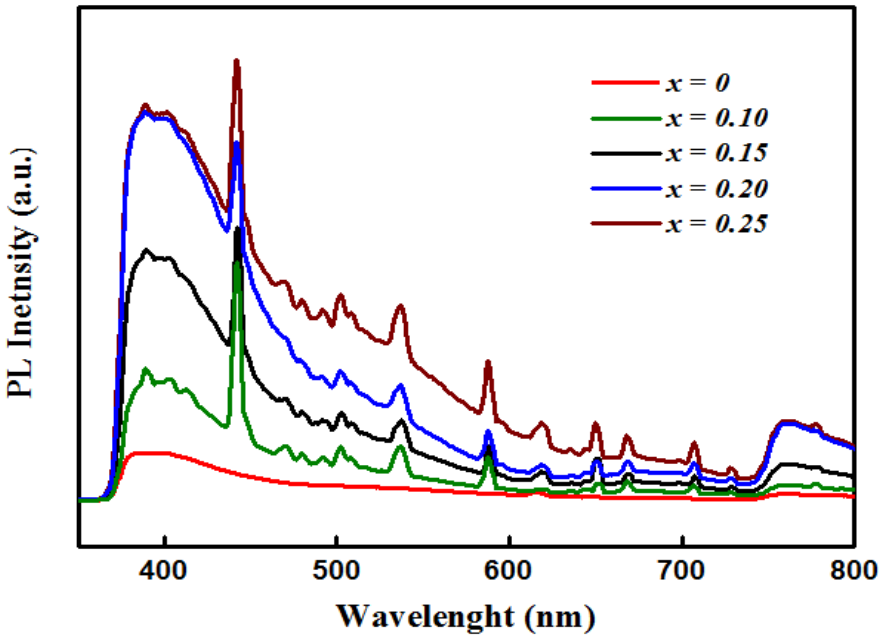

Figure 3.7: *Room temperature PL spectra of nano-structured $Cu_{1-x}Fe_xO$ thin films.*

Numerous theories, including singly ionised oxygen vacancies, interstitial cations, oxygen anti-site, and metal vacancies, have been considered potential causes of these emissions [42]. Consequently, the 434, 537, and 649 nm peaks can be identified as the spectral transitions $^2D^0 \rightarrow {}^2P$, $^1D^0 \rightarrow {}^3P$ of the oxygen atom and the transition 4P0→4D of the iron atom, respectively. The existence of two more peaks at 670 nm and 708 nm in the red region is linked to the doubly ionised oxygen vacancies [51], respectively.

3.4. UV–Visible spectroscopy

Figure 3.8 shows the absorbance (A) spectra of nano-structured $Cu_{1-x}Fe_xO$ thin films in the 200–900 nm wavelength range. One can obtain from these figures that pure and doped CuO films exhibit no apparent absorption in the visible light region (wavelength over 400 nm). Consequently, all films exhibit relatively poor absorbance in the visible light region, and the absorbance increases rapidly with decreasing wavelength due to the direct transition of electrons.

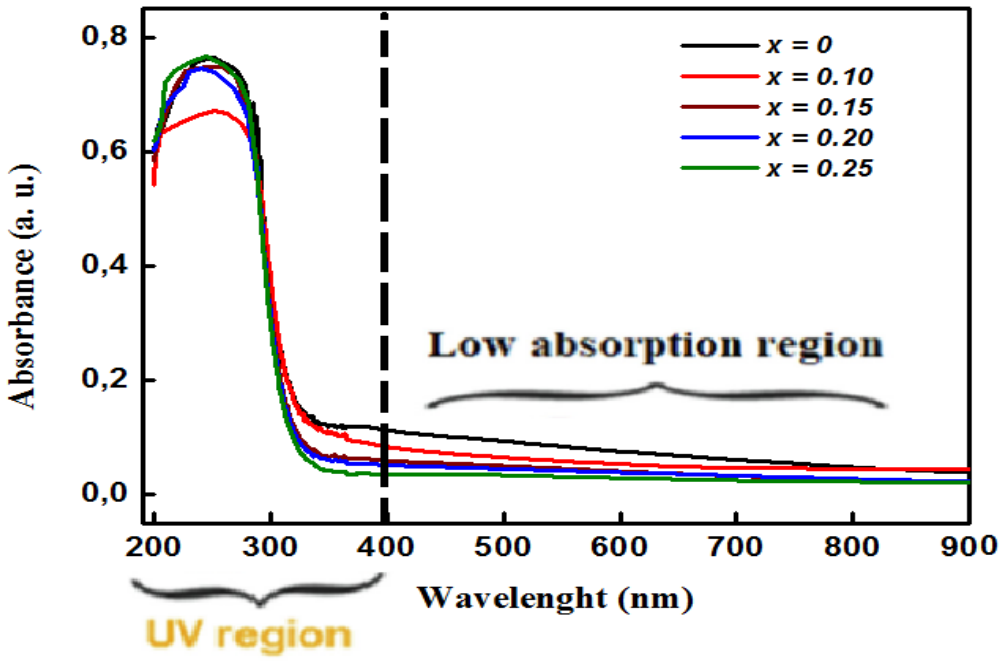

Figure 3.8: *UV–visible absorbance spectra of nano-structured $Cu_{1-x}Fe_xO$ films.*

An absorption edge at around 250 nm is observed for all samples. The related wavelength value is less than that reported for bulk CuO, which is 310 nm [51]. A comparable sharp absorbance peak of greenly synthesised CuO nanoparticles was observed at 280 nm [52], confirming the particle's nanoscale size. This behaviour of nano-structured $Cu_{1-x}Fe_xO$ agrees well with previous reports [51, 52]. Additionally, the absorbance increases

continuously with increasing Fe concentration. This may be attributed to the reduction in crystallite and particle size of the films with increasing doping levels [48, 53]. Additionally, the refinement of crystallite size can lower the film's light absorption [54]. However, the absorbance is augmented with increasing the Ni doping content [55] owing to the photons' prolonged scattering by the generated crystal defects [56].

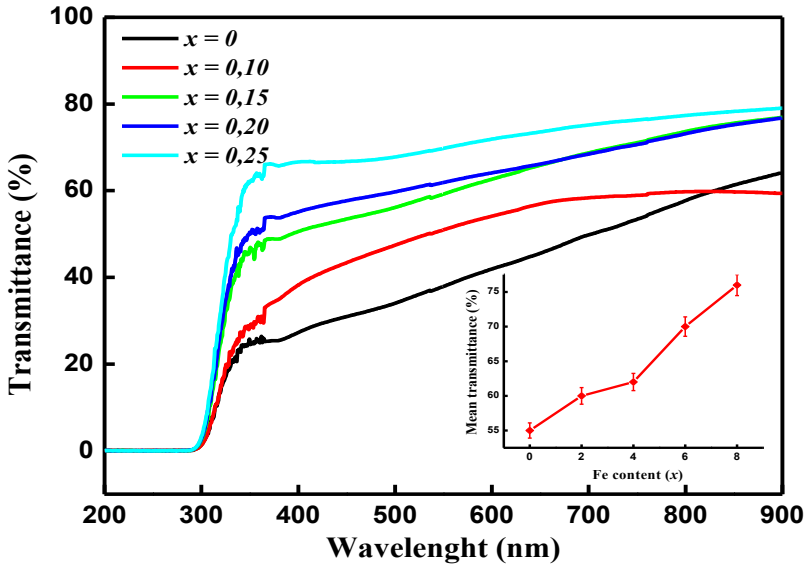

Figure 3.9: *Transmittance versus Fe content in nanostructured $Cu_{1-x}Fe_xO$ films.*

The transmittance (T) of the films, illustrated in Figure 3.9, was calculated from the absorbance (A) by the usual dependence:

$$A = 2 - \log 10\ (\%T) \qquad (3.8)$$

The average transmittance of the nanostructured films rises from 55% to 76 % in the visible range (430–770 nm) (inset in Figure 3.9). Conversely, for p-type cobalt-doped CuO thin films deposited by the reactive magnetron sputtering technique, the transmittance was found to decrease with the increase of Co content [57]. The authors suggested that this behaviour may be due to d–d transitions of the open d shell [58].

3.4.1. Absorption coefficient

The absorption coefficient (α) was obtained from the absorbance spectra of nanostructured $Cu_{1-x}Fe_xO$ films using $\alpha = \ln(10) \cdot A / t$, where t is the material's thickness or the length of the light path through the sample. (Figure 3.10). The absorption coefficient declines as the wavelength rises. The α coefficient shows a non-zero value for energies well lower than the gap [59]. The mean absorption coefficient ranged from ~ 10^3 to ~ $0.5 \cdot 10^5$ cm^{-1}

in the 3.5–5 eV region. This result is characteristic of several semiconductors and could be related to the crystal's internal electric fields, inelastic scattering of charge carriers by phonons, and lattice deformation produced by imperfections/impurities [60].

Similar behaviour was observed for CuO-NPs synthesised at room temperature via a green method, where the variation of α *vs* wavelength has been found to have a high-intensity absorbance peak at 310 nm [61,62]. Therefore, a broad peak is observed at 310 nm in the UV–vis absorption spectrum. This peak indicates that CuO-NPs exhibit maximum absorption in the ultraviolet range, a crucial optical characteristic for solar cell applications. Moreover, α decreases exponentially in the visible region when the wavelength increases; it also decreases exponentially in the ultraviolet region as the wavelength decreases.

From the perspective of fundamental material science the dispersion of the absorption coefficient can be divided into several spectral ranges: (i) high-absorption region involves optical transitions between the valence and conduction band states;(ii) the spectral range which is called the Urbach's exponential tail region where most of the optical transitions take place between localized tail states and extended band states and (iii) the region involves low-energy absorption which occurs due to the optical transitions between the localized states [59].

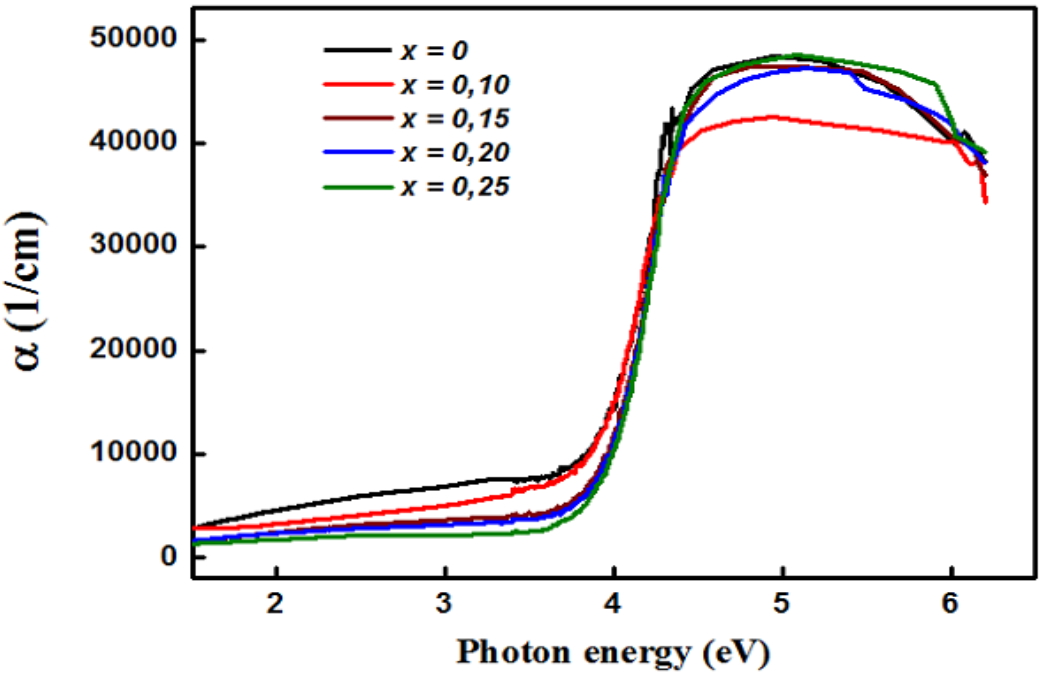

Figure 3.10: The absorption coefficient of nanostructured $Cu_{1-x}Fe_xO$ films.

3.4.2. Urbach energy (E_U)

Along the absorption coefficient curve and near the optical band edge, there is an exponential part called the Urbach tail. This exponential tail appears in the low crystalline, poor crystalline, disordered and amorphous materials because these materials have localised states which extend into the band gap [63]. The following equations give the band tail called Urbach energy (EU):

$$(\alpha h\nu) = \alpha_0 \exp(h\nu / E_U)$$
$$E_U = [d(\ln(\alpha)) / d(h\nu)]^{-1} \quad (3.9)$$

With α_0 being a constant. Figure 3.11a reveals that the plot of ln(α) versus photon energy is linear. The Urbach energy (E_U) is obtained from the slopes of the linear fitting of ln(α) versus the photon energy (hν) (Figure 3.11b). It augmented from 1.413 eV to 1.705 eV with increasing Fe content from x = 0 to 0.25, respectively. The calculated values are higher than those of other metal oxides [64]. It is important, then, to understand the reason for such high values of the Urbach energy and its relation with other material properties, which should be addressed in future work.

3.4.4. Optical band gap

In semiconductors, the optical absorption spectra play a crucial role because they provide fundamental details about the optical band gap and composition. Three main regions can be distinguished in the optical absorption spectra of the semiconductor: (i) weak absorption region, which results from defects and impurities; (ii) absorption edge region, which results from systemic disorder and structural perturbation; and (iii) the region of strong absorption that determines the optical energy gap.

The optical band gap of nano-structured $Cu_{1-x}Fe_xO$ films was determined according to the Tauc expression [65]:

$$\alpha \cdot h\upsilon = B\,(h\upsilon - Eg)^n \quad (3.10)$$

Where h is the Plank constant (6.625 x 10^{-34} *J/s*), υ is the frequency of the incident radiation, Eg is the band gap energy, B is a constant so-called the band tailing parameter, it is related to the material and the matrix element of the transition; α is the absorption coefficient in cm^{-1}, and n is a parameter depending on both the type of transition (direct or indirect) and the profile of

electron density in valence and conduction bands. In the above equation, n = 1/2 for an allowed direct, n = 2 for an allowed indirect, n = 3/2 for a forbidden direct, and n = 3 for a

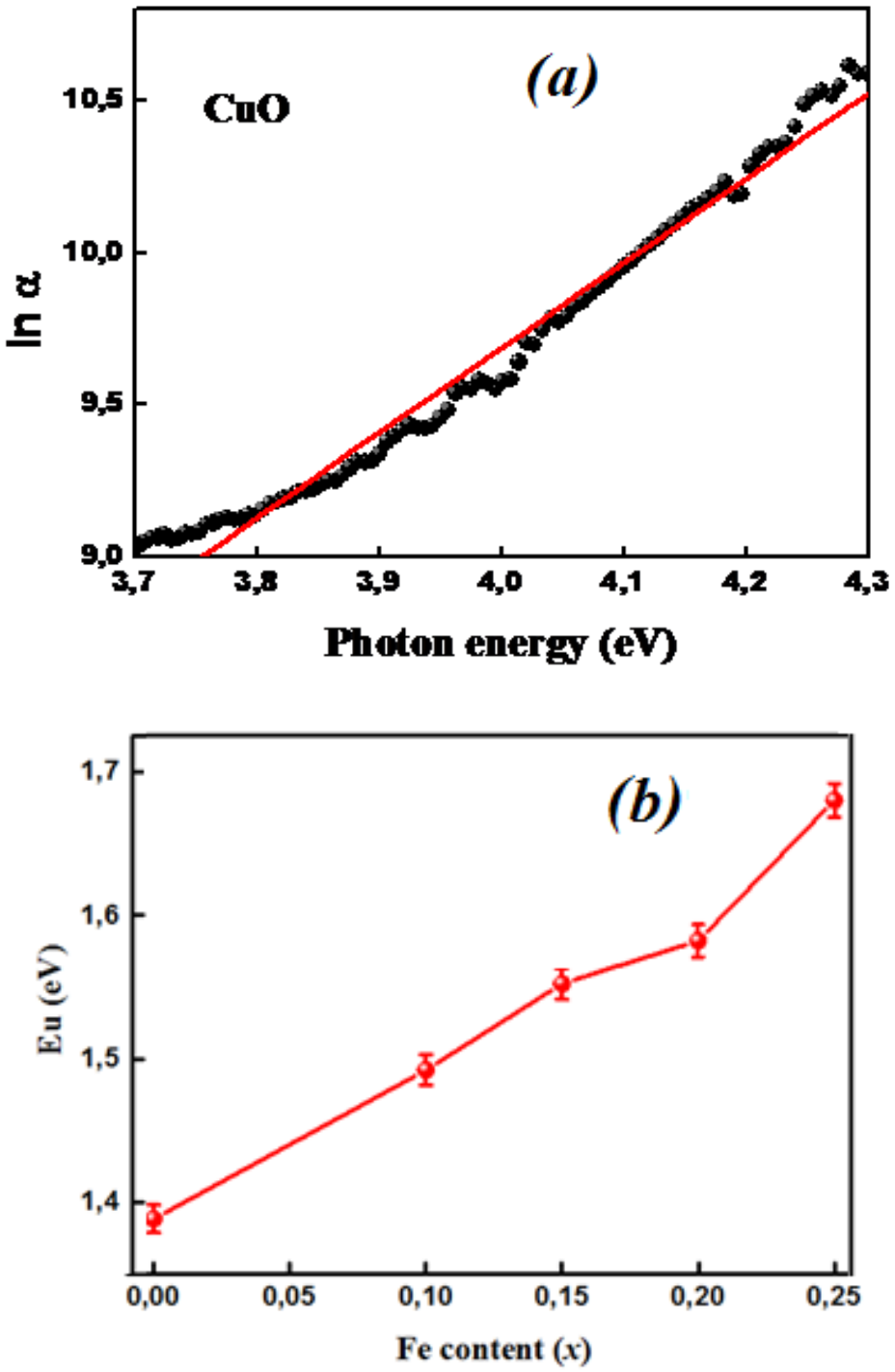

Figure 3.11: (a) plot of ln(α) versus photon energy for CuO and (b) *Evolution of Urbach energy against the Fe content in nano-structured CuFeO film.*

forbidden indirect transition. To determine the nature of the transition occurring, the value of *n* must be determined by plotting the relations $(ahν)^{1/2}$, $(ahν)^2$, $(ahν)^{2/3}$, and $(ahν)^{1/3}$ as functions of the incident photon energy hν [66]. The relation $(ahν)^2$ *vs* hν for the synthesized CuFeO thin films, presented in Figure 3.12 is fitted quite well via Eq. (3.10) indicating that the absorption mechanism is identified as an allowed direct transition where the maximum valence and minimum conduction bands have equal momentum, so $(ahν)^2$ has been used; which fits well with the experimental result. The band gap energy is deduced from the linear portion across the energy axis from the $(αhν)^{1/n}$ versus the photon energy (hν) plot. Hence, the intersection with the energy axis gives the corresponding gap energy [67].

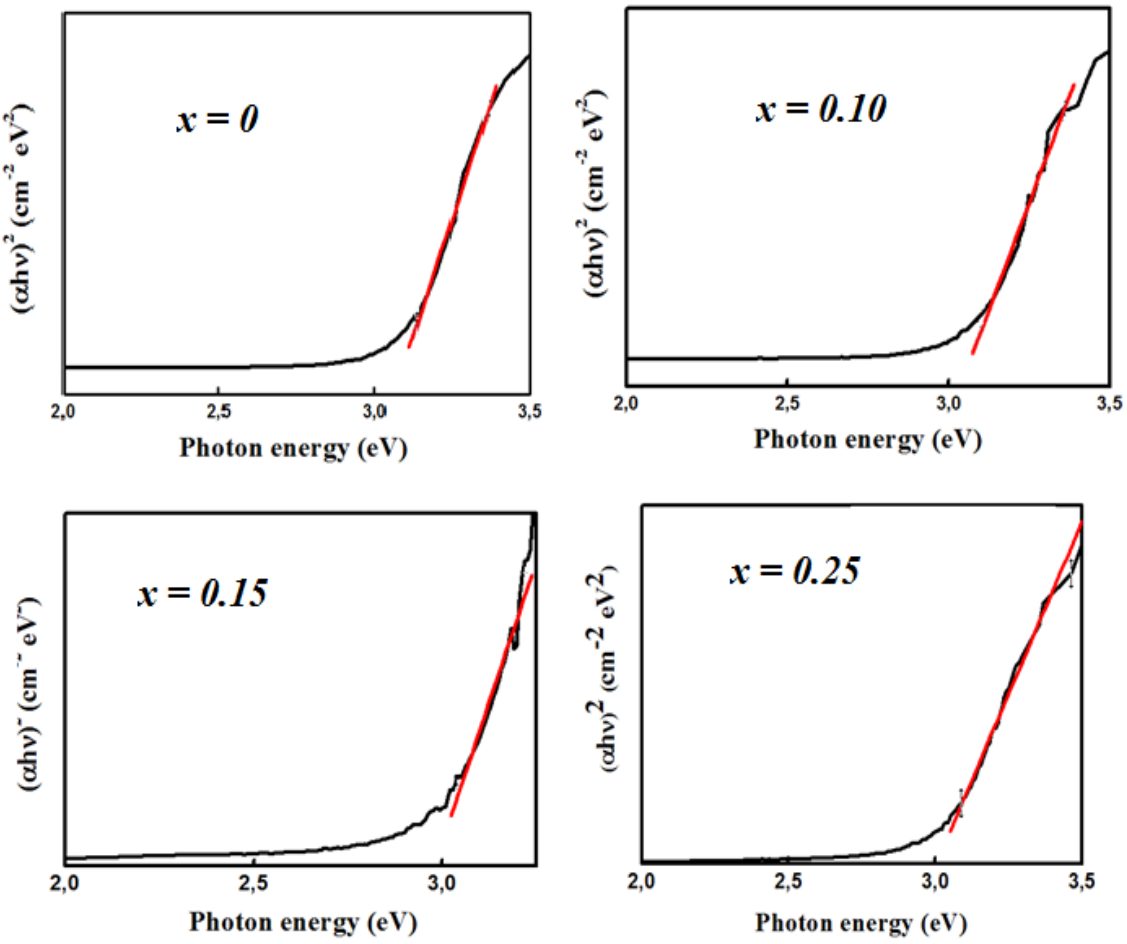

Figure 3.12: *Tauc's plots for the determination of the direct band gap of nanostructured $Cu_{1-x}Fe_xO$ films.*

The Eg values of nano-structured $Cu_{1-x}Fe_xO$ films decreased continuously as the iron content increased from 3.075 eV for pure CuO to 2.974 eV for x = 0.25 (Figure 3.13). One notes that values *Eg* changed contrarily according to E_U values. The diminution in the band gap can be due to the effects of quantum confinement. The drop in Eg might also be related to

the tail-like effect of Fe-doping, where many impurities are inserted into the CuO lattice. This leads to locally introducing distinct energy levels, which interact to form a band.

The extracted Eg values are higher/lower than those reported for doped and undoped CuO owing to the preparation conditions [68-70]. Regarding semiconductors, pure CuO belongs to a p-type semiconductor, characterised by a small band gap ranging from 1.8 eV to 2.5 eV [64,70]. Indeed, various factors, including the doping element, crystallinity, crystallite size, and ionic radii, can influence the bandgap in semiconductors. Compared with bulk CuO, the bandgap of nanostructured CuO is blueshifted, with reported values ranging widely from 1.2 eV to 2.1 eV [70]. The band gap energies calculated for CuO nanotubes synthesised via the wet chemical method are 1.98 eV [71], which is higher than the reported value for bulk CuO (1.85 eV) [72]. This increase in the band gap of the nanotubes is credited to the well-known quantum confinement effect in semiconductors [73]. Other researchers have also reported larger band gaps up to 4.13 eV for 10 nm quantum dots [76] and 3.02 eV for well-aligned arrays of CuO nanoplatelets [77]. Therefore, CuO absorbs strongly throughout the visible spectrum with a slight transparency for bigger bandgap nanostructured samples, which absorb in the UV region.

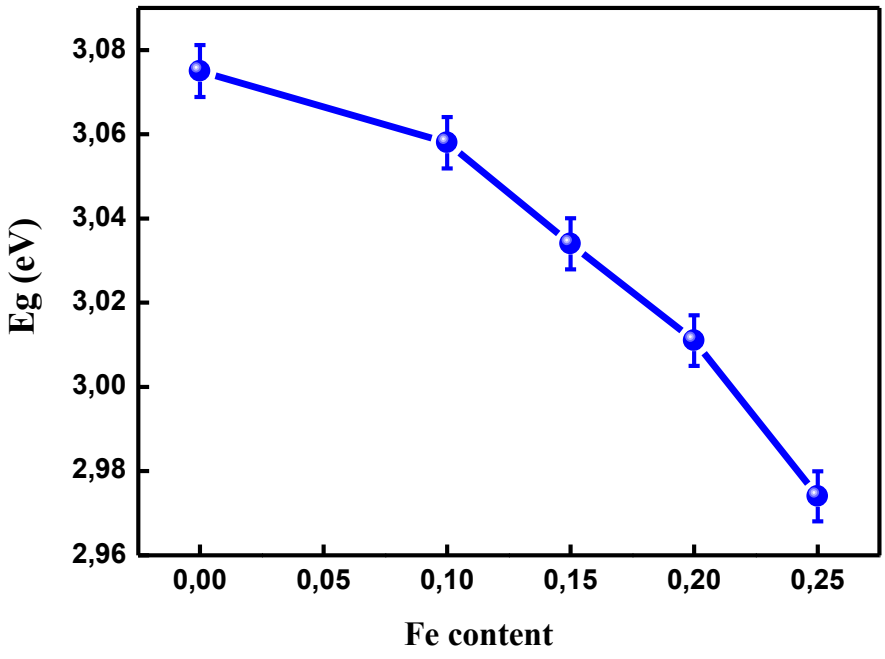

Figure 3.13: *Direct band gap of nanostructured $Cu_{1-x}Fe_xO$ films.*

The energy band gaps are found to be ~3.85 and 3.63, respectively, for CuO and Fe–CuO nanostructures synthesised by the co-precipitation method [78]. Contrarily to Fe, Cr-doping augmented the band gap of CuO thin films prepared by spin coating from 1.6 to 2.3 eV [57]. Additionally, the band gap energy of pure CuO thin films increased from 1.87 to 2.61 eV upon Cr doping, due to band filling and s-d and p-d exchange interactions [78]. In zinc (Zn)-doped CuO nanoparticles prepared by the hydrothermal method, an enhancement of the optical properties has been reported due to Zn doping [79]. The authors found that the optical band gap was reduced from 2.39 eV in pure CuO nanoparticles to 1.82 eV in Zn-doped CuO nanoparticles. They have explained this reduction as a result of the size confinement effect in which Zn-doping led to a decrease in particle size [80].

Hence, since Fe have a low degree of hybridisation for a stable electronic configuration, doping may lead to the creation of a unique energy level between Cu 3d and O 2p, resulting in a narrowed band gap [81]. Therefore, the absorption edge is shifted due to the electrical transition from the valence band to the dopant level and then from the dopant level to the conduction band. The observed shift is attributed to the addition of Fe^{+3} and/or Fe^{+2} in CuO (Cu^{+2}). This addition has a significant effect on the recombination time of charge carriers because doping ions introduce several new Fermi levels above the valence band of CuO, which further assist in absorbing photons with less energy in the visible region [71].

Another factor that may contribute to bandgap narrowing is the presence of a localised t2g state of the Fe doping element, which can be found in the centre of the band gap [82]. We can conclude that the band gap values in the nanostructured Fe-doped CuO decreased because the electrical transition between the conduction band and valence band was interfered with by the creation of several defect energy bands in the presence of Fe inside the band gap of CuO [83].

The CuO optical band gap widening may be attributed to charge migration taking place in 3*d* levels in Fe^{2+} and the strong sp-d exchange interactions between the localised d electrons and band electrons in the Fe dopant [84]. Another reason may be the Moss–Burstein effect, which happens once the carrier concentration surpasses the density of states at the conduction band edge [74,85]. Additionally, band tailings are generally observed in semiconductors to express the band dispersion [86]. The distribution of dislocations/impurities in the material initiates them.

3.4.4. Extinction coefficient and refractive index

The refractive index is one of the most significant characteristics of semiconductors. This property plays a key role in many electronic and optical applications [87]. The refractive index is directly related to the concepts of polarisation ability of atoms when they are subject to an electric field within the materials [88]. The mathematical equation of the complex refractive index (n^*) of thin films is given by Equation (3.11):

$$n^* = n + ik \tag{3.11}$$

The imaginary part (the extinction coefficient k) indicates the amount of light scattering and absorption in the medium per unit volume, and the real part (the refractive index, n) gives information about the refraction of light. The following equations are used to calculate the extinction coefficient and refractive index, respectively [88]:

$$k = \alpha\lambda/4\pi \tag{3.12}$$

$$n = 1/T + [1/(T-1)]^{1/2} \tag{3.13}$$

Here, T is the transmittance and α is the absorbance coefficient.

Variations of refractive index (n) and extinction coefficient (k) at various Fe concentrations as a function of wavelength are presented in Figure 3.14. The refractive index is found to decrease with increasing doping concentration, which can be attributed to the retarded crystal growth resulting from the increased doping concentration [89]. Otherwise, the extinction coefficient of these films is comparatively low, which indicates the smoothness of the surface and homogeneity of the particle size. The decrease of the extinction coefficient with increasing doping concentration represents lower absorption in higher doping [90].

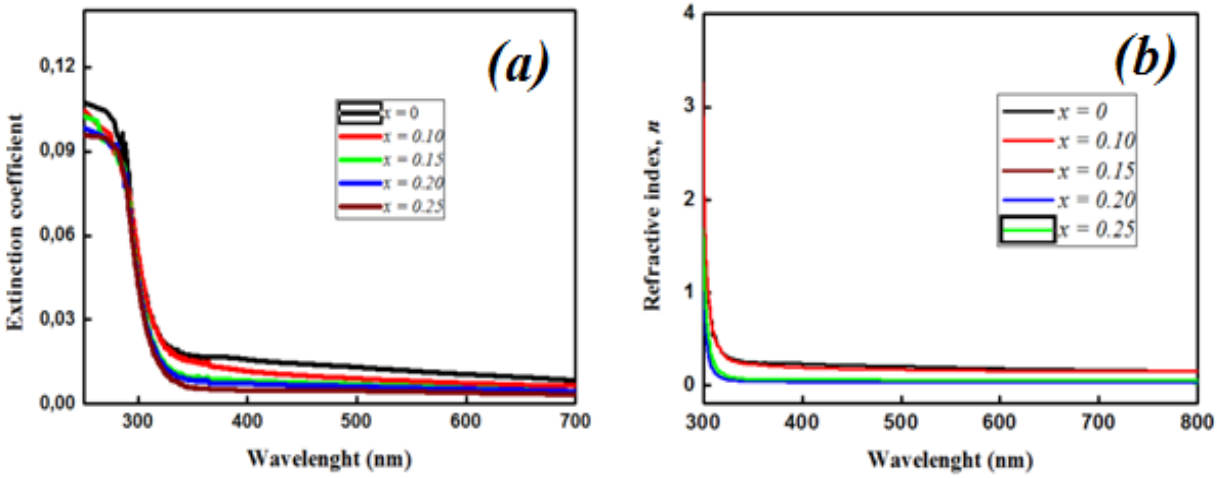

Figure 3.14: *(a) Extinction coefficient and (b) Refractive index of $Cu_{1-x}FexO$ thin films.*

The refractive index (n) of a material is a number that describes how light will propagate through it. Light travels at different speeds in materials with different refractive indices (n), which can be altered by modifying the material's density [91]. There appears to be a relationship between these two properties. Several approaches have been explored to understand the nature of this correlation. The importance of studying this correlation originated from the fact that refractive index data for some groups of semiconductors do not exist at a satisfactory level [92]. Also, the calculation of n has a vital role in the investigated studies of the optical features, such as with optical transmission, molar refraction, molar polarizability, energy gap, Urbach energy, optical dielectric constant, static dielectric constant, effective atomic numbers, and mass attenuation coefficients, of glass systems as potentially useful for radiation shielding properties, radiation protection applications, and radiation dosimeters [87,93]

Many empirical relationships have been proposed to predict the experimental refractive index within a range of energy gaps. The pioneering equation of Moss [66,91] suggested a simple equation based on the relationship of a material's electron energy levels with the effective optical dielectric constant. This equation can be written as

$$E_g n^4 = k \tag{3.14}$$

where k is a constant corresponding to 10^8 eV.

To improve the predictions of Moss's Equation, Herve and Vandamme (H.V.) have introduced a theoretical relationship based on the oscillatory theory. Their equation can be expressed as [94]:

$$n = \sqrt{1 + \left(\frac{A}{E_g + B}\right)^2} \tag{3.15}$$

Where A represents the hydrogen ionisation energy with the value of 13.6 eV, and B encodes the difference between the ultraviolet (UV) resonance energy $\hbar\omega 0$ and Eg. The alteration of refractive index (n) as a function of the Fe content in CuFeO thin films was also shown in Table 3.4 for these two models.

Table 3.4: *Optical parameters for the CuO films having different Fe concentrations.*

x	Moss relation		Herve & Vandamme		ε_0
	n	ε_∞	n	ε_∞	
0	2.434	5.926	2.326	5.411	9.049
0.10	2.438	5.944	2.331	5.437	9.107
0.15	2.446	5.969	2.339	5.472	9.184

0.20	2.447	5.991	2.345	5.502	9.252
0.25	2.455	6.030	2.357	5.558	9.372

One can see that the values of the refractive index increased from 2.434 to 2.455 with increasing Fe content. Nevertheless, the increasing rate appears to be correlated with the used models. It may be remarked that the refractive index of the materials strongly depends on the band gap energy.

The refractive index of bulk CuO is equal to 2.63. For CuO thin films, the refractive index varies in the range of 1.5 to 3.5, depending on the deposition conditions [95-98]. Dhanasekaran et *al.* [95] found values of the refractive index ranging from 2 to 3.5 when the bath temperature was varied from 30 °C to 90 °C. An increase in film thickness leads to the formation of denser films, resulting in an increase in refractive index for CuO thin films prepared by the SILAR method [98].

3.4.5. Optical dielectric constant

The study of materials' dielectric properties is important for various electronic device technologies because it is correlated to their ability to obstruct electron transit when polarised by an external electric field [99].

Identification of the dielectric characteristics of metal oxide semiconductors is crucial for various electronic device properties. Either static or high-frequency dielectric constants were calculated for all the films. The high-frequency dielectric constant (ε_∞) value was obtained from the following relation $\varepsilon_\infty = n^2$ where n is the refractive index. The static dielectric constant (ε_0) of the CuO thin films was obtained by using an equation which states the energy band gap dependence of ε_0 for semiconductor compounds in the following form :

$$\varepsilon_0 = 18.52 - 3.08Eg \qquad (3.16)$$

The calculated n, $\varepsilon\infty$ and ε_0 values of the Fe-doped CuO thin films, which correspond to different dopant concentrations, are given in Table 3.4.

3.5. Magnetic properties

Figure 3.15 shows the room temperature magnetisation as a function of applied magnetic field (M–H) for the nanostructured CuO sample. The data show that the magnetisation does not attain the saturation value even at the maximum applied magnetic

field (10 kOe). The M-H loops depicted a combined behaviour, with a small hysteresis at low fields and linear behaviour at high fields. These behaviours are separated, using the equation: $M(H) = M_{FM}(H) + \chi H$, where the χH term accounts for the paramagnetic (PM) or antiferromagnetic (AFM) contribution at high magnetic fields, and the MFM term accounts for the weak ferromagnetic contribution. The coercive field and remnant magnetisation of the ferromagnetic component are about 17.6 Oe and 4.67 10^{-4} emu, respectively (inset of Figure 3.15). According to the hysteresis plot, Sreeju et al. Reported the ferromagnetic behaviour of the CuO nanostructures in the temperature range from 20–300 K [100]. The coercivity at T = 20°C and T = 300 °C was estimated as 2945.2 G and 153.8 G, respectively. A similar interesting observation has been reported for CuO nanorods in the temperature range of 5–300 K [101].

Since bulk CuO is paramagnetic at room temperature, the observed ferromagnetism in nano-structured CuO sample - called *d^0 ferromagnetism*- can be related to vacancies and the uncompensated Cu^{2+} superficial spins on the surface of nanoparticles , which reorient in the direction of the magnetic field [102-104]. Therefore, the moment non-compensation can result either from disparity in the number of up and down spins due to the spin-structural disorder at the surface of CuO nanoparticles or from the existence of defects [105,106]. The weak ferromagnetism can also originate from the superexchange interaction between Cu^{2+}–O^{2-}– Cu^{2+} couplings [107]. However, the PM behaviour is derived from the surface Cu atoms that behave as partial spin-glass subsystem [108]. Similar behaviour has been found in pure CuO nanoparticles prepared by the sol-gel method [83,109].

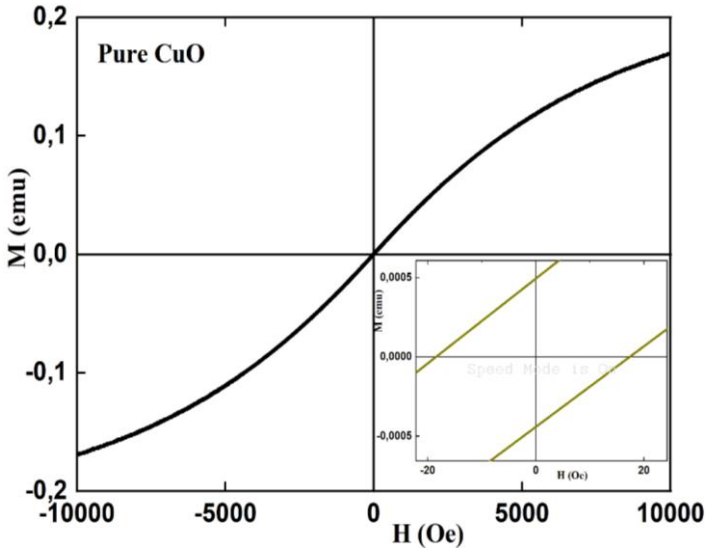

Figure 3.15: *Room temperature M–H hysteresis curve of the nano-structured CuO film.*

Figure 3.16 displays the hysteresis loops recorded at room temperature for nanostructured Fe-doped CuO thin films. We note here that the background magnetic contribution of the substrate has been subtracted from all of the magnetisation data. The hysteresis loops show the same trend. They are saturated and exhibit a ferromagnetic behaviour with a sigmoidal shape type. The inset in the figure above reveals a considerable change in the H_C and Mr values. We note that the shape and width of the hysteresis can be affected by the physical parameters of the samples, such as the chemical composition of the compound, exchange interactions due to cation distribution, porosity, and grain size, among others. It is also renowned that at the beginning of the applied field, the magnetic domain reorientation results in the magnetisation increasing rapidly. After that, due to spin rotation, the magnetisation slows and eventually saturates. Magnetic parameters, such as saturation magnetisation (Ms), remnant magnetisation (Mr), coercivity (Hc), squareness ratio (S), and anisotropy constant (K1), can also be calculated using the hysteresis loop.

The following two mechanisms could explain the observed ferromagnetism in Fe-doped CuO samples [110]:

(1) The first mechanism is the *super-exchange interaction*. In a high-spin state, a Fe ion has five d electrons with the total spin of S = 5/2 or 2 for the valence of 2 and 3, respectively. A Cu^{2+} ion has a total spin of 1/2. Fe ion substitution into Cu^{2+} ion enhances the magnetic moment. The extra magnetic moment may be linked to the lattice of Cu^{2+} spins through a super-exchange interaction, mediated by an O^{2-} ion.

(2) The second possible origin of ferromagnetism is an *F-centre-mediated* exchange interaction. For oxide materials, oxygen vacancies exist. So, indirect ferromagnetic coupling among the neighbouring Fe^{3+} ions via a localised carrier near an oxygen vacancy could occur.

For $x \leq 0.20$, the strong ferromagnetic order has an intrinsic origin and was related to the monoclinic CuO structure (DMS phase), as confirmed by XRD results, where no impurities are observed. Consequently, doping CuO with Fe replaces a nonmagnetic Cu^{2+} ion with a magnetic Fe transition metal ion, thereby enhancing CuO's room-temperature ferromagnetism (RTF). However, for the x = 0.25 sample, the RTF with a high Ms value (0.603 emu) is obtained, compared to other samples. It has been reported that in a two-phase system, the ferromagnetic signal originates from impurities in the sample [107]. However, due to a small amount of a secondary α-Fe2O3 (8%) phase, which exhibits an

antiferromagnetic behaviour with a weak spontaneous magnetisation of ~0.4 $Am^2 kg^{-1}$ due to spin-canted and defect moments [111], its contribution to the total magnetic moment is negligible. Moreover, since the experimental conditions are carefully controlled, contamination during sample synthesis or annealing could also be ruled out.

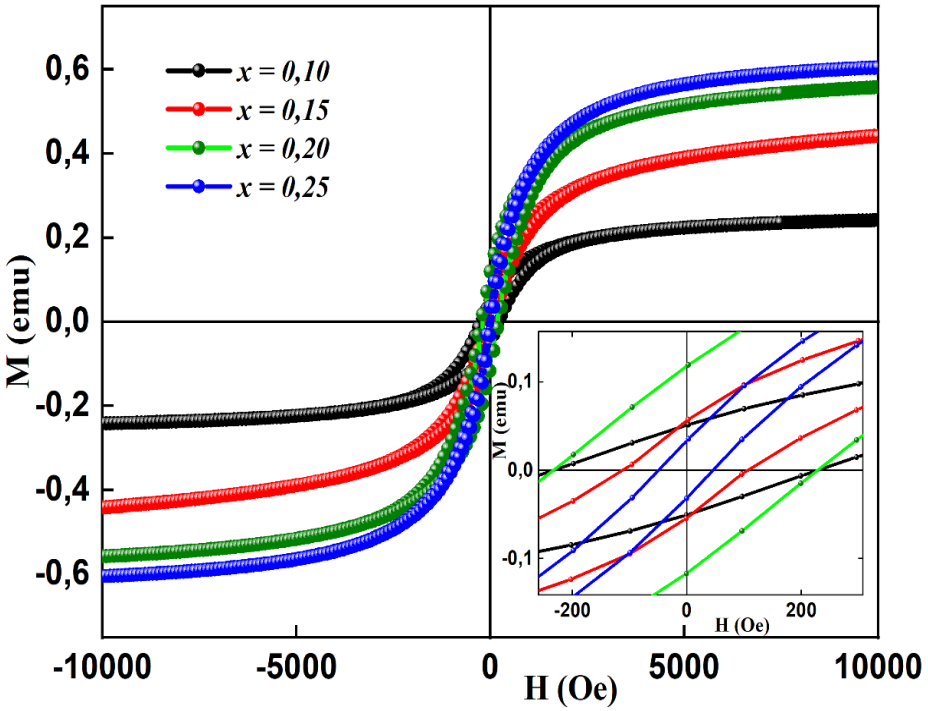

Figure 3.16: *Room temperature M–H hysteresis curves of the nano-structured $Cu_{1-x}Fe_xO$ films.*

Oxidation states of Fe ions in CuO play a critical role in the magnetic properties of CuO. It has been mentioned that in the Fe^{3+} substituted samples, the p-type nature is retarded while the oxygen deficiency is reduced. This type of change is not expected in the case of Fe^{2+} substitution. In the case of Fe^{2+}, oxygen vacancies could have increased as Fe^{2+} has the same charge and has a crystal radius of approximately 0.77 Å, which is about 8.5% more than that of the Cu^{2+} ion. As a result, oxygen vacancy-mediated ferromagnetism could have been possible. The exchange interaction would then have been through an electron trapped at the oxygen vacancy site, V_o [110]. The M_1–V_o–M_2 interaction [112] is generally ferromagnetic in the case of Fe^{3+}–V_o–Fe^{3+} [110]. In the case of Fe^{2+}–V_o–Fe^{2+}, it is weaker but still ferromagnetic. However, in a homogeneous solid solution, finding neighbouring Fe^{2+} or Fe^{3+} ions is less probable. Moreover, we have seen a predominant increase in oxygen content with substitution. Hence, be it Fe^{3+} or Fe^{2+}, an enhancement of ferromagnetism, mediated by oxygen deficiencies, seems inappropriate.

Metal–oxygen–metal double-exchange interactions have played an important role in magnetism. This exchange happens between two atoms of different valence (Figure 3.17). For double exchange to occur, an electron from Fe^{2+} has to move to the oxygen ligand while an electron from the oxygen moves to Fe^{3+} [113]. While superexchange most often results in antiferromagnetism, double exchange becomes the origin for ferromagnetism due to parallel spin alignment. An increase in oxygen content thereby makes such exchange integrals stronger. Fe3+ substitution opens up a better chance of Fe^{3+}–O^{2-}–Cu^{2+} superexchange or a Fe^{3+}–O^{2-}–Cu^{2+}–O^{2-}–Fe^{3+} double superexchange phenomena.

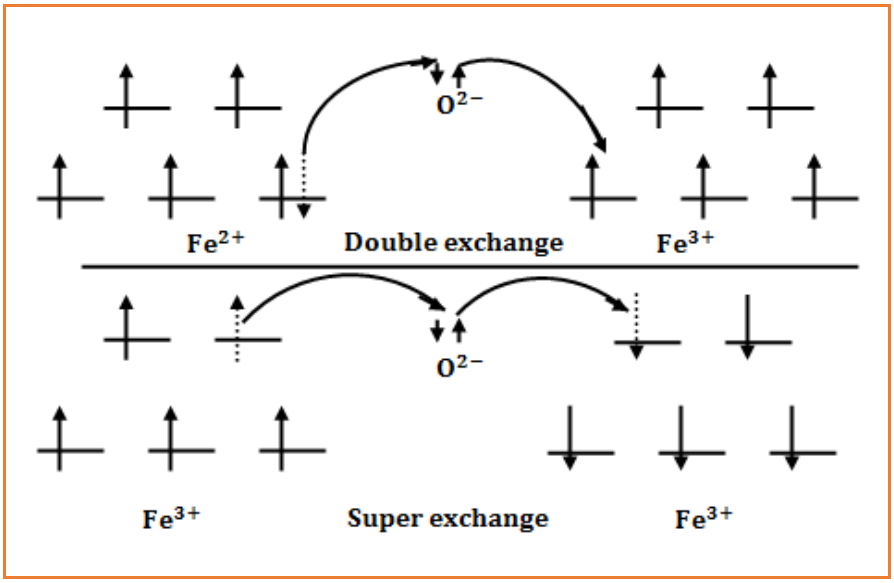

Figure 3.17: *Double Exchange vs. Super-exchange magnetic coupling. Both are facilitated by an oxygen ligand [113].*

The electronic configurations of Cu^{+2}, Fe^{+3} and Fe^{+2} are $3d^9$, $3d^5$ and $3d^6$. In high spin state, the magnetic moments of Cu^{+2}, Fe^{+3} and Fe^{+2} are 1.73 μ_B, 5.9 μ_B and 4,89 μ_B, respectively. Therefore, the incorporation of Fe in the CuO lattice enhances the magnetic moment. The extra magnetic moment may be coupled to the lattice of Cu^{2+} spins via a superexchange interaction, mediated by an O^{2-} ion, which leads to the emergence of a ferromagnetic state. Similar previous study demonstrates that substituting another transition metal ion, such as Fe^{2+} ions, for copper significantly increases the room temperature ferromagnetism in CuO nanorods [114]. It has been demonstrated that in $Fe_{2-x}Cu_xO_3$ ferromagnetism is enhanced with increasing Cu content [115]. In x=1, i.e. $FeCuO_3$ sample, maximum ferromagnetism has been observed. This enhancement hints at a stronger

ferromagnetism in Cu–O–Fe than Fe–O–Fe couplings. Thereby in Fe-substituted CuO such strong interactions may also contribute to the enhanced ferromagnetism.

The observed RTF behaviour in our $Cu_{1-x}Fe_xO$ samples is comparable to that described in the literature for oxides diluted magnetic semiconductors [116-119] and Fe-doped CuO nanopowders. Some studies have been conducted on CuO doped with Fe cations, which typically assume a trivalent state when diluted in oxides and, therefore, exhibit a magnetic moment of pure spin. For example, Manna and De [114] prepared Fe-doped CuO nanorods using a hydrothermal method and reported feeble ferromagnetism at room temperature. The nanoparticle shape anisotropy was found to determine the magnetic behaviour of the $Cu_{1-x}Fe_xO$ nanorods, and ferromagnetism was considerably enhanced by the substitution of iron in the copper sites. Gaur et *al.* [120] reported the synthesis of Fe-doped CuO nanostructures using a wet chemical method. They observed superparamagnetic behaviour at room temperature. Furthermore, Liu et *al.* [121] proposed that the RTF observed in Fe-doped CuO nanopowders generated using the sol-gel and co-precipitation methods may be attributed to an indirect coupling among the Fe^{3+} ions via a localised carrier at an oxygen vacancy.

3.5.1. Saturation magnetisation

The saturation magnetisation, Ms, increases from 0.245 to 0.603 emu as the Fe content increases from 0.10 to 0.25 (Figure 3.18). The rise in the Ms indicates the incorporation of Fe ions into the CuO lattice. Comparable behaviour was observed in Fe-doped CuO nanofilms, where Ms augmented from 0.14 to 0.73 emu/g when the Fe content was increased [122]. For the $Cu_{0.95}Fe_{0.05}O$ sample prepared by a solid-state reaction, the saturation magnetisation was about 0.46 emu/g, and the coercivity was 126 Oe [123].

The electronic configurations of Cu^{2+}, Fe^{3+}, and Fe^{2+} are $3d^9$, $3d^5$, and $3d^6$. In the high spin state, the magnetic moments of Cu^{2+}, Fe^{3+}, and Fe^{2+} are 1,73 μ_B, 5,9 μ_B, and 4,89 μ_B, respectively. Therefore, incorporating Fe in the CuO lattice enhances the magnetic moment. The extra magnetic moment may be coupled to the lattice of Cu^{2+} spins via a super-exchange interaction through an O^{2-} ion, which leads to the emergence of a ferromagnetic state.

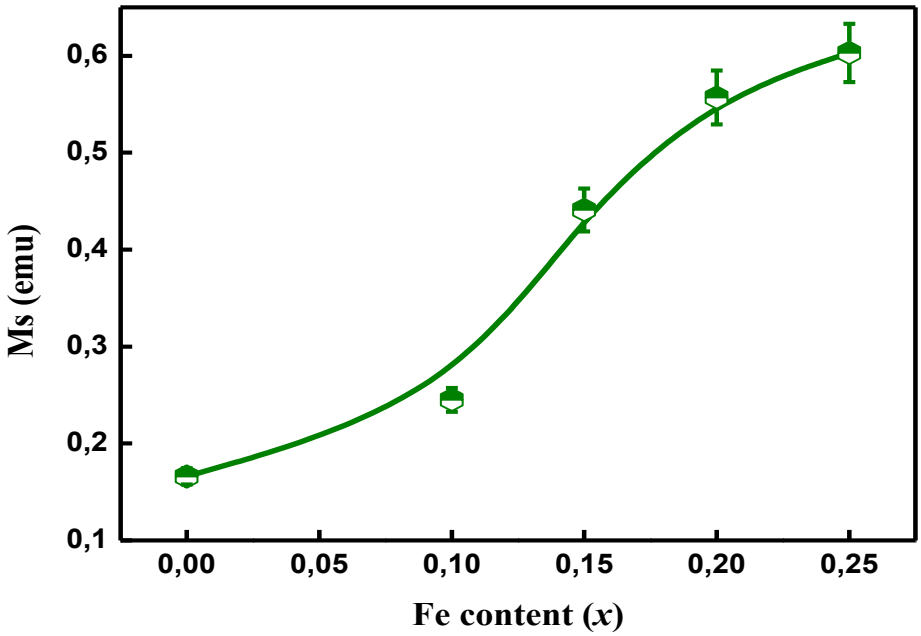

Figure 3.18: *Evolution of the saturation magnetisation versus Fe content.*

3.5.2. Coercivity and anisotropy

The Coercivity is an indicator of the magnetic field intensity required to surpass the energy of magnetic anisotropy. Figure 3.19 displays the coercivity (Hc) as a function of Fe content. It shows sawtooth-like behaviour as a function of Fe content. It reaches maximum values of approximately 229.5 and 231.5 Oe for x = 0.1 and 0.2, respectively. It then decreases to 110 Oe for x = 0.15 and drops to 46.5 Oe for x = 0.25. The coercivity can be altered by numerous parameters, including particle shape and size, magnetic anisotropy, competing magnetic interactions, and structural defects that hinder magnetic domain wall motion. The variation in the coercivity exhibits a dissimilar behaviour to the r.m.s. strain variation against the Fe-doping content, as revealed in the inset of Figure 3.18.

The reduction in the coercivity to 46.5 Oe for x = 0.25 might be related to the crystallite size reduction to about 32.74 nm and the particle size refinement to an average value of about 64 nm. The variation in local magnetic interaction and a non-uniform distribution of Fe ions into the CuO lattice give rise to magnetic domain formation and pinning changes. The nature and density of grain boundaries may vary non-linearly with Fe-doping content.

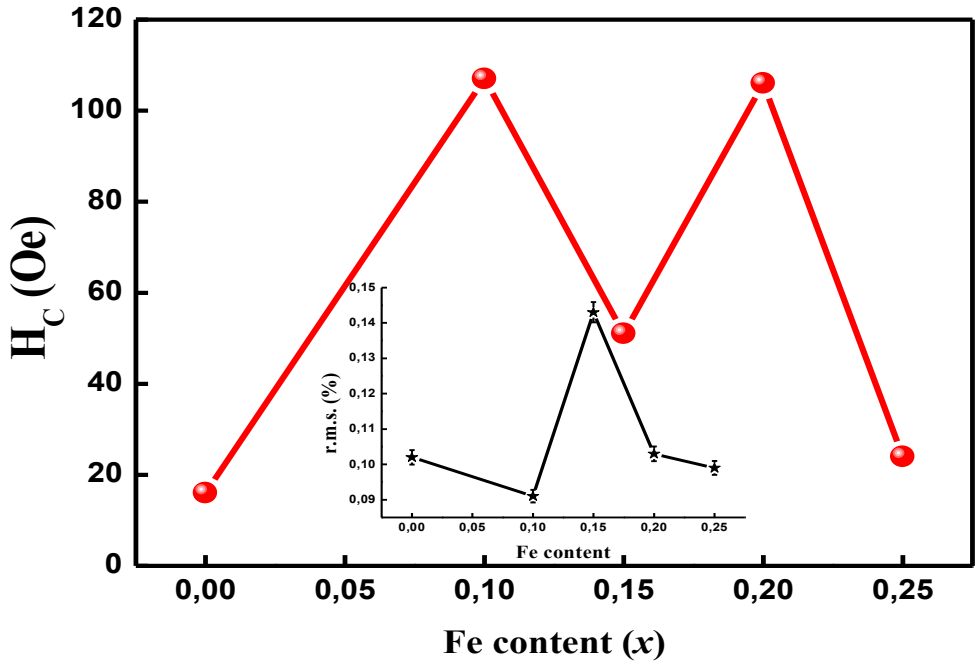

Figure 3.19: *Evolution of the coercivity and saturation magnetization versus Fe content. The inset displays the variation in the r.m.s. strain as a function of Fe-doping.*

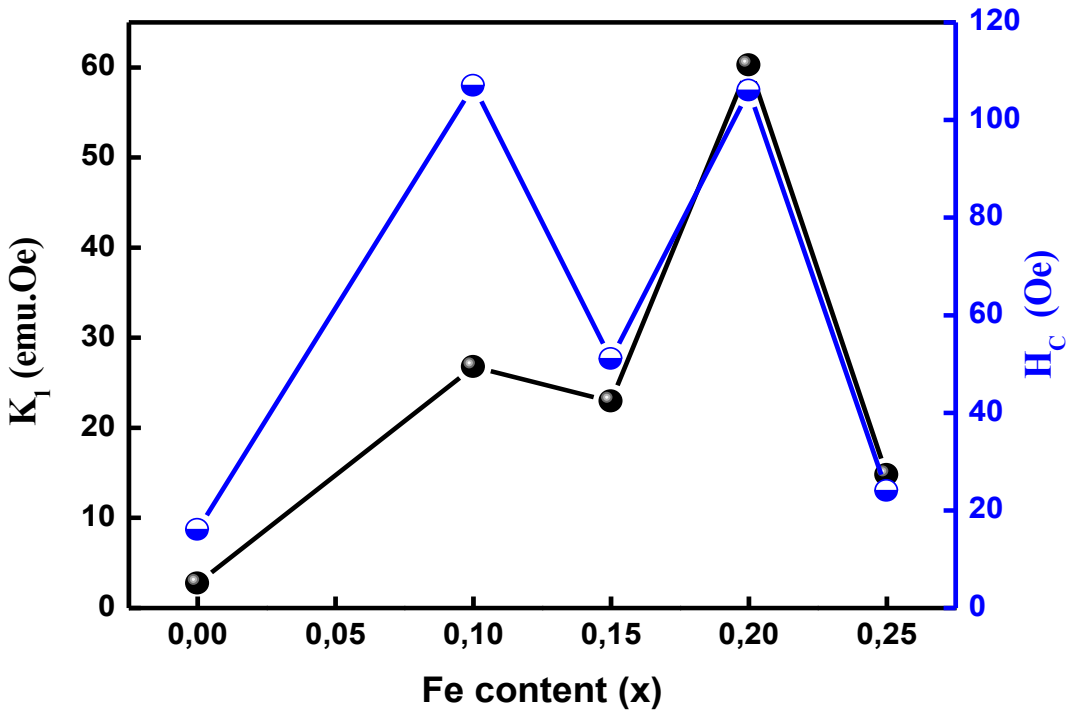

Figure 3.20: *Evolution of the coercivity and anisotropy constant vs. Fe content.*

The physical nature of magnetism arises from the electron spin as well as the orbital motion (see Appendix). The origins of magnetic anisotropy can also be assessed similarly. Two adjacent electrons will exhibit a type of spin coupling, which maintains the parallel motion of the electrons [124]. This will not cause them to have a similar direction, as it depends on the angle of the spins rather than the direction; any contribution from this coupling to magnetic anisotropy would be negligible. Similarly, there would be an orbit lattice coupling, which would be strong because the orientations of the orbitals are fixed to the lattice. Now, the spin-orbit coupling, when the spin is under the influence of the field, will try to reorient itself, but the orbit will resist this reorientation as it is fixed to the lattice. The energy required to rotate the spin to overcome the spin-orbit coupling is called the anisotropy energy [124,125].

While there is scientific consensus on the fact that the significant contribution to the anisotropy constants K_0, K_1, K_2… are the spin-orbit coupling. There is no precise or general method for calculating their values from these principles, as the crystal structure greatly influences them. Since anisotropy is strongly dependent on the structure, as expected, with an increase in temperature, anisotropy decreases [124]. Anisotropy contributes significantly to the coercive field, and just like how coercivity tends to zero as the temperature approaches the Curie temperature TC, anisotropy vanishes at the Curie temperature. The magnitude of the anisotropy constant K_1 is defined as the strength of the anisotropy in any particular crystal. The anisotropy constants are calculated using the following equation [126], $Hc = (0.98 \times K_1) / Ms$, where Hc and Ms denote the coercivity and saturation magnetisation. It is seen that the value of K_1 shows the same behaviour as coercivity (Figure 3.20). It was reported that the anisotropy strongly contributes to the Hc in doped oxides [127].

Vijayalakshmi et *al.* Doped CuO nanoparticles with Co (Cobalt) via a wet chemical route and studied their magnetic properties [128]. They reported that Co-doped CuO nanoparticles exhibited higher values of coercivity and retentivity when compared to the pure CuO nanoparticles. They exhibited superparamagnetic behaviour, rendering the synthesised CuO nanoparticles essential sources in the biomedical field. Chandrasekar et *al.* synthesised pure and nickel (Ni)- doped copper oxide (CuO) nanoparticles via the hydrothermal method and reported that Ni doping enhanced the magnetic properties of CuO nanoparticles [129].

3.5.3. Squareness ratio

The squareness ratio (S = Mr/Ms) is given by the ratio of the remnant magnetisation (retentivity) to the saturation magnetisation values. It provides the information regarding whether nanoparticles are multiple magnetic domains (MD) [S value is <0.5] or single magnetic domains (SD) [S value is >0.5]. Changes in magnetisation occur by uniform rotation in SD grains and domain wall motion and domain transitions (creation or annihilation of domain walls) in MD grains. Materials with a higher S value are plausible candidates for use in magnetic recording and memory devices. In Figure 3.21, the S values are found to be in the range of 0.0017 to 0.479, suggesting the prepared films are in the MD structure. Additionally, a clear idea about the inter-grain magnetic interactions in the materials may be understood with the numerical values of S [130]. The non-zero values confirm the inter-grain magneto-static interaction in the materials [131](i) S = 0.5 authorises the random grain distribution and non-interacting, and (ii) S < 0.5, as in our case, authorises the magneto-static interactions between grains. This may be one of the reasons for the superior magnetic parameters of high-Fe-doped CuO. Analogous results were obtained for Ni-doped CuO nanoparticles with x = 0.0, 0.02, 0.04, 0.06, and 0.08 produced by the chemical sol-gel route [132].

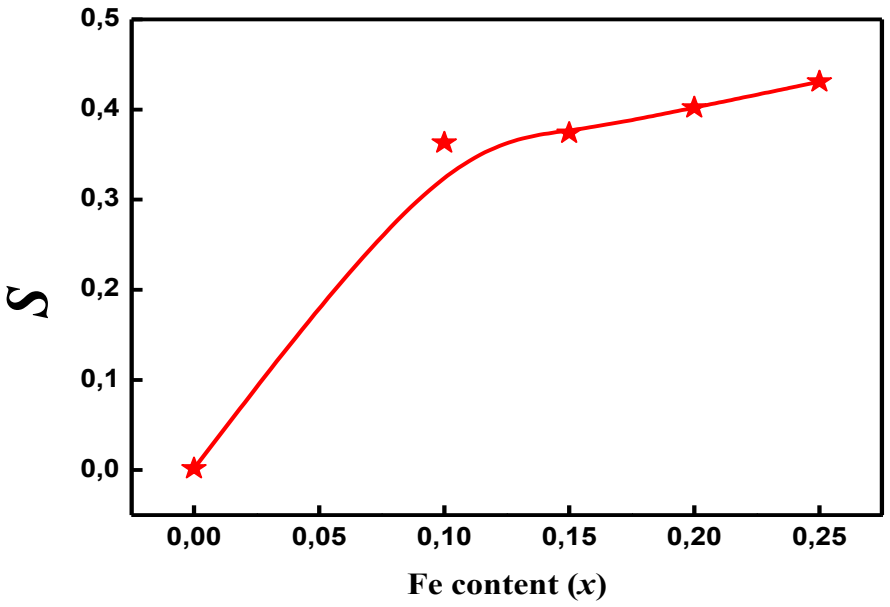

Figure 3.21: *Variation of magnetic squareness ratio of $Cu_{1-x}Fe_xO$ thin films.*

3.6. Electrical properties

The presence of dopants, as well as their concentration in CuO, may influence the chemical and physical properties. Furthermore, the presence of dopant affects the stoichiometry and crystallinity of CuO, thereby impacting its conductivity. Figure 3.22 shows the variation of electrical resistivity (ρ) of $Cu_{1-x}Fe_xO$ films. It can be seen that the resistivity decreases steadily with Fe content, attaining a minimum value of 5.8×10^{-3} cm for $x = 0.25$. Simultaneously, the electrical conductivity was found to be in the order of 10^{-2} S/cm, showing an increasing trend with the dopant concentration. The incorporation of Fe into the CuO lattice was found to be effective in increasing electrical conductivity at room temperature.

For pure CuO, the electrical conductivity is found to be $2x10^{-2}$ S/cm. This value is higher/lower than those reported for pure CuO. We note that the electrical performance of pure CuO can be influenced by its morphology, preparation method and chemical composition. Shao et *al.* reported a value of electrical conductivity of a p-type CuO nanostructure as 7.8×10^{-4} S/cm [133]. Jeong et *al.* observed a higher electrical conductivity value for smaller grain-sized CuO due to the dominance of conductivity in the grain rather than that of the grain boundary [134]. Furthermore, the presence of a non-stoichiometric defect, which is responsible for modulating charge carrier concentration, can impact the electrical properties. For example, Kuryshchuk et *al.* have obtained resistivities of 18.69 and 5.96 kΩ.cm for CuO thin films formed by reactive magnetron sputtering at 300 and 523 K, respectively [135]. An enhancement in CuO conductivity caused by a non-stoichiometric defect resulting from an increase in oxygen partial pressure has been reported [136].

For Fe-doped CuO samples, the decrease in the electrical resistivity can be related to the structural defects introduced through Fe doping, which alters the material's electronic structure and induces changes in energy band structure by adding defect levels and variations in charge carrier mobility [110]. Figure 3.23 shows the decrease in carrier concentration as Fe content increases. The reduction of carrier concentration is observed to facilitate the carrier mobility and gives rise to an improvement in conductivity. The positive values of the carrier concentrations, obtained in the range of 10^{17} cm^{-3}, show that the deposited films are of type (p). Consequently, its resistivity is associated with the generated holes in the valence band by Cu vacancies [111]. Nasir et *al.* found that carrier densities of $Cu_{1-x}Fe_xO$ (x = 0.000, 0.027,

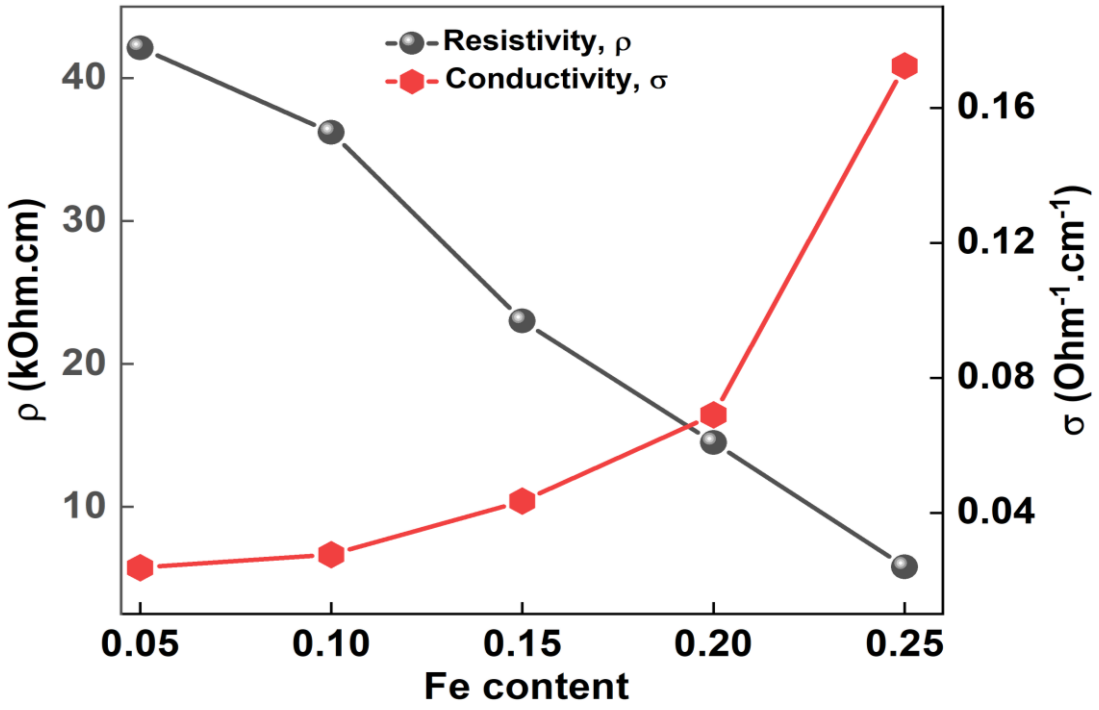

Figure 3.22: *Variation of the electrical resistivity (ρ) and conductivity (σ) of $Cu_{1-x}Fe_xO$ thin films*

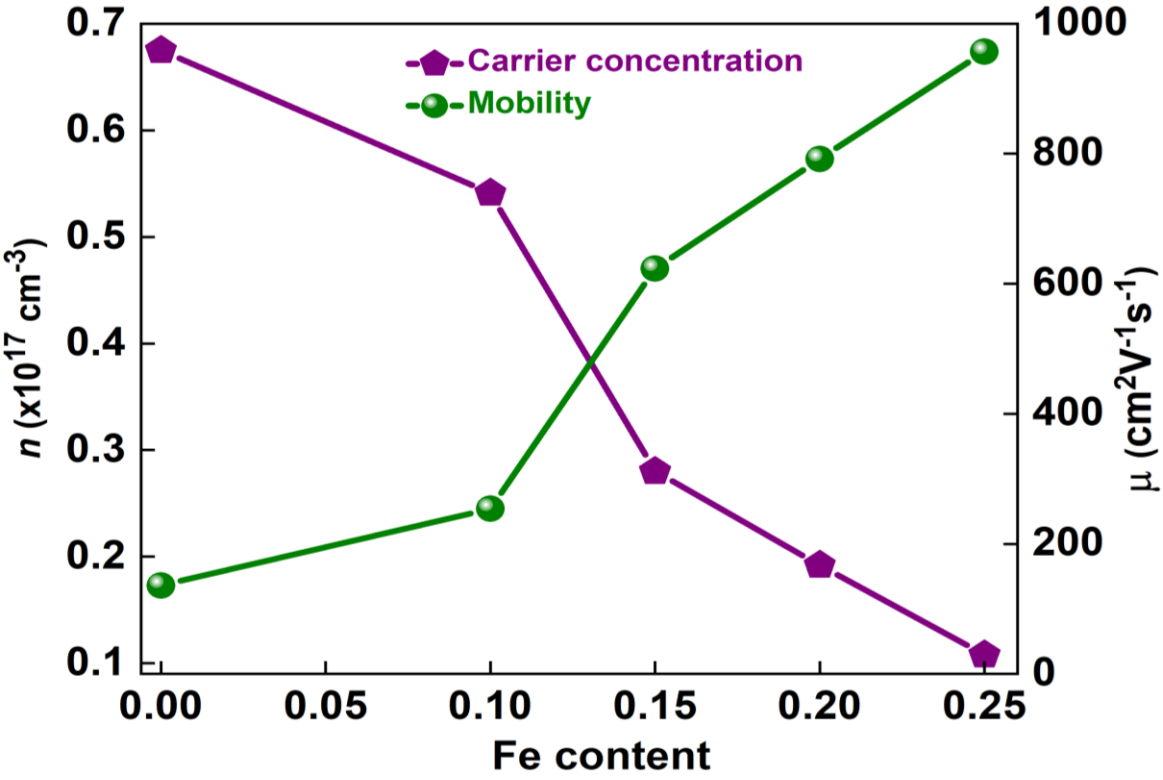

Figure 3.23: *Carrier concentration (n) and mobility (μ) as a function of Fe content in $Cu_{1-x}Fe_xO$ thin films.*

0.055, 0.097, 0.125) nanopowders decreased with increasing Fe concentration by the hall measurements [142].

The behaviour of copper oxide (CuO, tenorite) thin films, such as n-type or p-type, mainly depends on the preparation technique and the starting raw materials, as described by many researchers [137-143]. It is observed that CuO, having a p-type conductivity, shows a band gap of nearly 2.1 eV [137-139], whereas CuO showing n-type conductivity is observed to exhibit a band gap between 1.3 and 1.5 eV [139-143]. It is speculated that the presence of oxygen deficiency, which is unavoidable during the process of synthesis, makes the CuO exhibit n-type conductivity.

Different factors can contribute to the observed modulations in electrical conductivity/resistivity of $Cu_{1-x}Fe_xO$ nanostructures. Interatomic electron transition is one of the mechanisms involved in the electrical conductivity process. Short interatomic distances are desirable for improving the material's conductivity, as shorter distances result in broader energy bands, which facilitate the electron transition. As a result of the slightly smaller ionic radius of Fe^{2+} than Cu^{2+}, in the perfectly doped sample ($x \leq 0.20$), the interatomic distance needed for electron transition became smaller as compared to pure CuO. Therefore, the activation energy required for the interatomic electron transition in the prepared samples became smaller. A relatively high electrical conductivity of 1.8×10^{-5} S/cm was observed for Ni-doped CuO even at a lower concentration of around 2.9 at% [144].

Kuanr et *al.* [145] prepared Cu1-xNixO (x = 0%, 3%, 6%, and 9%) nanoparticles using the co-precipitation method. They observed that the electrical conductivity increases with Ni content until 0.06, as only the DMS structure exists. Then it decreases to 2.04×10^{-2} S/cm for the $Cu_{0.91}Ni_{0.09}O$ sample due to the lattice mismatch arising from the formation of a secondary NiO phase. This lattice mismatch is found to create incompatibility towards the smooth transition of an electron in the CuO system, which lowers the conductivity of this sample (Figure 3.24).

Further, the electrical properties of $Cu_{1-x}Fe_xO$ systems also depend on the electronic configuration of the outer d-shell. The electronic configuration for Cu^{2+} remains as $[Ar]3d^9$, whereas that of Fe^{2+} and Fe^{3+} are $[Ar]\ 3d^6$ $[Ar]\ 3d^5$, respectively. Therefore, doping Fe in CuO by replacing Cu^{2+} (d^9) induces a larger number of holes, which alleviates localisation at the valence band edge by increasing hole mobility. Since it is a p-type semiconductor, the majority charge carriers are holes, which influence the conductivity. In addition, the electrical

conductivity of CuO varies with deviations from its stoichiometric nature due to the multiple oxidation states of copper [146]. Cu vacancies are the most stable defects because of the existence of excess oxygen ions or deficiencies of copper ion, which therefore generates a nonstoichiometric form of p-type conducting CuO [147]. The stoichiometric deviation was deliberately improved by increasing the doping percentage of Fe as foreign impurity atoms in the CuO crystal lattice to enhance the electrical properties by generating constitutional defects. The concentration of defects is directly proportional to the lattice strain value determined by X-ray diffraction; therefore, an increase in defect concentration improves conductivity.

Yildirimcan have prepared (0, 2, 4, 6 mol%) Fe-doped CuO thin films by the spin coating technique [10]. The obtained electrical conductivity was found to decrease slowly with increasing Fe concentration, due to the effect of grain boundaries on the mobility of charge carriers [148]. Fe^{3+} ions cause a decrease in donor carrier concentration in the crystal lattice. Therefore, the Fermi level moves away from the conduction band. Joseph et al. also reported that the resistivity increased with 10% Fe doping to CuO thin film [149]. Chafi et *al.* reported that the conductivity decreased with increasing Fe concentration from 0 to 3% in CuO samples at room temperature [150].

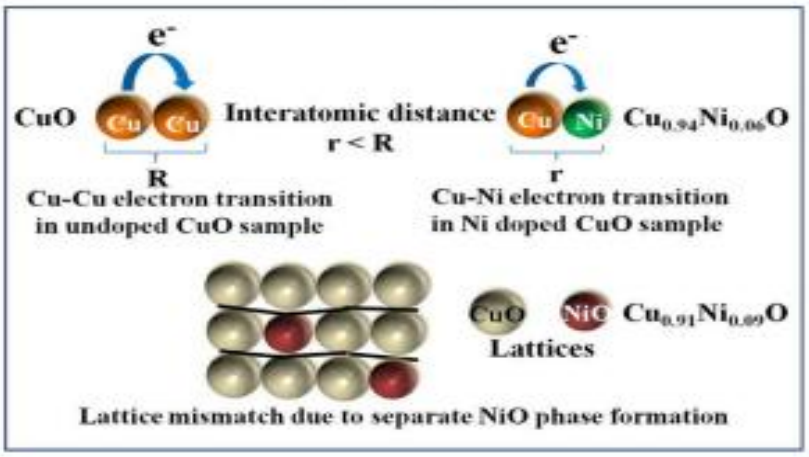

Figure 3.24: *Schematic of conduction mechanism in $Cu_{1-x}Fe_xO$ as a function of dopant concentration [145].*

References

[1] U.K. Gaur, A. Kumar, G.D. Varma, J. Mater. Chem. C., 3 (2015) 4297.
[2] Y. Li, M. Xu, L. Pan, Y. Zhang, Z. Guo, and C. Bi, J. Appl. Phys. 107(2010) 113908.
[3] S. Bhuvaneshwari, N. Gopalakrishnan, J. Mater. Sci. Mater. Electron., 30 (2019) 6920.
[4] D. Paul Joseph, C. Venkateswaran, S. Sambasivam, B.C. Choi, J. Korean Phys. Soc. 61 (2012) 449.
[5] M.H. Kabir, H. Ibrahim, S.A. Ayon, M.M. Billah, S. Neaz, Heliyon, 8(2022) e10609.
[6] S.L. Jenish, S. Valanarasu, I.L. Raj, V. Ganesh, I.S. Yahia, J. Photochem. Photob. A Chem. 462 (2025) 116215
[7] M. Nasir, N. Patra, M.A. Ahmed, D.K. Shukla, S. Kumar, D. Bhattacharya, C.L. Prajapat, D.M. Phase, S.N. Jha, S. Biring, and S. Sen, RSC Adv., 7 (2017) 31970.
[8] R.A. Young, D.B. Wiles, J. Appl. Crystallogr., 15 (1982) 430.
[9] MAUD program version 2.999. https://luttero.github.io/maud/maud/release/2023/07/03/new-version-2.999.html
[10] S. Yildirimcan, Indian J. Phys., 97 (2023) 1707.
[11] Z. Pezeshki-Nejad, S. Alikhanzadeh-Arani and M. Almasi Kashi J. Magn. Magn. Mater., 482 (2019) 301.
[12] A.M. El Sayed, M. Shaban, Spectrochim. Acta - Part A Mol. Biomol. Spectrosc., 149 (2015) 638.
[13] M. Shaban, A.M. El Sayed, H. AlMohamadi, M.T. Khan, A.M. Ahmed, Inter. J. Hydr. Energy. 56(41) (2024). 164.
[14] S. Pitiphattharabun, K. Auewattanapun, N. Sato, K. Janbooranapinij, R. Techapiesancharoenkij, G. Panomsuwan, J. Ohta and O. Jongprateep, Crystals, 12 (2022) 1536.
[15] O. Jongprateep, K. Meesombad, R. Techapiesancharoenkij, K. Surawathanawises, P. Siwayaprahm and P. Watthanarat, J. Met. Mater. Miner., 29 (2019) 78.
[16] K.B. Kim, M.S. Sohn, S. Min, J.W. Yoon, J.S. Park, J. Li, Y.K. Moon, Y.C. Kang. , Small, 20 (2024) 2308963.
[17] S. Mehraj, M.S. Ansari, A. Alimuddin, J. Nanoeng. Nanomanuf. 3 (2013) 229.
[18] K.T. Jacob, S. Raj, L. Rannesh, Int. J. Mater. Res. 9 (2007) 98.
[19] G. J. Wilso, A. S. Matijasevich, D. R. Mitchell, J. C. Schulz, G. D. Will, Langmuir, 22, (2006) 2016.
[20] S.M. Yakout and A.M. El-Sayed, Adv. Powder Technol., 30 (2019) 2841.
[21] M. Iqbal, M.A.Z.G. Sial, S. Shabbir, M. Siddiq, A. Iqbal, J. Photochem. Photobiol. A Chem., 335 (2017) 112.
[22] S.U. Din, M. Sajid, M. Imran, J. Iqbal, B.A. Shah, M. Azeem Ullah, S. Shah, Mater. Res. Express. 6 (2019) 85022.
[23] A. Ali, M.H. Jameel, S. Uddin, A. Zaman, Z. Iqbal, Q. Gul, Materials, 14,1 (2021)
[24] S.M. Karadeniz, D. Iskenderoğlu, M.E. Güldüren, H. Güney, S. Sarıtaş. , J. Mater. Sci.: Mater. Electr., 34 (2023) 1840.
[25] M.H. Jameel, S. Saleem, M. Hashim, M.S. Roslan, H.H.N. Somaily, M.M. Hessin, Nanotechnol Rev. 92 (2021) 1484.
[26] T. Liu, Y. Chen and L. Chen, Acta Metall. Sin. (English Lett.), 34, 85 (2021).
[27] D.P. Dubal, G.S. Gund, R. Holze and C.D. Lokhande, J. Power Sources, 242 (2013)

687.
[28] H. Khaleghi and M.H. Ehsani, Appl. Phys. A Mater. Sci. Process, 128 (2022) 969.
[29] A. Aslani and V. Oroojpour, Phys. B Condens. Matter., 406 (2011) 144.
[30] S. Ning, P. Zhan, Q. Xie, W. Wang, Z. Zhang, J.Mater. Sci. Technol., 31 (2015) 969.
[31] A. Ghosh, R.N.P. Choudhary, J. Phys. D: Appl. Phys., 42 (2009) 075416.
[32] A. Aslani and V. Oroojpour, Phys. B. Condens. Matter., 406 (2011) 144
[33] S. Sihag , R. Dahiya , S. Rani , Anushree2 , A. Kumar, V. Kumar, Indian Journal of Chemical Technology , 29 (2022) 578.
[34] A. Aslani, Phys. B Condens. Matter, 406 (2011) 150.
[35] H. Carranco, G. Juarez-Diaz, M. Galvan-Arellano , J. MartinexJuarez, J Lumin, 129 (2009) 1483.
[36] H. Z. Asl, S. M. Rozati; Research Square, (2022) https://doi.org/10.21203/rs.3.rs-1796153/v1.
[37] A. Pramothkumar, N. Senthilkumar, K.C. Mercy Gnana Malar, M. Meena and I. Vetha Potheher, J. Mater. Sci. Mater. Electron., 30 (2019) 19043.
[38] S. Arya, Prerna, A. Singh and R. Kour, Mater. Res. Express., 6 (2019) 116313.
[39] Y. Okamoto, S. Ishizuka, S. Kato, T. Sakurai, N. Fujiwara, H. Kobayashi and K. Akimoto, Appl. Phys. Lett., 82 (2003) 1060.
[40] P. Thomas, K. E. Abraham, Academic Review, XVIII, 108 (2012).
[41] D. Rajan, F. Francis , D. Thomas , M. Ramankutty, S.A. Joseph, IOP Conf. Ser.: Mater. Sci. Eng., 1233 (2022) 012005.
[42] K.H. Tam, C.K. Cheung, Y.H. Leung, A.B. Djurišić, C.C. Ling, C.D. Beling, S. Fung,W.M. Kwok, W.K. Chan, D.L. Phillips, L. Ding and W.K. Ge, J. Phys. Chem. B., 110 (2006) 20865.
[43] A.S. Lanje, R.S. Ningthoujam, S.J. Sharma, R.B. Pode and R.K. Vatsa, Int. Nanotechnol., 7 (2010) 979.
[44] S.M. Soosen, A. Chandran, J. Koshy and K.C. George, J. Appl. Phys., 109 (2011) 113702.
[45] A. Rufus, N. Sreeju, D.Philip, RSC advances, 6 (2016) 94206.
[46] S.M.Soosen, A. Chandran, J. Koshy, K.C. George; J. Appl. Phys., 109 (2011) 113702.
[47] K.H. Tam, C.K.Cheung, Y.H.Leung, A.B.Djurisic, C.C.Ling, C.D. Beling, S.Fung, W.M. Kwok, W.K. Chan, D.L. Phillips, L.Ding, and W.K.Ge, J. Phys.Chem.B, 110 (2006) 20865.
[48] R. S. Ningthoujam, V. Sudaran, S. K. Kulshreshtha,J. Lumin., 127 (2007)747.
[49] A.S Lanje, S. Raghumani, Ningthoujam, S. J. Sharma, R. B Pode, Adv. Powd. Technol., 24 (2013) 331.
[50] A. Lassoued, M.S. Lassoued, B. Dkhil, S. Ammar, A. Gadri, Phys. E: Low-Dimens. Syst. Nanostructures, 101 (2018)212.
[51] P. Chand, A. Gaur, A. Kumar, U.K. Gaur, Mater. Sci. Semicond. Process., 38 (2015) 72.
[52] G.F. Aaga, S.T. Anshebo. Heliyon, 9 (2023) e16067.
[53] S. Prakash, N. Elavarasan, A. Venkatesan, K. Subashini, M. Sowndharya, V. Sujatha. Adv. Powder Technol., 29 (2018) 3315.
[54] T. Chtouki, S. Taboukhat, H. Kavak, A. Zawadzka, H. Erguig, B. Elidrissi, B. Sahraoui., J. Phys. Chem. Solids, 124 (2019) 60.
[55] E.G. Goh, X. Xu, P.G. McCormick., Scr. Mater., 78 (2014) 49.
[56] N. Van Loi, L.T.N. Mai, N.H. Luong and B. Nguyen Quoc Trinh. Optical Mater. X., 19 (2023) 100246.
[57] W. Z. Tawfik, Z.S. Khalifa, M. Sh. Abdel-wahab, A. H. Hammad, J.Mater. Sci.:

Materials in Electronics, 30 (2019) 1275.
[58] A. L. Tchougreeff, J. Mol. Catal. A, 119 (1997) 377.
[59] R.S. Sabry, Y.K. Al-Haidarie and M.A. Kudhier, J. Sol-Gel Sci. Technol., 78 (2016) 299.
[60] C. Malerba, F. Biccari, C. Leonor Azanza Ricardo, M. D'Incau, P. Scardi and A. Mittiga, Sol. Energy Mater. Sol. Cells, 95 (2011) 2848.
[61] Al-Fa'ouri, A.M., Abu-Kharma, M.H., Awwad, A.M., Chem. Int., 7(2021)155.
[62] A.M. Al-Fa'ouri , O. A. Lafi , H. H. Abu-Safe ,M. A.Kharma, Arab. J.Chem., 16 (2023) 104535.
[63] T. Umebayashi, T. Yamaki, H. Itoh, K. Asai. J. Phys. Chem. Solids, 63(2002) 1909.
[64] S. Ruzgar, Y. Caglar, O. Polat, D. Sobola, M. Caglar. Appl. Phys. A, 127 (2021) 924.
[65] Alharbi, E.M., Rajeh, A., J. Mater. Sci. Mater. Electron. 33(2022) 22196.
[66] T.S. Moss, G.J. Burrell, B. Ellis, M.A. Omar, Semiconductor Opto-Electronics, Butterworth-Heinemann, (Elsevier Ltd, 1973).
[67] T.C. Paul, J. Podder and M.H. Babu, Surf. Interface. 21(2020) 100725.
[68] A. Escobedo-Morales, I.I. Ruiz-López, M. de L. Ruiz-Peralta, L. Tepech-Carrillo, M. Sánchez-Cantú, J.E. Moreno-Orea. Heliyon, 5 (2019) e01505.
[69] Y. Du, X. Meng, X. Gao. Thin Solid Films. 684 (2019) 53.
[70] A. Jjaq, Ö. Barin, A.O. Çağırtekin, B. Soltabayev, S. Acar, Ceram. Inter., 49(24) (2023) 40853.
[71] M. Idrees, S. Khan, S. Hussain, J.Optics and Photonics Research (2025).
[72] A. Ogwu, T. Darma, E. Bouquerel, *J. Achiev. Mater. Manuf. Eng.*, 24(2007) 172.
[73] M. Iqbal,A.Ali, K. S.Ahmad, F. M. Rana,J. Khan, K. Khan, K.H.Thebo, SN Applied Sciences, 1 (2019) 647.
[74] N.M. Basith, J.J. Vijaya, L.J. Kennedy, M. Bououdina, Physica E: Low Dimens. Syst. Nanostruct., 53(2013) 193.
[75] A.S. Ethiraj, D.J. Kang, Nanoscale Res. Lett., 7(2012) 70.
[76] K. Borgohain, S. Mahamuni, J. Mater. Res.,17 (2002)1220.
[77] M. Yang, J. He, X. Hu, C. Yan, Z. Cheng, Environ Sci.Technol.,45 (2011)6088.
[78] M. Chaudhary, M. Singh, A. Kumar, Prachi , Y.K. Gautam, A.K. Malik, Y. Kumar, B.P. Singh Ceram. Int., 47(2021) 2094.
[79] A. Khalid, P. Ahmad, A. I. Alharthi, S. Muhammad, M. U. Khandaker, M. Rehman, M. R. I. Faruque, I. U. Din, M. A. Alotaibi, K. Alzimami, D. A. Bradley, Nanomaterials, 11 (2021) 451.
[80] Y. Bellal, A. Bouhank, H. Serrar , T. Tüken and G. Sığırcık. MATEC Web of Conferences 253 (2019) 03002.
[81] Md. R. Islam, M. A. Zubair, M. S. Bashar and A. K. M. B. Rashid, Sci. Rep., 9 (2019) 5205.
[82] T. Umebayashi, T. Yamaki, H. Itoh and K. Asai, J. Phys. Chem. Solids, 63 (2002) 1909.
[83] J. Amir, S. Muhammad, M. Kashif, A. Ali Khan, M. Gul, H.Sun, M.Shah, S. Azizi, M. Maaza, J. Iran. Chem. Soc., 22 (2025) 63.
[84] S. Baturay, I. Candan and C. Ozaydın. J. Mater. Sci. Mater. Electron., 33 (2022) 7275.
[85] M. Sajid, M. Imran, Salahuddin, J. Iqbal. Appl. Phys. A, 124 (2018) 768.
[86] Md. R. Islam, M. A. Zubair, M. S. Bashar and A.K.M.B. Rashid. Sci. Rep., 9(2019) 5205.
[87] A. Alkathiri, *J. Radiat. Res. Appl. Sci.*, 17 (2024) 100783.
[88] H. Çavusoglu, Europ. J. Sci. Technol., 13 (2018) 124.
[89] T. Shrividhya, G. Ravi, Y. Hayakawa, T. Mahalingam, J. Mater. Sci. Mater. Electron.

25 (2014) 3885.
[90] A. Moumen, B. Hartiti, E. Comini, Z. el khalidi, H.M.M.M. Arachchige, S. Fadili, P. Thevenin, Superlattice. Microst. 127 (2019) 2.
[91] T. S. Moss, Physica Status Solidi (B), 131 (1985)415.
[92] S. Tripathy, Optical Materials, 46 (2015) 240.
[93] J. A.Samdani, Z.Alrowaili, K. C.Sekhar, I.Olarinoye, C.Sriwunkum, A.Alalawi, *J. Radiat. Res. Appl. Sc.*, 16(2023) 100747.
[94] P. Herve, L. Vandamme, Infrared Physics & Technology, 35(1994) 609.
[95] V. Dhanasekaran , T. Mahalingam, R. Chandramohan, Jin-Koo Rhee , J.P. Chu, Thin Solid Films, 520 (2012) 6608.
[96] L. D. Valladares , D. H. Salinas, A. B. Dominguez, D. A. Najarro ,S.I. Khondaker , T. Mitrelias, C.H.W. Barnes , J. A. Aguiar , Y. Majima, Thin Solid Films, 520 (2012) 6368.
[97] D. Gopalakrishna, K. Vijayalakshmi ,C. Ravidhas , J. Mater. Sci.: Mater. Electron, 08 (2012) 667.
[98] Y. Akaltun, Thin Solid Films, 594 (2015) 30.
[99] D. G.El-Damhogi, E.ELesh, A. H.Ibrahim, S.Mosaad, M. M. Makhlouf, Z. Mohamed, Radiat. Phys. Chem., 195 (2022)110060.
[100] N. Sreeju, A. Rufus, D. Philip, J. Phys.Chem.Solids (2018).
[101] H.M. Xiao, L.P. Zhu, X.M. Liu, S.Y. Fu, Solid State Commun., 141 (2007) 431.
[102] T.S. Moss, Proc. Phys. Soc. Sect. B., 67 (1954) 775.
[103] E. Burstein, Phys. Rev., 93 (1954) 632.
[104] A. Kumar, M. Kumar, P. Chandra Sati, M.K. Srivastava, S. Ghosh, S. Kumar, Curr. Appl. Phys., 32 (2021) 24.
[105] C. Rajashree, A.R. Balu, V.S. Nagarethinam, Surf. Eng., 31 (2015) 316.
[106] S. Rehman, A. Mumtaz, S.K. Hasanain, J. Nanopart. Res.13 (2011) 2497.
[107] H. Khaleghi and M.H. Ehsani, Appl. Phys. A Mater. Sci. Process, 128 (2022) 969.
[108] A. A. Lepeshev, IV Karpov, A.V. Ushakov, D.A. Balaev, A. A. Krasikov, A. Dubrovskiy, D.A.Velikanov , M.I. Petrov, J. Supercond. Nov. Magn., 30 (2017) 931.
[109] M. ul Haq, M. Iqbal, M.A.Z.G. Sial, S. Shabbir, M. Siddiq, A. Iqbal, J. Photochem. Photobiol. A Chem., 335 (2017) 112.
[110] J.M.D. Coey, A.P. Douvalis, C.B. Fitzgerald, M. Venkatesan, Appl. Phys. Lett., 84 (2004) 1332.
[111] A. Morrish, Canted antiferromagnetism: Hematite (pp. 1–2). World Scientific Publishing Company Pty. Ltd. (1994).
[112] Y. An, S. Wang, L. Duan, J. Liu, Z. Wu, Appl. Phys. Lett. 102 (2013) 212411.
[113] C. Zener, Physical Review, 82, 403 (1951).
[114] S. Manna, S.K. De, J. Magn. Magn. Mater., 322 (2010) 2749.
[115] A. Yogi, D. Varshney, Mater. Sci. Semicond.Process., 21 (2014) 38.
[116] C. C.Vidyasagar, Y. Arthoba Naik, T. G. Venkatesh, R. Viswanatha. Powder Technology, 214 (2011) 337.
[117] S. Aditya, M. Varshney, J. Park, T. Ha, K.-H. Chae, and H.-J. Shin, RSC Advances, 5 (2015) 21762.
[118] P. Kankanit, S. Suphankij, W. Mekprasart, W. Pecharapa. Energy procedia, 34 (2013) 740.
[119] H.Y. Dang,Y.L.Zhang, J.K. Liang, S.S.Xie, J. Mater. Sci., 28 (1993) 5176.
[120] U. K. Gaur, A. Kumar, G. D. Varma, J. Mater. Chem. C, 3 (2015) 4297.
[121] K. L.Liu, S. L. Yuan, H. N. Duan, S. Y. Yin, Z. M. Tian, X. F. Zheng, S. X. Huo, C. H. Wang. Mater. Lett., 64 (2010) 192.
[122] A.M. Raba-Páez, I.M.S. Gaona, J.O.D. Malafatti, C.A.P. Vargas, A.J. Chiquito, E.C.

Paris, M.R. Joya, Mater. Charact., 201 (2023) 112978.
[123] K.B. Kim, M.S. Sohn, S. Min, J.W. Yoon, J.S. Park, J. Li, Y.K. Moon, Y.C. Kang. Small, 20 (2024) 2308963.
[124] B. D. Cullity, C. D. Graham, "Magnetic Anisotropy," in Introduction to Magnetic Materials, Hoboken, New Jersey, Wiley, 2009, pp. 197-238.
[125] W. D. Callister Jr and D. D. Rethwisch, "Magnetic properties," in Material Science and Engineering, Hoboken, NJ, Wiley, 2014, pp. 804-836.
[126] K. Tanbir, M. P. Ghosh, R. K. Singh, M. Kar, S. Mukherjee, J. Mater Sci. Mater. Elec., 31 (2020) 435.
[127] B. D. Cullity, C. D. Graham. Introduction to Magnetic Materials. John Wiley and Sons, New Jersey, 2 edition, 2009.
[128] R.V. Vijayalakshmi, G. Saravanan, P. P. Kumar, K. Ravichandran, AIP Conf. Proc. 1953 (2018) 030160.
[129] M. Chandrasekar, M. Subash, S. Logambal, G. Udhayakumar, R. Uthrakumar, C. Inmozhi, J. King Saud University – Science, 34 (2022) 101831.
[130] Y. Du, X. Meng, X. Gao, Thin Solid Films. 684 (2019) 53.
[131] S. Baturay, I. Candan, C. Ozaydın, J. Mater. Sci. Mater. Electron., 33(9) (2022) 7275.
[132] A. Punnoose, H. Magnone, M.S. Seehra and J. Bonevich, Phys. Rev. B – Condens Matter Mater. Phys., 64 (2001) 174420.
[133] P.R. Shao, S.Z. Deng, J. Chen, J. Chen, N.S. Xu, J. Appl. Phys., 109 (2011) 023710.
[134] Y.K. Jeong, G.M. Choi, J. Phys. Chem. Solids, 57 (1996)81.
[135] E. Swatsitang, K. Attaphol, P.Sumalin, H.Sitchai, P.Thanin, J. Sol-Gel Sci. Technol., 83 (2017) 382.
[136] V.F. Drobny, L. Pulfrey, Thin Solid Films, 61 (1979) 89.
[137] B. Balamurugan, B.R. Mehta, Thin Solid Films, 396 (2001) 90.
[138] F. Marabelli, G.B. Parraviciny, F.S. Orioli, Phys. Rev. B, 52 (1995) 1433.
[139] J. Ghijsen, L.H. Tjeng, J.V. Elp, H. Eskes, J. Westerink, G.A. Sawatzky, M.T. Czyzyk, Phys. Rev. B, 38 (1988) 11322.
[140] Y. Chaudhary, A. Agarwal, R. Shrivastav, V. Satsangi, S. Dass, Int. J. Hydrogen Energy, 29 (2004) 131.
[141] F.P. Koffyberg, F.A. Benko, J. Appl. Phys., 53 (1982) 1173.
[142] P. Samarasekara, GESJ Phys., 2(4) (2010) 3.
[143] M. Nasir, G Kumar, P M Shirage, and S Sen, J. Nanosci. Nanotechnol., 17 (2017) 1345.
[144] C.T. Meneses, J.G.S. Duque, L.G. Vivas, M. Knobel, J. Non-Cryst. Solids, 354 (2008) 4830.
[145] S.K. Kuanr, S. Nayak, K. S. Babu. Mat.Sci. Semicon. Proc., 71 (2017) 268.
[146] Y.K. Jeong, G.M. Choi, J. Phys. Chem. Solids, 57 (1996) 81.
[147] M. Muhibbullah, M.O. Hakim, M.G.M. Choudhury, Thin Solid Films, 423 (2003) 103.
[148] P. Samarasekara, U. Wijesingh, E. N. Jayaweera GESJ: Phys.1 (2015) 13.
[149] D. P. Joseph, C. Venkateswaran, J. Korean Phys. Soc., 61 (2012) 449.
[150] F. Z. Chafi, B. Fares, A. Hadri, C. Nassiri, L. Laaneb, N. Hassanain, A. Mzerd, IRSEC (2015) 1209.

Conclusion

Conclusion

Nanostructured $Cu_{1-x}Fe_xO$ (x = 0.10, 0.15, 0.20 and 0.25) thin films were successfully prepared via a spray pyrolysis method on a glass substrate at 350 ºC. The main results of the present work are summarised as follows:

- The XRD results indicated a monoclinic phase for all samples. At higher Fe concentration (x = 0.25), a secondary α-Fe_2O_3 impurity phase (~8%) was detected.
- The average crystallite sizes were found to decrease from 46 to 33 nm with increasing Fe content, simultaneously with enhanced lattice strains and dislocation density.
- SEM analysis revealed cubic-like particle morphology. The average particle size was observed to decrease with increasing dopant concentrations, reaching 80 nm for x = 0.25.
- Optical Band gap decreases from 3.075 eV for x = 0 to 2.974 eV for x = 0.25. Moreover, the Urbach energy increased with higher Fe doping levels, suggesting enhanced optical properties.
- Magnetic measurements showed ferromagnetic behaviour in the $Cu_{1-x}Fe_xO$ nanostructured films (MD structure), with significant improvements in magnetisation with increasing Fe content. The coercivity fluctuated between 17.6 and 231.5 Oe due to magnetic anisotropy and microstructure.
- The electrical resistivity and carrier concentration decrease steadily to about 5.8 kΩ.cm and 0.108×10^{17} cm^{-3}, respectively, for x = 0.25, while the electrical conductivity and mobility increase to 0.17 $S.cm^{-1}$ and 957 $cm^2V^{-1}s^{-1}$.

The spray pyrolysis process at 350ºC effectively tailors the physical properties of nanostructured $Cu_{1-x}Fe_xO$ thin films. The improved magnetisation and optical properties make these dilute magnetic semiconductor (DMS) films highly suitable for advanced spintronics and optoelectronic device applications. The ability to tune the material properties through controlled Fe doping opens new avenues for developing multifunctional nanostructured materials for various technological applications.

-

Appendix

Appendix

i. Origin of Magnetism

Magnetic fields are created by the movement of charge through space. In atoms, it is the movement of electrons that produce the magnetic fields. The strength of the magnetic field produced is known as magnetic moment (μ). Magnetic moments are associated with both the spin (s) and orbital (l) angular momentum of each electron. The magnetic moment of an individual electron is the Bohr magneton given by:

$$\mu_B = eh / 2\pi m_e \quad \text{(i.1)}$$

Where e is the charge of the electron; h is the Planck constant, and me is the mass of an electron.

When a material consisting of several atoms is subjected to an applied magnetic field (H), the net magnetic moment per unit volume of the material is defines as the magnetization (M). The response of a material upon application of a magnetic field is known as magnetic induction or magnetic flux density (B). Inside a magnetic material, the relationship between B and H due to the magnetization is given by:

$$B = \mu_0 (H+M) \quad \text{(i.2)}$$

One of the most important properties of magnetic materials is susceptibility (χ) which is the degree of magnetization induced in a material per unit applied magnetic field. It is given by Equation:

$$X = M / H \quad \text{(i.3)}$$

ii. Classes of Materials

Materials are divided into different classes of magnetism based on how the atoms interact collectively (Table i.1).

ii.1. Diamagnetism

The magnetic response of the materials belonging to this category is opposite in direction to the external magnetic field. There are no unpaired electrons in outer orbits of atoms/molecules of such materials and hence their net magnetic moment is zero. The

susceptibility of diamagnetic materials have negative sign and the direction of induced magnetic moment is opposite to the applied external magnetic field [1]. The response signal of diamagnetic materials is independent of temperature.

***Table i.1**: Classification of materials based on their magnetic susceptibility [3].*

Type of magnetism	Magnetic susceptibility, χ	Atomic / Magnetic Behavior	Temperature dependence	Examples and comments
Diamagnetic	Negative and small, Au: -2.74×10^{-6} Cu: -0.77×10^{-6}	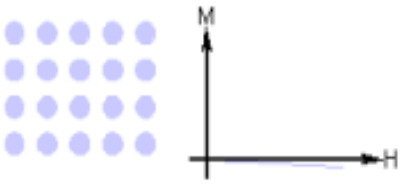	Temperature independent	The shells of the atoms are closed as in the case of covalent solids such as Ge, Si, and metals such as Au, Cu, Ag, etc.
Paramagnetic	Positive and small, β-Sn: 0.19×10^{-6} Pt: 21.04×10^{-6} Mn: 66.10×10^{-6} 10^{-5}-10^{-4}	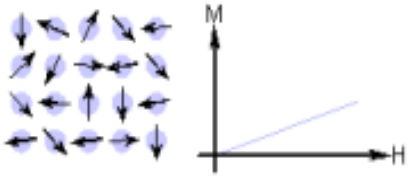	Temperature independent	Atoms have randomly oriented magnetic moments as in alkali and transition metals
	Positive and small		Follows Curie or Curie-Weiss law: $\chi = \frac{C}{T-\theta}$	Atoms constituting the material have a permanent magnetic moment as in ferromagnets (Fe), antiferromagnets (Cr), ferrimagnets (Fe_2O_3) at high temperatures
Ferromagnetic	Positive and large, function of applied field, microstructure dependent Fe: ~100,000	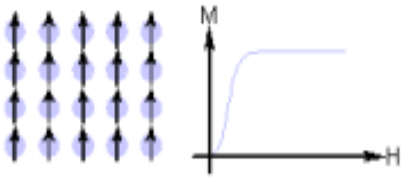	Ferromagnetic below Curie temperature and paramagnetic above it	Atoms have parallel aligned magnetic moments, possesses large permanent magnetization even without external magnetic field as in some transition metals and rare earths such as Fe, Co, Ni, Gd, Dy
Antiferromagnetic	Positive and small, Cr: 3.6×10^{-6}	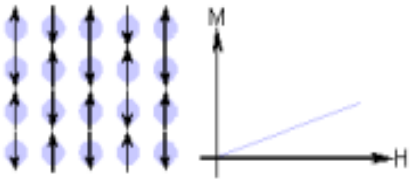	Antiferromagnetic below the Néel temperature and paramagnetic above it	Atoms have mixed parallel and anti-parallel aligned magnetic moments Primarily oxides and salts of transition metals such as MnO, NiO, MnF_2.
Ferrimagnetic	Positive and large, function of applied field, microstructure dependent, Ba ferrite: ~3	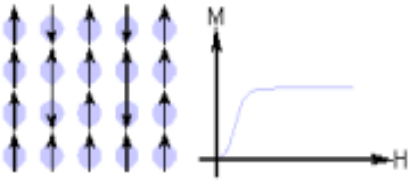	Ferrimagnetic below the Curie temperature and paramagnetic above it	Atoms have anti-parallel aligned magnetic moments, possesses large magnetization even without external magnetic field

ii.2. Paramagnetism

The Paramagnetic behaviour is possessed by the materials whose atoms/molecules have unpaired electrons in the outer orbits which leads to some net non-zero moments. But for bulk material, the moments are aligned in random directions and cancel out each other which

results in zero magnetization. However, when an external magnetic field is applied, the moments align with the direction of the magnetic field and leading to net non-zero magnetic moment. The susceptibility for paramagnetic materials can be given by Curies-Weiss law :

$$\chi = N\mu_0 m^2 / 3K_B T \qquad \text{(i.4)}$$

where μ_0 is the magnetic permeability , N is number of dipoles per unit volume, T is temperature and K_B is Boltzmann's constant.[1,4]

The magnetic susceptibility of paramagnetic materials is very small (~10^{-4}). The strength of magnetization decreases with temperature which may be due to the more random thermal mis-alignment of the magnetic domains.

ii.3. Antiferromagnetism

The antiferromagnetic materials have both kind of magnetic moments i.e. parallel and antiparallel . These moments tends to cancel out each other which leads to overall zero magnetization. This effect is normally observed in transition metal oxides such as Nickel Oxide (NiO) and Cobalt Oxide (CoO). The temperature above which antiferromagnetic order vanishes is known Néel temperature (T_N). Above this temperature T_N, antiferromagnetic materials behave like ferromagnetic materials and their magnetic susceptibility can be explained by Curie-Weiss theory. But they have a negative intercept in negative exchange interactions in M vs H curve [1].

ii.4. Ferrimagnetism

The Ferrimagnetic behaviour is similar to ferromagnetism and it is usually observed in ferrites and garnets. In ferrimagnetic materials, the interactions between nearest neighboring magnetic domains (atomic sublattices) are antiferromagnetic, but these magnetic domains have unequal magnetic moments and which results into a resultant net non-zero magnetic moment. Such materials are generally consisting of two or more different type of elements/ions for example Fe^{2+} and Fe^{3+}. The atomic sub-lattices of these atoms/ions are ferromagnetic and they have unequal magnetic moments. Ferrimagnetism is usually mediated by indirect exchange or superexchange interactions. Ferrimagnetic materials exhibits all the characteristics of ferromagnetic behaviour [1,2]: spontaneous magnetization, Curie temperatures, hysteresis, and remanence etc.

ii.4. Ferromagnetism

The materials having unpaired electrons exhibits ferromagnetism. The unpaired electrons cause the material to have a net magnetic moment. When an external field is applied to such, the electron spins aligns in the direction of the external magnetic field. These spins remain aligned even after removal of the magnetic field as shown in Table i.1. The alignment is not disturbed even due to the effect of thermal agitation. The electron spins interact with each other through various exchange mechanisms in an energetically favorable way.

Numerous ferromagnetic materials have large number of magnetic domains consisting 10^{12} to 10^{15} atoms and aligned in same direction which results in large magnetization. It can also be visualized as presence of large number of individual crystals in a bulk polycrystalline material. The magnetic moment of the magnetic domains aligns in a specific axis the ferromagnetic material, which is also known as the easy axis. It happens due to coupling between the electronic spin and the angular momentum of the atomic orbit. The easy axis also makes the magnetic moment is anisotropic to the magnetization. When the direction of the applied magnetic field is not parallel to the specific axis, the magnetic field has to overcome the energy barrier for pulling all the moments away from the easy axis and align towards magnetic field. This energy barrier is known as the magneto crystalline anisotropy and it is the atomic origin of hysteresis behavior in magnetic materials.

Some of the most common examples of ferromagnetic materials include Iron (Fe), nickel (Ni), and cobalt (Co) etc. Ferromagnetism have strong relationship on temperature. The maximum temperature at which a ferromagnetic material retains its magnetization is known as the Curie temperature (TC). When Temperature is more than curie temperature, the atomic spins orientations tends to misalign due to thermal agitation and leading to reduced magnetization similar to paramagnetic materials.

ii.4.1. Hysteresis

Ferromagnetic materials have a special property of retaining the memory of an applied magnetic field event when it is removed. This behavior is known as hysteresis, and a plot of the variation of magnetization with respect to magnetic field reveals the hysteresis loop. This phenomenon occurs due to the presence of magnetic domains. Hysteresis is a very important property and is extremely useful for making magnetic memory devices (Figure i.1).

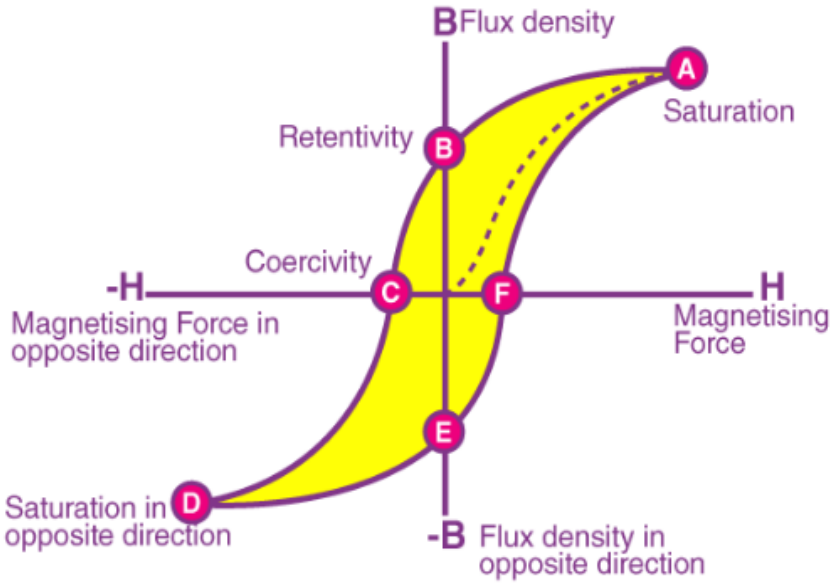

Figure i.1: *Hysteresis Curve for ferromagnetic material.*

iii. Magnetic Exchange Interactions

iii.1. Indirect Exchange Interactions

Various exchange mechanisms have been evolved for explaining magnetism in transition metal (TM) doped semiconductors. The three main classical indirect exchange mechanisms are [2]:

iii.1.1. RKKY Exchange Interactions

RKKY is an indirect exchange mechanism which has been named after scientist who discovered it: Ruderman, Kittel, Kasuya, and Yosida. This mechanism explains the coupling of magnetic moments using Coulomb exchange interactions through energy bands electrons over large distances. This theory was formulated for investigating ferromagnetism phenomenon in metals, and is an efficient mechanism when a high concentration of free carriers are present (Figure 2a) [5-7]. The interactions can be either ferromagnetic or antiferromagnetic based on distance between atoms involved in interactions. However, the defect energy levels of transition metals lie in middle of bandgap and do not contribute any free carriers for supporting exchange interaction [20]. Overall, this indirect exchange mechanism provides flexibility for modifying magnetic properties by changing concentration of holes.

iii.1.2. Double Exchange Mechanism

it involves the coupling of magnetic ions in different charge states by the hopping of an electron from one ion to another through interacting with the p-orbital (Figure 2b) [8]. Spin flips are not allowed in this model and it is energetically favorable if both the ions have a similar magnetic structure.

iii.1.3.Superexchange

The exchange interaction which is resulted from the coupling of nearest neighbor transition metals through a shared cation, known as super-exchange intraction (Figure 2c). This mechanism results from the virtual hopping of carriers between the completely filled p-orbitals of anions and the d orbitals of the magnetic TM cations. In order for electrons from both adjacent atoms to occupy the same p-level, they must be opposite in spin, a result of Pauli exclusion principle considerations. This leads to an antiferromagnetic coupling of nearest-neighbor cations through a shared anion.

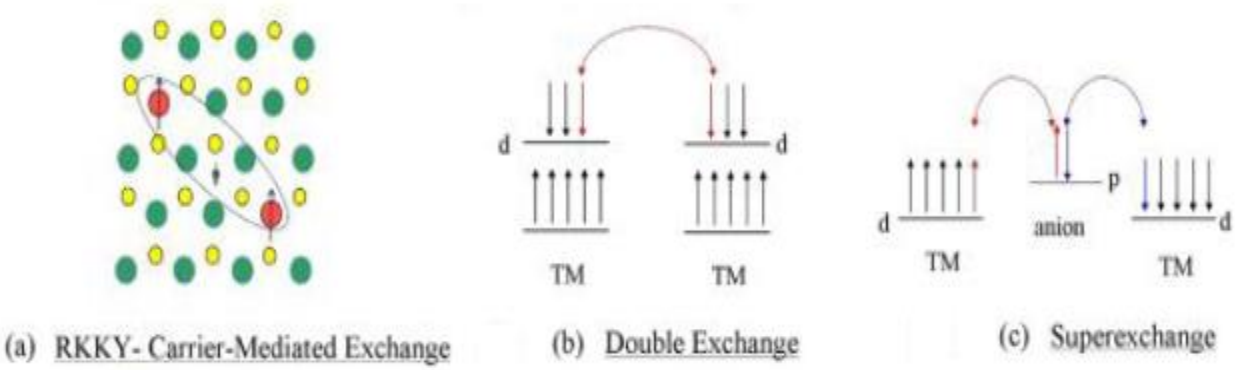

***Figure i.2**: Classical indirect exchange mechanisms*

In magnetic semiconductors, there are two main spin-dependent coupling mechanisms that control the magneto-optical phenomenon:

(i) coupling between the conduction-band electrons (s-character) and localized spins (d-character),

(ii) hole exchange coupling: coupling between the valence band holes (p-character) and localized spins (d-character).

iii.2. Additional Exchange Mechanisms in DMS

In addition to the classical direct and indirect mechanism, several additional indirect exchange mechanisms have been proposed and developed to explain the observation of ferromagnetism in DMS.

iii.2.1. Bound Magnetic Polarons

The bound magnetic polarons are formed by the alignment of the spins of many transition-metal ions with that of much lower number of weakly bound carriers such as excitons within a polaron radius. The basic idea is schematically illustrated in Figure i.3. The localized holes of the polarons act on the transition-metal impurities surrounding them, thus producing an effective magnetic field and aligning all spins [9]. As temperature decreases the interaction distance (boundary) grows. Neighboring magnetic polarons overlap and interact via magnetic impurities forming correlated clusters of polarons. One observes a ferromagnetic transition when the size of such clusters is equal to the size of the sample. This model is inherently attractive for low carrier density systems such as many of the electronic oxides.

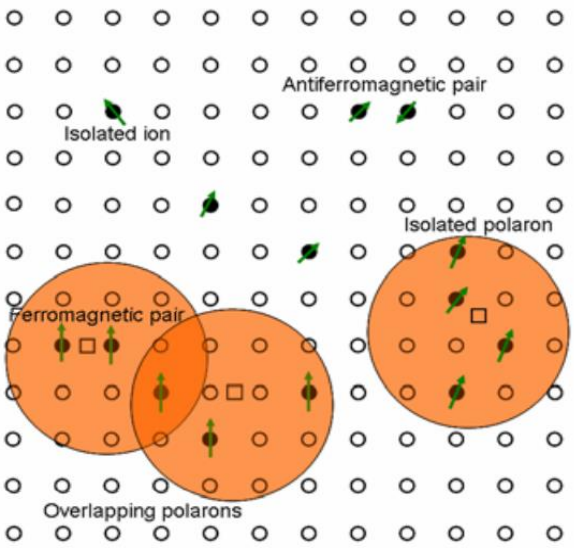

***Figure i.3**: Bound Magnetic Polaron Interactions [9].*

iii.2.2.Donor Impurity Band Exchange

This model suggests that defect centers mediate ferromagnetism and are responsible for the magnetization seen in TM doped ZnO [9,10]. Three scenarios for TM doping in ZnO were evaluated in this model (Figure i.4). In the first scenario of a light 3d element (e.g. TM = Ti), the 3d spin-up states lie high in the 2p (O) and 4s (Zn) gap, overlapping the spin split

donor impurity band. For the next element (TM = Mn) there is no overlap with the 3d level and the exchange is weak, and towards the end of the series (TM = Co) the 3d down states overlap with the impurity band which then has the opposite spin splitting for the same occupancy. High TC are found when the unoccupied 3d states overlap the impurity band. The origin of the donor impurity band has been attributed to oxygen vacancies (F centers) in ZnO and it has been proposed that this model can be used to explain ferromagnetism in GaN, which can be caused by the d^0 centers.

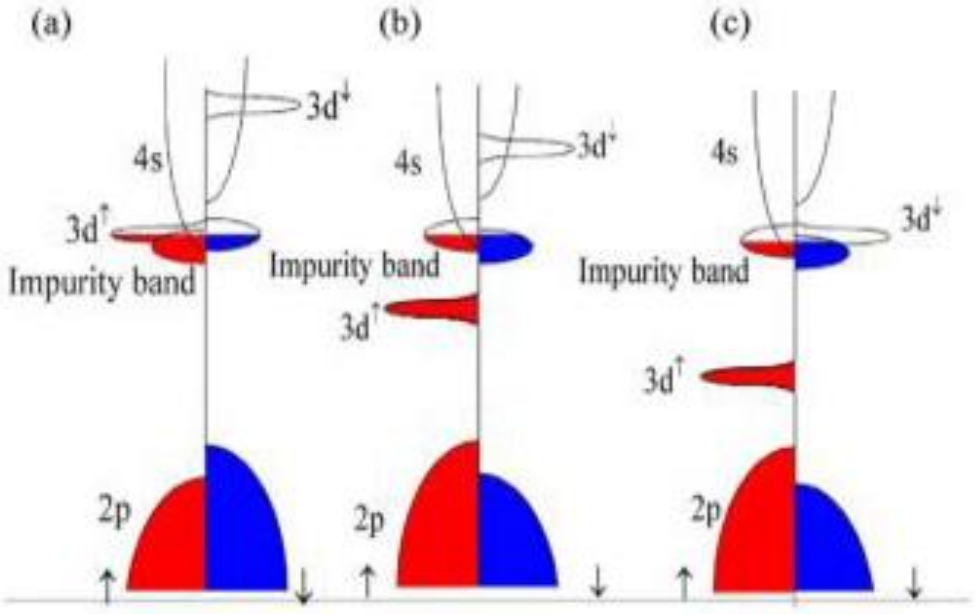

***Figure i.4** : Density of States for TM doped ZnO (a) Ti, (b) Mn, and (c) Co [2]*

The higher magnetization that is seen in ZnO at the interfaces is due to the defects that are present in the region. Thus in order for long range magnetization to occur it is essential to have high carrier concentration and a large number of vacancies. Once the donor concentration increases significantly, the donors merge with the conduction band and then RKKY exchange mechanism begin to dominate.

References

[1] M. Getzlaff, Fundamentals of Magnetism, Springer, Berlin, 2008
[2] H.S. Kaushik, Thesis, J.C. Bose University of Science & Technology, YMCA, Faridabad (2011).
[3] Ü. Özgür, Y. Alivov, H. Morkoç , J. Mater. Sci.: Mater. Electron., 20 (2009)789.
[4] D. Jiles, Introduction to Magnetism and Magnetic Materials, Chapman & Hall, New York, 1991.
[5] M. A. Ruderman and C. Kittel, Physical Review 96 (1954) 99.
[6] T. Kasuya, Progress of Theoretical Physics 16 (1956) 45.
[7] K. Yosida, Physical Review, 1 (1957) 893.
[8] C. Zener, Physical Review, 82 (1951) 403.
[9] J. M. D. Coey, M. Venkatesan, C. B. Fitzgerald, Nat. Mater., 4 (2005) 173.
[10] M. Venkatesan, C. B. Fitzgerald, J. G. Lunney, J. M. D. Coey, Physical Review Letters, 93 (2004) 177206.